Automatic vascularization of massive arterial networks in the human cerebral cortex: a computational modeling approach

Eduardo Guerreiro Zilves

Petrópolis, RJ - Brazil

August, 2024

Eduardo Guerreiro Zilves

Automatic vascularization of massive arterial networks in the human cerebral cortex: a computational modeling approach

Dissertation submitted to the examining committee in partial fulfillment of the requirements for the degree of Master of Sciences in Computational Modeling.

National Laboratory for Scientific Computing

Graduate Program in Computational Modeling

Advisor: Pablo Javier Blanco

Petrópolis, RJ - Brazil

August, 2024
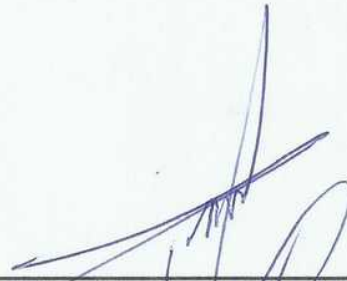
Eduardo Guerreiro Zilves
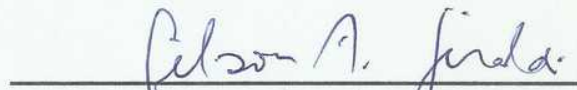
Automatic vascularization of massive arterial networks in the human cerebral cortex: a computational modeling approach

Dissertation submitted to the examining committee in partial fulfillment of the requirements for the degree of Master of Sciences in Computational Modeling.
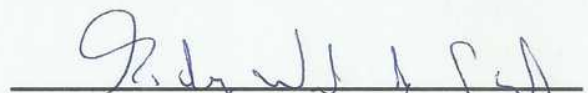
Approved by:

_____
Prof. Pablo Javier Blanco, D.Sc.
(Chair of the Committee)

_____
Prof. Gilson Antonio Giraldi, D.Sc.

_____
Prof. Rodrigo Weber dos Santos, D.Sc.

Petrópolis, RJ - Brazil

August, 2024

Dedication
To my family, and my friends.

Acknowledgements

"My formula for greatness in a human being is AMOR FATI: *that one wants nothing to be different, not forward, not backward, not in all eternity. Not merely bear what is necessary, still less conceal it — all idealism is mendaciousness in the face of what is necessary — but* LOVE *it."*

(**Friedrich Nietzsche**, *Ecce Homo.*)

(tr. W. Kaufmann)

Abstract

Stroke-related diseases add up to 11% of worldwide deaths, and medical imaging techniques describe many aspects of cerebral circulation. Nevertheless, the limited resolution of these techniques hinders the assessment of smaller vessels. Computational models aid in this problem, providing tools to analyze physiological scenarios otherwise inaccessible. This work proposes a methodology to build vascular networks in the human cerebral cortex across different regions of the pial surface and the gray matter. An adaptive version of the Constrained Constructive Optimization that exploits distributed computing generates blood vessels following anatomical rules. A patient-specific geometry of the brain is used as geometric substrate, and an existing model of larger arteries is the base from where the vascular network is expanded. The geometry is partitioned into three independent territories for each large cerebral artery. A thin volume of the pial surface has blood vessels generated down to the scale of arterioles of 50 micron in lumen diameter. The network penetrates the gray matter, and vascularization is constructed by appending samples of sub-trees to each terminal vessel, which are generated separately with properties associated with the gray matter. The final network for the left hemisphere reaches 234 000 vascular segments in the pial network, and 23.3 million vascular segments including the gray matter. Vessel diameters over the pial surface vary between 2100 µm and 26 µm, and terminals between 50 µm and 60 µm. The resulting network can be coupled with existing models of the cardiovascular system to simulate pulsatile blood flow and investigate the blood pressure variations along the cerebral cortex in normal and pathological conditions. This novel approach proposes a strategy for understanding patient-specific microcirculation under different conditions, allowing to evaluate the risk of stroke, among other mechanisms involved in the onset and progress of degenerative diseases.

Keywords: cardiovascular system. automatic vascularization. human brain circulation. computational hemodynamics.

Resumo

Doenças relacionadas a AVC totalizam 11% das mortes mundiais, e técnicas de imagens médicas descrevem muitos aspectos da circulação cerebral. No entanto, a resolução limitada dessas técnicas atrapalha a avaliação de vasos sanguíneos menores. Modelos computacionais auxiliam nessa questão, provendo ferramentas para analisar cenários fisiológicos outrora inacessíveis. Este trabalho propõe um método para construir redes vasculares no córtex cerebral humano em diversas regiões da superfície pial e da matéria cinza. Uma versão adaptativa do Constrained Constructive Optimization que explora computação paralela gera vasos sanguíneos seguindo regras anatômicas. Uma geometria cerebral de um paciente real é usada como substrato geométrico e um modelo existente das grandes artérias é a base de onde a rede vascular é expandida. A geometria é particionada em três territórios independentes para cada grande artéria cerebral. Um volume fino da superfície pial teve seus vasos gerados até a escala de arteríolas de 50 mícrons de diâmetro de lúmen. A rede penetra a matéria cinza, e a vascularização é construída fixando-se amostras de sub-árvores para cada vaso terminal, que são geradas separadamente com propriedades associadas à matéria cinza. A rede final para o hemisfério esquerdo alcança 234 000 segmentos vasculares na rede pial, e 23.3 milhões de segmentos incluindo a matéria cinza. Os diâmetros de vasos na superfície pial variam entre 2100 µm e 26 µm, com terminais entre 50 µm e 60 µm. A rede resultante pode ser acoplada com modelos existentes do sistema cardiovascular para simular escoamento sanguíneo pulsátil e investigar as variações de pressão sanguínea ao longo do córtex cerebral em condições normais e patológicas. Essa nova abordagem propõe uma estratégia para entender microcirculação específica a pacientes em diferentes condições, permitindo analisar o risco de AVC, entre outros mecanismos envolvidos no início e progresso de doenças degenerativas.

Palavras-chave: sistema cardiovascular. vascularização automática. circulação cerebral humana. hemodinâmica computacional.

List of Figures

List of Tables

Contents

1 Introduction

1.1 Worldwide status of cerebrovascular diseases in 2024

Every year, millions of people die due to undiagnosed or untreated health conditions, and many others suffer from the lack of the proper tools to evaluate their medical treatment. Cardiovascular diseases are among the leading causes of death worldwide as claimed by statistics reports (FEIGIN et al., 2021), and cerebrovascular diseases, in particular, have increased their number of incidence by 70% between 1990 and 2019, accompanied by increasing healthcare burden. The second leading cause of death by total numbers is due to stroke, a cardiovascular condition where insufficient blood flow is provided to brain cells, causing cellular death among tissues in the body, being responsible for a total of 11% of deaths worldwide (FEIGIN et al., 2021). Figure 1 presents the incidence of strokes worldwide, highlighting the variation of incidences across different countries. Given this scenario, the onset and development of cardiovascular diseases are still a focus of research in this field, being of utmost importance to improve the quality of life.

Figure 1 – Total stroke incidence rate per 100 000 people by country.
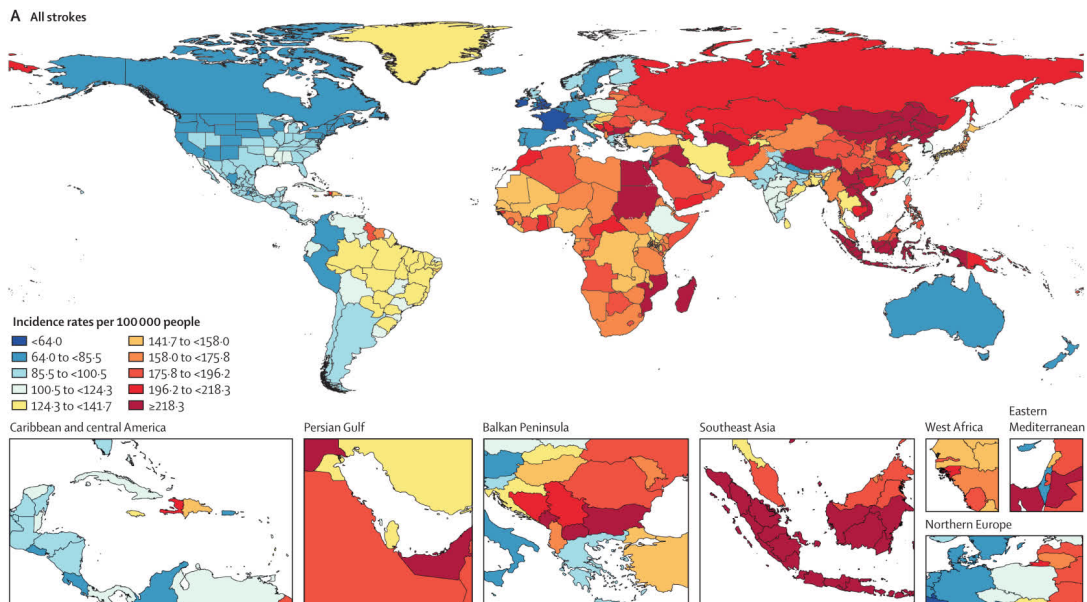
Source: (FEIGIN et al., 2021)

Given this situation, it is necessary to continue to develop methodologies to evaluate the onset and progress of cerebrovascular conditions, particularly for the brain. Previous studies have correlated the development of cerebrovascular diseases with blood flow in

the brain (BLANCO; MÜLLER; SPENCE, 2017), which may impact the functioning of the brain (FUJISHIMA et al., 1995) and result in anomalies or even neurodegenerative disorders (IADECOLA, 2004) These relations between cerebrovascular diseases and blood flow in the brain are explored in detail in chapter 2.

Therefore, proper modeling of the blood flow in the cerebral cortex is necessary to understand the functioning of the brain, and the causes for cerebrovascular disorders. This permits to simulate specific scenarios in a patient-specific basis, which is key to establish better actions to define therapeutic actions, determine prognosis, among others.

1.2   Computational models in the medical domain

The modeling of the cardiovascular system has evolved significantly in the last decades, powered by the advances in high performance computing. The current scenario allows the possibility to gain insight into the study of the whole body hemodynamics, and more particularly to investigate cerebral blood flow.

Taking into account the increasing power of high performance computers, and the existence of data systems for human physiology, a high degree of accuracy for modeling vascular networks can be derived from medical images extracted from real patients, and very valuable computer simulations can be performed to estimate in-vivo data from computational models (HARTUNG et al., 2018; REICHOLD et al., 2009; DIEM et al., 2016). They permit to describe and simulate physiological systems and their evolution with a high degree of accuracy in diverse scenarios of clinical interest. This interaction between physicians, and professionals in the field of scientific computing, allows the development of tools capable of assisting the analysis and diagnosis of pathophysiological phenomena, the development of patient-specific therapies *in-silico*, and the analysis of scenarios *in-vivo* for ongoing conditions (NADER et al., 2022; JAMES et al., 2006; BAUMBACH; HEISTAD, 1988). This results in the personalized medicine, which is assisted by modeling and simulation (LORTHOIS; CASSOT; LAUWERS, 2011), while promoting interdisciplinary values thanks to the combination of clinical data and scientific computing tools.

As a consequence, there is the possibility in experimenting dozens of conditions using simulation, by varying the parameters to achieve patient-specific problems, while taking into consideration the individual geometry of each person, resulting an augmented description of the potential mechanisms that could be taking place in the patient. While this may sound ubiquitous nowadays in clinical research, this was not the case a decade ago, especially in a world entering the permanent state of artificial intelligence, where medical data is scarce, and the evaluation of data obtained from *in-silico* modeling permits the training of AI models.

1.3   Problems and limitations in hemodynamic studies

Each new day, state-of-the-art equipment and techniques are brought forth to better empower the clinical environment and evaluate the conditions that may result in future cardiovascular events. Cerebral blood flow can be studied via the acquisition of data from medical images and various exams performed by personnel in the field, such as magnetic resonance imaging (MRI) (HEINZER et al., 2006), computerized angiotomography (JÓZSA et al., 2021) as seen in previous models for human brain circulation, or transcranial doppler ultrasonography (MALATINO et al., 1992) for visualization of vasoconstriction and blood flow velocity. *Post-mortem* techniques include microscopy, which permits the evaluation of geometrical aspects of microcirculation in the brain (CASSOT et al., 2006). While this everlasting race to improve healthcare in new generations exists, there are persistent limitations to how far technology can be employed to obtain data from patients in order to better characterize the pathophysiological conditions of the patient in general. This is the case for the construction of patient-specific hemodynamic modeling, where limitations in data hinders the characterization of the vascular domain where blood flow mathematical models are formulated.

A major limitation in the modeling of blood flow in the cardiovascular system is the missing smaller blood vessels in current models, where many pathologies typically unfold (BLANCO; MÜLLER; SPENCE, 2017), due to limitations in resolution of medical imaging and the high-risk of *in-vivo* invasive procedures in acquiring real data from patients. The non-invasive techniques, such as angiotomography, doppler ultrasonography, and magnetic resonance imaging, are highly useful to obtain geometrical descriptions of the major anatomical structures including larger blood vessels. (BERNIER; CUNNANE; WHITTINGSTALL, 2018) obtained the morphology of large cerebral arteries of 42 patients using angiography, showing existing heterogeneities along the cerebral vasculature. (REYMOND et al., 2009) presents a comparison of one-dimensional models of the systemic arterial tree, with the goal of validating these models, which will be discussed in chapter 2. However, the limitation in the resolution of these images are crucial for the creation of highly detailed vascular models.

Regarding the invasive techniques, *post-mortem* data is available thoroughly in the literature. (DUVERNOY; DELON; VANNSON, 1981) presents a highly-descriptive atlas of the cerebral arteries and veins in the pial surface obtained from brains of patients aging between 40 and 65 years. (Reina-De La Torre; Rodriguez-Baeza; Sahuquillo-Barris, 1998) uses scanning electron microscopy for 12 fresh brains for the gray matter vasculature, while (NONAKA et al., 2003a) and (NONAKA et al., 2003b) present the morphology of white matter cortical vessels. While these documents are highly descriptive of existing vascular structures of the human brain, obtaining vascular information *in-vivo* presents more limitations. This scenario is encountered in the study of patient-specific cases where

the existing conditions are located in places where access is limited.

Therefore, the characterization of the cerebrovascular network remains incomplete when studying the correlation between measurable quantitative parameters, such as blood pressure and flow, and the qualitative observations manifested in the form of the development of conditions and diseases. A more complete model of the cerebral vascular system is therefore highly desired to enable the study of large and small scale phenomena related to blood flow in arterioles and capillaries.

1.4   Previous works in the literature

This is not the first work to address the study of cerebral hemodynamics in the human brain cortex, and each previous work has had a different goal and scale in mind. Goals vary from the investigation of cerebral circulation, to the modeling of blood perfusion, and also the behavior of blood flow and pressure drop in capillary networks, and each contribution promotes a push towards the development of cortical brain circulation models.

Previous works have implemented optimization algorithms to generate blood vessel networks in rat brains. (LINNINGER et al., 2019) describes the cerebrovascular perfusion using compartment resistance models, and the continuation in (HARTUNG et al., 2021) presents a model of the cerebral cortex of a rat, created via computational models shown in figure 2.

Figure 2 – Synthetic arterial and venous network generated for a rat brain.
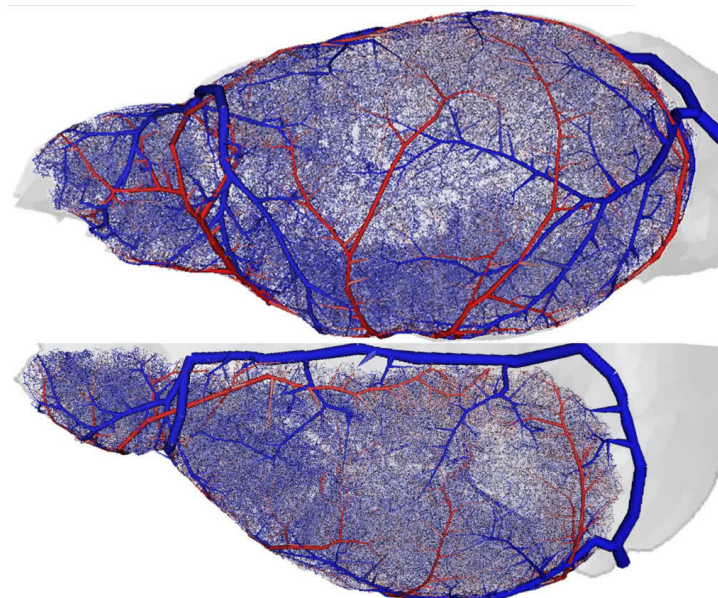
Source: (HARTUNG et al., 2021)

This resulted in the study of blood flow distribution along different regions of the rat brain, aiming to aid in quantification of blood flow and metabolism for the brain, for both arterial and venous blood vessels, coupled via a capillary network. Similar techniques can be employed in human-scale brain models to understand mechanisms targeting the outcomes of ischemic strokes.

Other works modeling the human cerebral vascularization include (JÓZSA et al., 2021), where the brain was modeled as porous media representing the circulation in the cerebral arterioles in different regions, and also in the capillaries, by varying the parameters of the blood flow in each domain of the media. The effect of collateral vessels was discussed in (OTANI et al., 2023) when obstructive lesions, such as ischemia or stenosis in blood vessels, are developed. This work studies the paths where blood may arrive for each region, and the existence of these collateral vessels permit the redistribution of blood flow via alternative means that does not encompass the damaged pathways. Their conduction of the study regarding patient-specific anatomy is also another key idea that is worth to be mentioned.

Now focusing on the smaller scales, in (GOULD et al., 2017), the main investigation was the analysis of pressure drop in a representative portion of the capillary vascular network of the cortical brain matter. Their conclusion was that the smaller vascular network, i.e. the capillary bed, is responsible for the largest pressure drop in the brain circulation, and while these vessels have shorter length, it is noticeable that the diameter of these capillary networks is significantly smaller than the larger vessels, and therefore the resistance of blood flow inside them is comparatively larger.

(PADMOS et al., 2021) goes further and combines image-based patient specific data with literature models to expand vessels not visible, and model the pial surface hemodynamics. Their goal is to study ischemic stroke and set up *in silico* trials for treatment. One-dimensional blood vessel models are coupled to 3D perfusion models of the brain tissue to perform patient-specific simulations. (REICHOLD et al., 2009) modeled the cerebral blood flow using a vascular graph in a grid representative of the brain tissue, permitting to compute blood flow and scalar transport realistically. Sections of penetrating cortical arterioles are simulated. (KÖPPL; VIDOTTO; WOHLMUTH, 2020) generates microvascular networks from larger vessels to construct a surrogate network analog to the real vasculature using automatic algorithms, in a 3D-1D coupled model that accounts for blood and oxygen pressure, and the porous medium for the brain tissue.

1.5 General motivation and goal of this work

This work aims to use modeling techniques to characterize the cerebrovascular network and allow the simulation of blood flow in such networks, as a mean to provide

tools to understand the physiological and pathological phenomena, and to correlate the risks of development of cerebrovascular diseases, as well as to study the interaction of blood flow and neural activity. For that, the generation of arterial networks via automatic algorithms permits the continuation and expansion of existing blood vessel models into a more complete model of the cardiovascular system.

Given the difficulty of obtaining descriptions of smaller vessels in the human cerebral cortex, the aim is to construct a highly-detailed representation of these vascular segments to study brain hemodynamics, starting from larger arteries and going down to the scale of microns in vessel diameter. The methodology proposed here aims to extend current models of the arterial network in the human cerebral cortex by building massive anatomically consistent arterial networks, first through the generation of a highly-detailed vascular network in the pial surface of the human brain, and second through the incorporation of descending arterioles that penetrate the gray matter, following from the terminal vessels of the pial network, into the gray matter region. The third goal is to generate structures that perfuse the gray matter around each arteriole, vastly increasing the resolution of the network into the millions of blood vessels, and finally, we evaluate the diameters and the pressure drop to verify the agreement in terms of some global markers, with the available literature, targeting the same order of vessels found in the literature (HARTUNG et al., 2021; SCHMID et al., 2019).

The final target of this work is to create a cerebrovascular model that permits the study the hemodynamic environment and its heterogeneities along the cerebral cortex, by the use of this expanded model in patient-specific simulations of blood flow in the cerebral region, and allow investigation to correlate cerebrovascular diseases and hemodynamic environments.

1.6   Contributions of this work

The quantitative characteristics of the human brain from the literature describing the cerebrovascular system are explained in chapter 2. Also, automatic vascularization algorithms, such as the constrained constructive optimization (KARCH et al., 1999), provide the tools used to properly construct the dense vascular network based on a set of fundamental laws, as explained in chapter 3. The method employed in this work consists in using the Constrained Constructive Optimization algorithm (CCO) (KARCH et al., 1999), and the version used is called Parallelized Adaptive Constrained Constructive Optimization (PDCCO) (CURY et al., 2021), which permits the flexibility required to deal with the complexity found along the brain cortex. Another point, is the possibility of generating massive vascular networks via parallelization conducted in separate partitions accelerating the workflow.

The specific novelty here is due to the combination of a patient-specific geometric model of a cerebral cortex model employed for this work with existing vascular data from the literature (BLANCO et al., 2015), these considerations are better illustrated in the chapter 4. The third pillar is the application of the PDCCO algorithm to build network down to the level of gray matter arterioles, going through the outer layers of the brain, and the penetration into the gray matter, creating a full brain vascular network. More details about the generation can be obtained in chapter 5.

Following the automatic vascularization, one-dimensional pulsatile blood flow simulations for the pial network can be conducted using the methodology in (MÜLLER et al., 2016) and (BLANCO et al., 2020), by coupling the network built in this work to the existing ADAN model (BLANCO et al., 2015) to investigate and quantify circulatory phenomena in the cerebrovascular system. Chapter 6 wraps the text to summarize the main contributions of this work.

The impact of this work includes the incorporation of such models as auxiliary tools that assist research in physiology and clinical domains, allowing the investigation of blood flow phenomena beyond the capabilities of current models in literature to understand the mechanisms that originate cerebrovascular diseases, and simulate them to expand the frontier of knowledge regarding the onset and progress of these diseases, as well as to promote the development of alternative therapeutic strategies. This work is a first step towards a complete cerebral hemodynamic simulation, employing massive networks across cerebral regions to understand the multiscale nature of the circulation in the brain, which is a fundamental ingredient for the study of vascular lesions, strokes, substance transport, hypertension, stenosis, among other pathologies.

2 The human brain circulation

2.1 Anatomy of the human brain

The human brain is an organ of the nervous system, which exerts the functions necessary to body control, sensory perception, movement, and cognition (SCHÜNKE; SCHULTE; SCHUMACHER, 2010). It comprises two hemispheres, interconnected via the corpus callosum in the middle, while the brainstem in the center is connected to the cerebellum and the spinal cord, from where connection to the rest of the body is achieved. Despite weighing 2% of the body mass, it receives 20% of the cardiac output (SCHMID et al., 2019), and consumes 25% of the total energy and oxygen of the body. This is due to the high cellular activity in the cortical regions of the cerebral tissues, where the high quantity of brain cells require the necessary nutrients to perform their metabolism. Figure 3 presents the anatomy of the brain and the division in its respective lobes.

Figure 3 – Sagittal view of the brain subdivided in lobes.
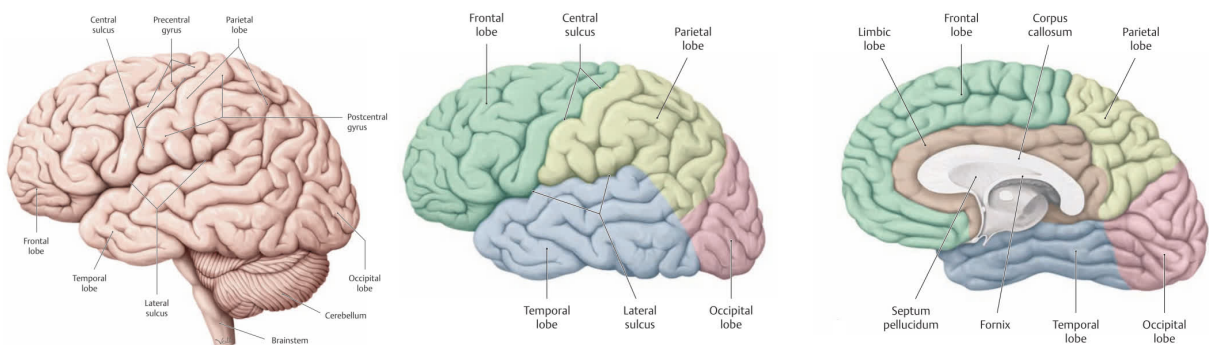
Source: (SCHÜNKE; SCHULTE; SCHUMACHER, 2010). Left: sagittal view of the brain with the cerebellum included; center: subdivision in lobes; right: sagittal section in the middle of the brain.

Morphologically, the brain is composed of convex and concave structures, named gyri and sulci respectively, to maximize the outer surface of the brain where the gray matter lays, and the number of neuroglial cells (SCHÜNKE; SCHULTE; SCHUMACHER, 2010). They are shown in figure 3. The outer layer of the brain is surrounded by a liquid denoted the cerebrospinal fluid, and this layer is called the pial surface of the brain, which is formed by the exterior boundary of the gray matter, extending along the gyri and sulci. Figure 4 shows the pial surface of the brain where major arteries run along.

The brain cortical matter is composed of two different tissues. The first is the gray matter disposed on the outer layer, where most of the nervous cells are located, and which

Figure 4 – Pial surface of the brain including its major arteries.
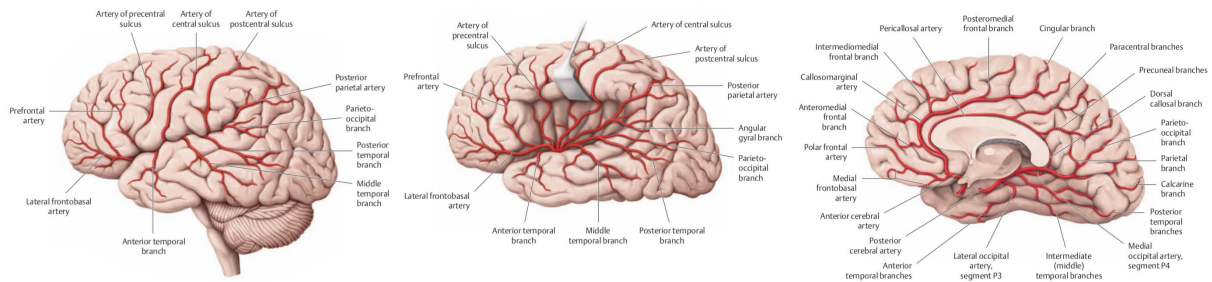
Source: (SCHÜNKE; SCHULTE; SCHUMACHER, 2010). Left and center: sagittal view; right: sagittal section in the middle of the brain.

is responsible for high neural activity. The white matter is located underneath, where similar structures exist, however in different compositions, having a larger percentage of cellular fat when compared to cortical nervous cells, which gives its characteristic white color (SCHÜNKE; SCHULTE; SCHUMACHER, 2010). Figure 5 shows the disposition of the gray and white matter tissues.

Figure 5 – Gray and white matter tissues in the brain.
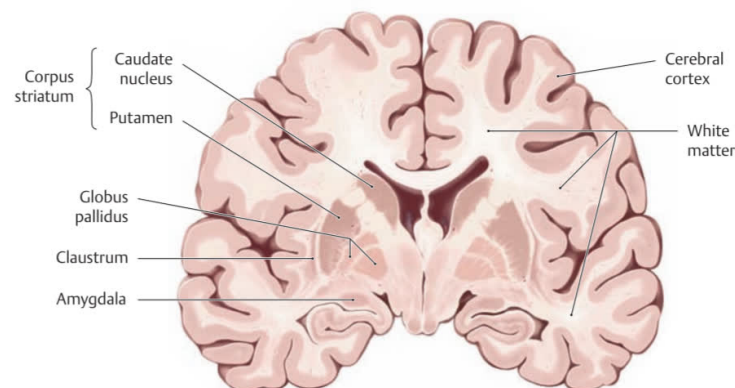
Source: (SCHÜNKE; SCHULTE; SCHUMACHER, 2010). Coronal section. Gray matter is denoted as "Cerebral cortex".

The tissues of the brain contain neuroglial cells from the nervous system, and blood vessels from the cardiovascular system, and they are the fundamental substrate that enables proper neurological functions in the brain. The combination of these two systems, nervous and cardiovascular, constitute the fundamental substrate that enables proper brain function, in a convoluted way that is commonly referred to as a neurovascular units (SCHAEFFER; IADECOLA, 2021). This interlacing of neuroscience and the cardiovascular system permits to study the connections between vascular strokes and neurodegenerative diseases, their

correlations and causes, thus elucidating the necessity of studying hemodynamic conditions in order to properly understand the neurological behavior of the brain and vice versa.

(IADECOLA, 2017) reviews this relation of the neurovascular units, and in (IADECOLA et al., 2023) the symbiotic relation between the cardiovascular and neurological systems are presented in the neurovasculome, that includes the lymphatic system. Their results suggest that pathogenic mechanisms in the neurovasculome are linked to cognitive dysfunction and neurovascular and neurodegenerative diseases. When studying the coupled behavior of such systems, it becomes possible to model and simulate the neural and metabolic integration, and investigate mechanisms once inaccessible or difficult to reach.

2.2   Description of the cerebrovascular system

The brain has a high demand of energy provided by an extensive network of blood vessels that permeate the gray and white tissues, and this complex demand is not only patient-specific dependent, but also features higly variable time and spatial variability. In a nutshell, the cerebrovascular arterial system starts with large backbone arteries, that transport blood to the brain, and the pial arteries, that distribute the blood over the pial surface. Penetrating arteries descend into the tissues, and sprout into smaller capillary blood vessels with thin walls that permit the exchange of substances with the surrounding cells. This network of vessels is connected back to the venous system (HARTUNG et al., 2021).

Figure 6 presents a scheme of the arterial anatomy if a coronal section of the brain, with highlight to each different type of artery (SCHAEFFER; IADECOLA, 2021).

In more detailed terms, each hemispherical cortex is subdivided in into three major vascular sub-regions where each region receives blood from one of the three major cerebral arteries (SCHÜNKE; SCHULTE; SCHUMACHER, 2010). These vessels are named the Anterior (ACA), the Middle (MCA), and the Posterior Cerebral Artery (PCA), and their territories are presented in figure 7. The three cerebral arteries originate from segments in the Circle of Willis, which is an internal loop-shaped circuit located at the base of the brain, and receives blood anteriorly by the pair of internal carotid arteries, and posteriorly by the basilar artery. These major cerebral arteries and their bifurcations are responsible for providing blood flow to the vascular territories in the brain cortex, first by running along the convoluted pial surface of the brain, and later by bifurcating into smaller vessels to maximally cover the brain surface (DUVERNOY; DELON; VANNSON, 1981). Figure 8 depicts this coverage.

After reaching diameters in the range of 50 µm, supply of blood into the inner layers of the cerebral parenchyma is achieved via bifurcations in smaller terminal branches

Figure 6 – Different arteries in the brain.
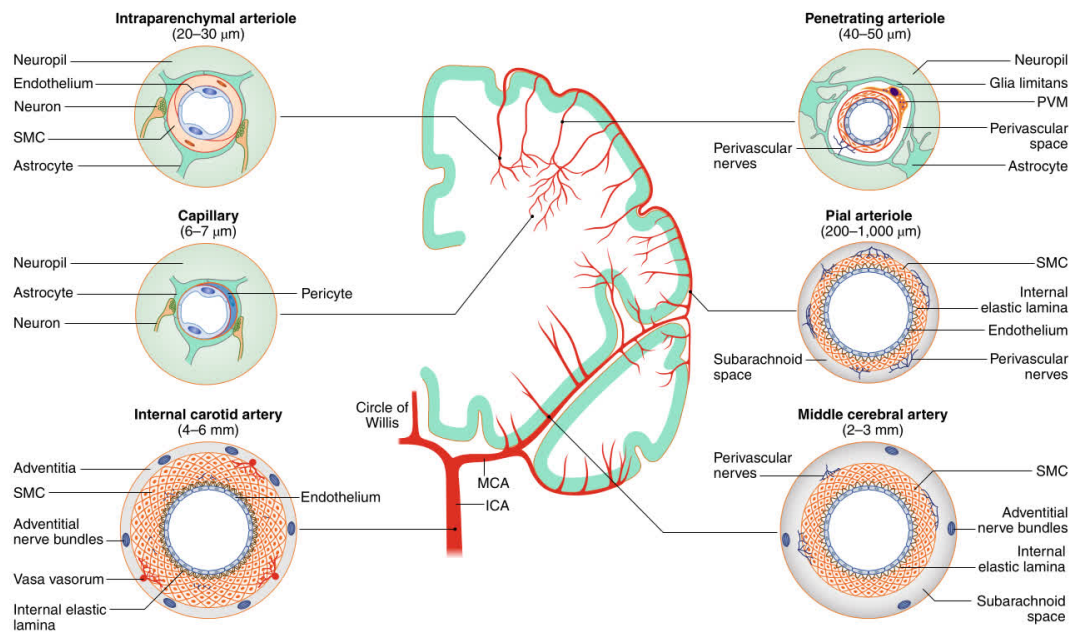
Source: (SCHAEFFER; IADECOLA, 2021). Coronal section for the MCA branch.

of the pial network. These bifurcations penetrate the gray and white matter tissues inwards via penetrating arterioles, also called descending arterioles in the literature (LAUWERS et al., 2008). It is estimated that the human cortex has a density of around 1 arteriole per mm² (SCHMID et al., 2019). The penetrating arterioles are shown in figure 9.

These penetrating arterioles that form cortical columns vascularize the region surrounding them by bifurcating into dense and massive networks of arterioles and capillaries (Reina-De La Torre; Rodriguez-Baeza; Sahuquillo-Barris, 1998) permeating the gray and white matter in a radial manner to feed the neuroglial cells and interstitial space with nutrients and oxygen.

The blood vessels in the microvascular network feed the brain tissues via vessels in the form of arterioles, capillaries, and venules. In these smaller blood vessels, the Fahraeus-Lindqvist effect (FÅHRÆUS; LINDQVIST, 1931) describes the variation of blood viscosity when the lumen and the red blood cells are in the same order of scale. Scalar transport in the tissues happens via the interstitial space (RAY; HEYS, 2019) and the draining of metabolic waste is hypothesized to happen via the perivascular circulation (RAY; HEYS, 2019).

Removal of deoxygenated blood after the cellular metabolism is performed similarly in reverse. Ascending venules remove the blood from the tissue outwards to the veins laying over the pial surface, and after that they join back into larger cerebral veins that conduct

Figure 7 – Arterial territories in the brain.
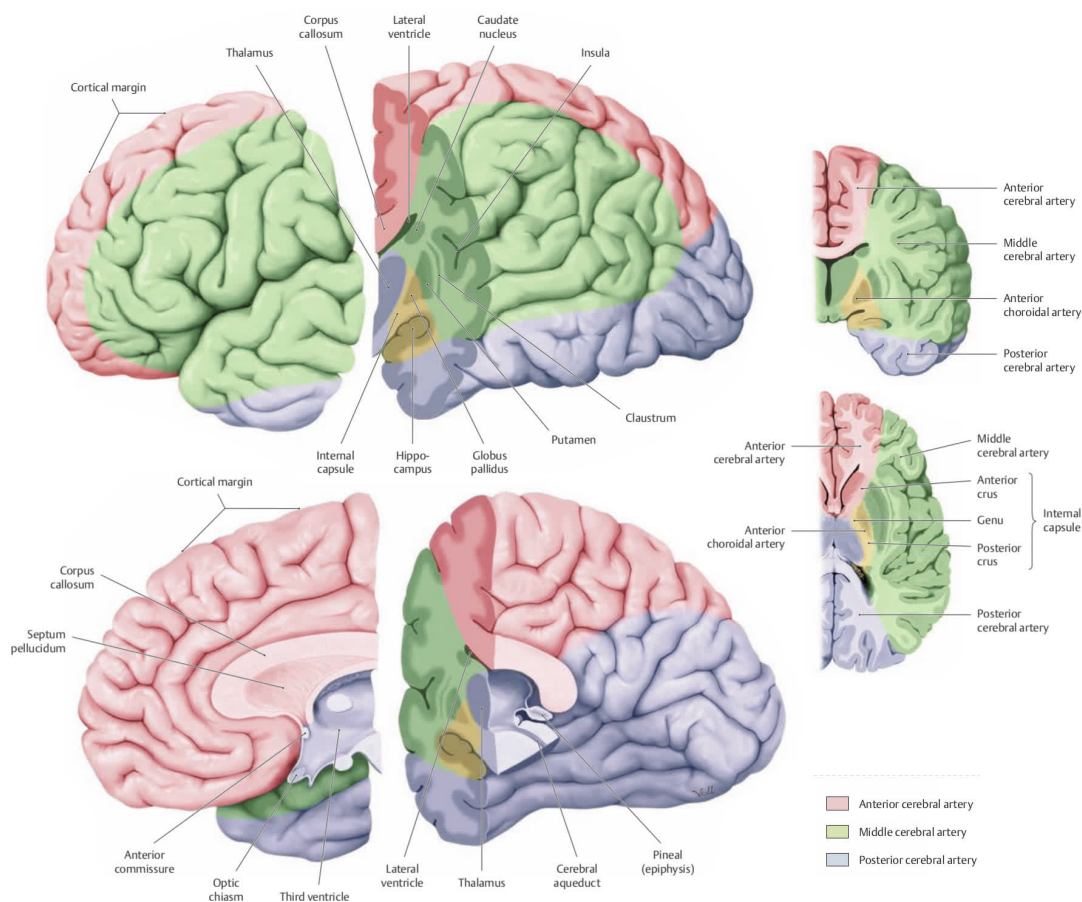
Source: (SCHÜNKE; SCHULTE; SCHUMACHER, 2010). Top left: sagittal view; bottom left: sagittal mid-section slice; top right: coronal section; middle right: transverse section.

the blood back to the main circulatory system (DUVERNOY; DELON; VANNSON, 1981).

2.3 Pathologies and conditions in the brain

Neurons and blood vessels in the brain are both intrinsically related to the behavior and functioning of the body, and previous works have correlated the functioning of neurovascular units and the impact on health and cognitive conditions (IADECOLA et al., 2023), therefore dysfunctions in one system result in anomalies in the other.

Strokes are interruptions of blood flow in the brain caused by diverse factors, but commonly with risks associated with hypertension, diabetes, unhealthy diet, obesity, smoking and sedentarism (FEIGIN et al., 2021). As mentioned before, it is the second largest cause of death in the world accounting for 11% of the total deaths worldwide, only following heart ischemia (IADECOLA; ANRATHER, 2011). The consequences of

Figure 8 – Drawing of the cortical pial vasculature.
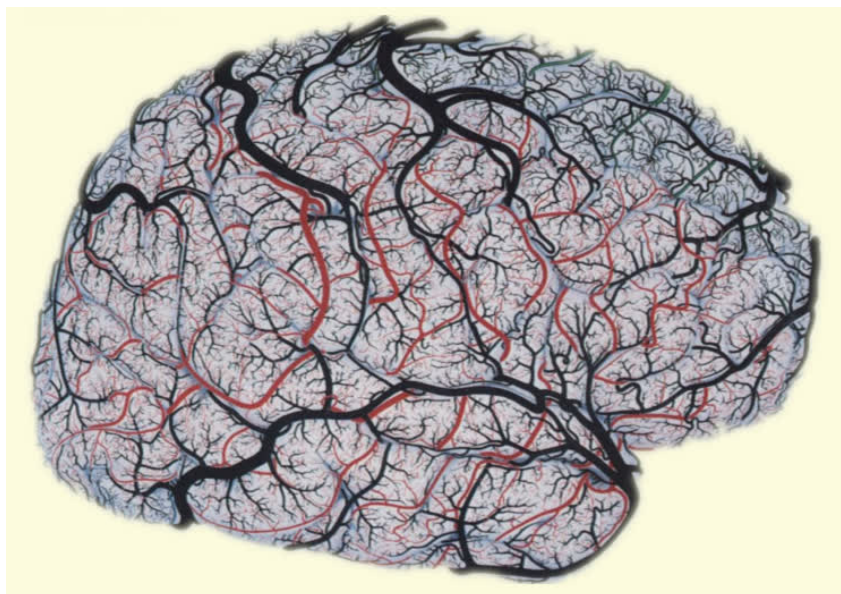
Source: (DUVERNOY; DELON; VANNSON, 1981). Right hemisphere, arteries are shown in red (MCA), green (ACA), and blue (PCA), veins are shown in black.

Figure 9 – Penetrating arteries in the cerebral cortex.
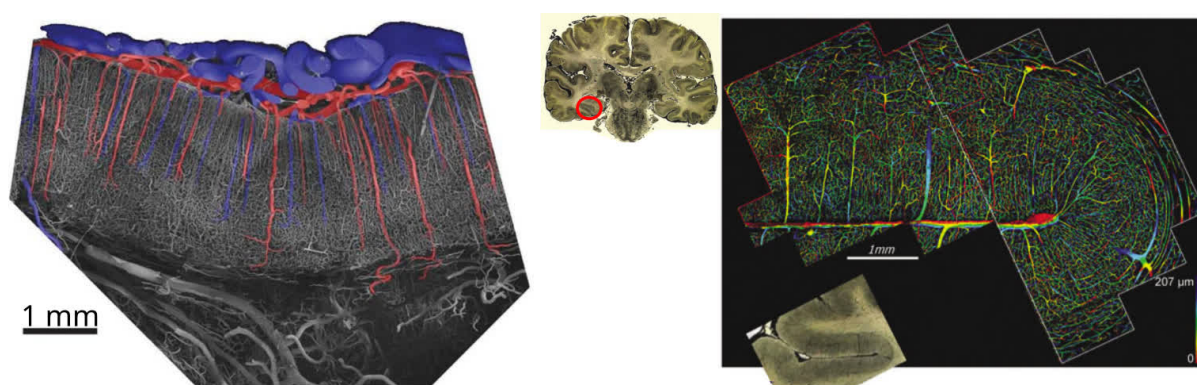
Source: (HIRSCH et al., 2012) (left), (CASSOT et al., 2006) (right). Left: Scanning electron micrograph of penetrating arterioles in a monkey's visual cortex, arteries in red, veins in blue. Right: ink-injected human brain section of a temporal lobe sulcus with penetrating arterioles, reconstructed by confocal microscopy.

Figure 10 – Scanning electron micrography of blood vessels in the cortical gray matter.
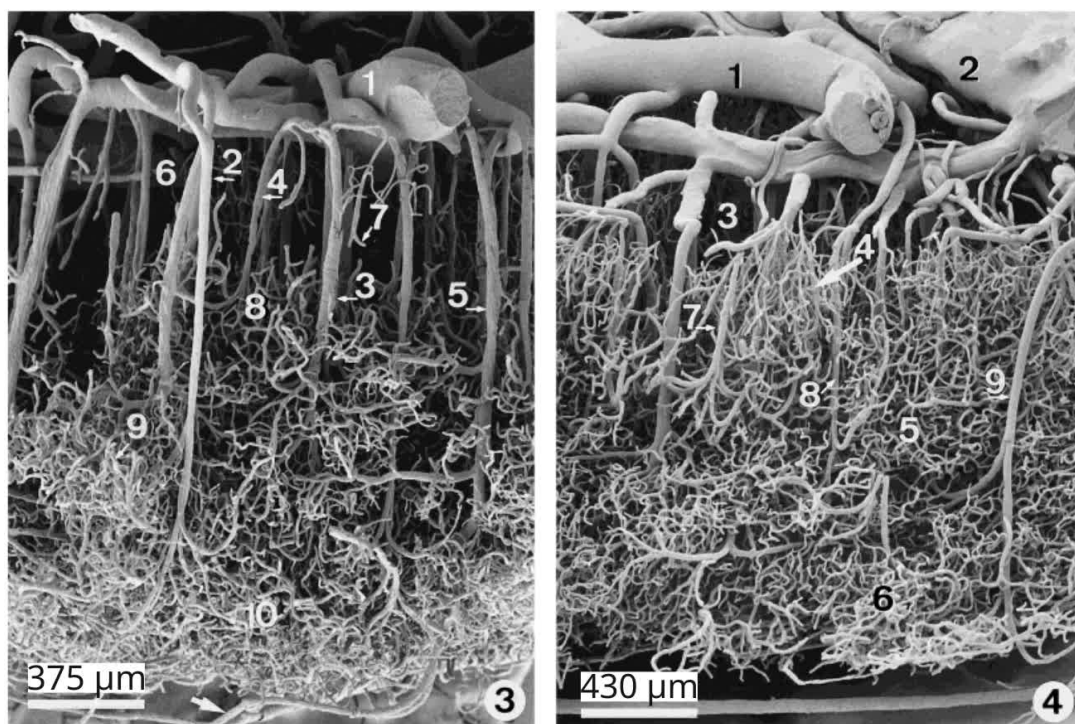
Source: (Reina-De La Torre; Rodriguez-Baeza; Sahuquillo-Barris, 1998). Temporal (left) and occipital (right) lobes. Both arteries and veins are depicted.

ischemic strokes can cause several secondary complications, such as inflammations, which may potentially cause more ischemic strokes. This positive-feedback loop impacts the health of stroke survivors (IADECOLA; ANRATHER, 2011). One type of occlusion in blood vessels that causes strokes is stenosis, i.e. the irregular narrowing of blood vessels due to lesions, which reduces the lumen area of the blood flow, which is the sectional area where the flow of blood occurs. This condition impacts both stationary and pulsatile blood flow (STERGIOPULOS; YOUNG; ROGGE, 1992) and results in the variation of the distribution of pressure in the cardiac cycle for the human brain, altering the well-functioning of the organ. Studies for the simulation of blood flow altered by this condition are then fundamental to understand how the pressure drops after the narrowed gap. Occlusions, and particularly stenoses, affect the downstream blood flow, causing lack of oxygen, and therefore brain ischemia. For that, a proper model to measure the areas affected along the cerebrovascular system is fundamental to quantify the extension of the damage in question.

The pathogenesis of small vessel disease, another common pathology of the brain, are highly linked with the blood pressure gradients in the cerebrovascular system (BLANCO; MÜLLER; SPENCE, 2017) and irregular patterns of the pressure field in the cerebral

cortex may result in different mechanisms that lead to such a pathological condition. The study of distribution of pressure in the brain helps understand the mechanisms that may contribute to the development of this condition.

Hypertension is the condition defined by the increase of pressure in the blood vessels, that may be the result of vessel diameter constriction, capillary rarefaction, among other systemic alterations, and is, at the same time, a vascular condition and a risk factor for several cerebrovascular diseases mentioned here. One of the effects is the hypertrophy of larger cerebral arteries in the brain, resulting in attenuation of blood pressure downstream (BAUMBACH; HEISTAD, 1988), and distension of the sectional area. This larger vascular section, however, could result in blood pressure lower than the ideal during rest or sleep, which subsequently may trigger other conditions, and may also cause tissue hypertension over the brain parenchyma, predisposition to ischemia, and compromise of the entire cerebrovascular network. Lesions in the white matter tissue are also present in elderly patients with hypertension (FUJISHIMA et al., 1995), and the effects of anomalous pressure in the brain also impairs metabolism of neuroglial cells, and cognition. The resistance of peripheral vessels also contributes to increase this problem in the smaller vessels (HEAGERTY et al., 1993), where the vascular network tends to remodel itself to accommodate the high pressures beyond the essential values for proper functioning, resulting in an alteration in the lumen to media ratio, where the media is the blood vessel wall thickness.

Alzheimer's disease is a neurodegenerative condition that causes the deterioration of nervous cells in the human brain tissues, whose consequence is a permanent and irreversible state of the organ resulting in loss of synapses and neurons due to the deposition of non-soluble $A\beta$-Amyloid proteins in the brain, causing the replacement of the original tissue (DAYEH; LIVADIOTIS; ELAYDI, 2018). Around 60% to 70% of the causes in dementia are related to this condition. Several studies have correlated the blood pressure with the development of Alzheimer's disease (GENTILE et al., 2009), and have proposed to model the development of the condition (DIEM et al., 2016; DAYEH; LIVADIOTIS; ELAYDI, 2018) in order to understand how this deposition occurs in the brain and how cleanse of metabolic waste can be performed (RAY; HEYS, 2019). This condition is highly linked with cerebrovascular anomalies (IADECOLA, 2004) and blood system dysregulation is a feature of this disease, therefore the study of blood flow is intrinsically linked with this neurodegenerative condition.

Parkinson's disease is the second most common neurodegenerative disease after Alzheimer's, and is also an irreversible condition caused by deposition of $A\beta$-Amyloid in the brain (LIM et al., 2019), and causing dementia. Vascular Parkinsonism also initiates with small vessel disease, and presents vascular conditions as a risk factor for its development (NARASIMHAN; SCHWARTZ; HALLIDAY, 2022), therefore the connection between

vascular diseases and Parkinsonism is still matter of study.

The common thread unifying the onset and development of these cerebrovascular diseases is the set of mechanisms related to the blood flow and pressure in the brain, therefore the study of the vascular structures with details in the cerebral cortex is necessary to better understand these phenomena, and as well as to investigate the coupling between hemodynamics and neural actovity in both, normal and abnormal conditions.

2.4 Brain imaging techniques

Brain imaging is the set of techniques used to visualize the current state of a patient's brain components, including cerebral perfusion, tissue composition, and vascular description of the larger blood vessels. There are a few common techniques employed for this goal, including magnetic resonance imaging (MRI) (HEINZER et al., 2006), computerized angiotomography (JÓZSA et al., 2021), transcranial doppler (MALATINO et al., 1992), and electron microscopy (CASSOT et al., 2006), as briefly mentioned in chapter 1. Depending on the technique employed, they are used to study different aspects of hemodynamics, allowing to quantify effects from the larger pial arteries (BERNIER; CUNNANE; WHITTINGSTALL, 2018) down to capillaries (GOULD et al., 2017), showing, for example, that the largest resistance to circulation occurs in capillaries with low diameter (d<10 µm).

For larger structures, magnetic resonance (MRI) techniques can be used to investigate macro-scale phenomena, but at the expense of lowest resolution, since these have a limitation in the pixel size and the instruments. These techniques, however, permit to clinically correlate anatomic conditions with stroke (TATU et al., 1998), especially by using MRI to analyze larger anatomic structures, and the brain blood supply through perfusion maps. (BERNIER; CUNNANE; WHITTINGSTALL, 2018) presents a detailed magnetic resonance angiography of the human cerebrovascular system, for both arteries and veins, showing the heterogeneity of larger vessel densities in the brain arteries. This study allows the characterization of the cerebral tissue and the density of arteries, veins, and cerebrospinal fluid, in an atlas of the human cerebrovascular system, divided in sub regions, in order to quantify the gray and white matter properties. (SCHMID et al., 2019) characterizes anatomical and functional features of the brain cortex vasculature and uses this data to discuss important implications for calibration of MRI techniques.

Electron microscopy can be used to study smaller vessel phenomena, but the region evaluated is extremely limited to the sample that is used, and present a local evaluation, not a global one. (CASSOT et al., 2006) uses electron microscopy to analyze capillary size, frequencies and distribution of diameters and lengths of small blood vessels, in order to obtain data and understand aspects of microcirculation (see figure 9). (HEINZER et al.,

2006) cites the limited number of regions of interest in microscopy as a limiting factor of this technique, and proposes hierarchical imaging as a solution to obtain images for both larger and smaller scales of the human brain, combining tomography and microscopy together. Figure 11 shows this solution combining micro-computed tomography (µCT), synchrotron radiation µCT (SR µCT), and scanning electron microscopy (SEM).

Figure 11 – Hierarchical imaging of the cerebral vasculature.
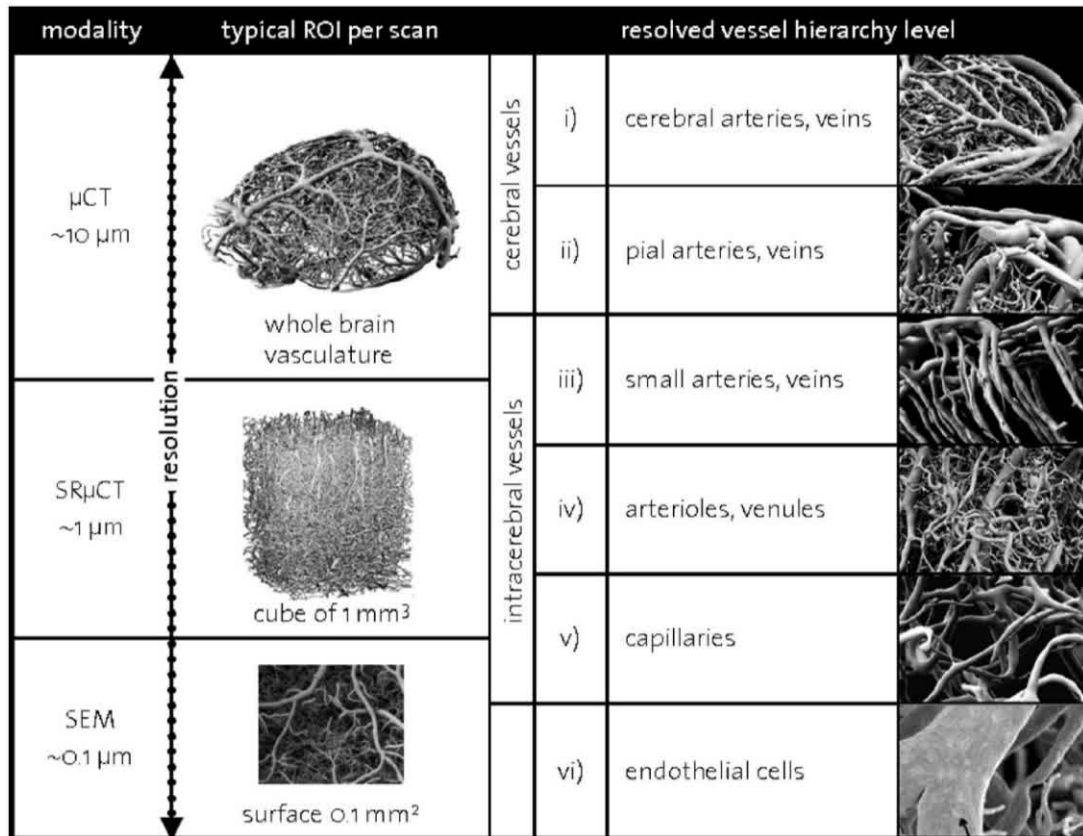
Source: (HEINZER et al., 2006).

(LEE, 1995) compares both human and rat cerebrovascular morphology via microscopy to show similarities and conclude that rat offers good models for studying human cerebrovascular diseases. (Reina-De La Torre; Rodriguez-Baeza; Sahuquillo-Barris, 1998) identifies arterial vessels in the cerebral cortex via electron microscopy, (see figure 10) that are characterized by penetration length and vascular layer densities, as reported previously by (DUVERNOY; DELON; VANNSON, 1981). (NONAKA et al., 2003b) combines x-ray techniques with microscopy to analyze anastomoses in the deep white matter and understand mechanisms related to ischemia pathological lesions.

These techniques complement each other. The problem, however, lies when coupling the data for larger and smaller vessel hemodynamics, because the coupling between vastly different scales is difficult to obtain. Such a link between different scales could be established

through the construction of vascular models, filling the gap and providing an alternative to build whole-organ vascular models.

2.5 Vascular models of the brain

Currently, hemodynamic models of the human circulation, have been proposed in the literature, and their description has allowed the understanding of mechanisms that describe hemodynamic patterns in the human brain. They can be used to study the pressure levels across different regions in the brain, particularly in the cortex and the brainstem, permitting the study of criteria for hypertension. The high degree of complexity of spatial and temporal scales presents itself as a challenge in modeling cerebral circulation. While current models allow to describe with high level of detail the human body blood flow for large and medium-sized arteries, blood flow in smaller arterioles, where pathologies commonly unfold, is difficult to model.

The Avolio model (AVOLIO, 1980) is a cardiovascular model of the human body that contains 128 arteries in total, and has been used for compartment type simulations, when a single vessel is treated as an entity with spatially-condensed properties. Other models, such as (STERGIOPULOS; YOUNG; ROGGE, 1992) contain 55 arteries used for one-dimensional simulation of the arterial network, i.e., when the properties vary along the axial dimension of the blood vessel, resulting in a much more detailed description of the hemodynamics. Figure 12 shows these two models for the arteries of the human body.

Figure 12 – Arterial models of the human body.
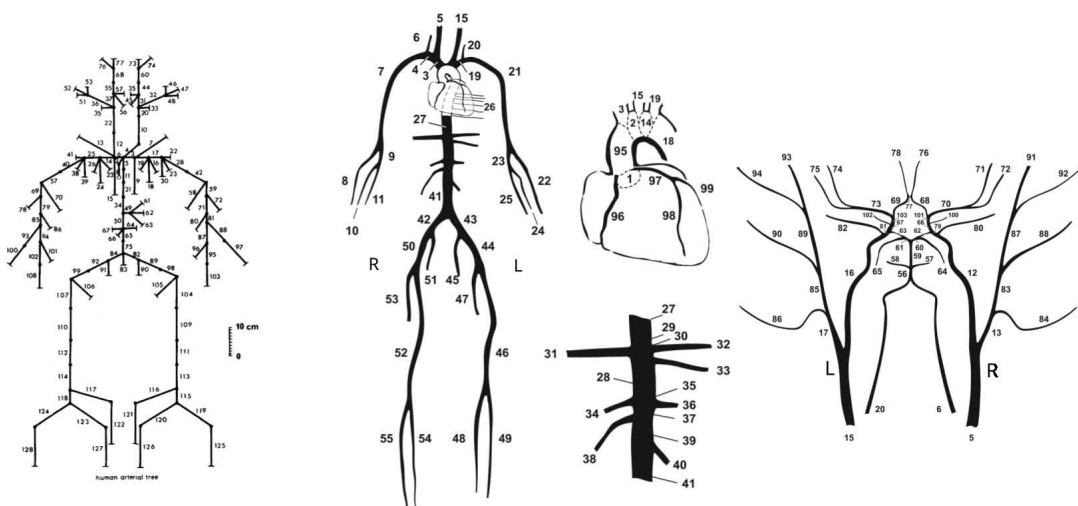
Source: (AVOLIO, 1980) (left) (REYMOND et al., 2009) (right).

The Anatomically Detailed Arterial Network model (ADAN) (BLANCO et al., 2015) is a state-of-the-art model and a highly descriptive arterial cardiovascular model of

the entire human body, including over two thousand arteries. Its description comprises the entirety of the human cardiovascular system, and permits the one-dimensional simulation of blood flow in the vascular segments with a high degree of detail, allowing the study of pulsatile blood flow propagated through the body. Figure 13 shows an illustration of the ADAN model, with highlight for the arterial network in the head.

Figure 13 – ADAN: the Anatomically Detailed Arterial Network model.
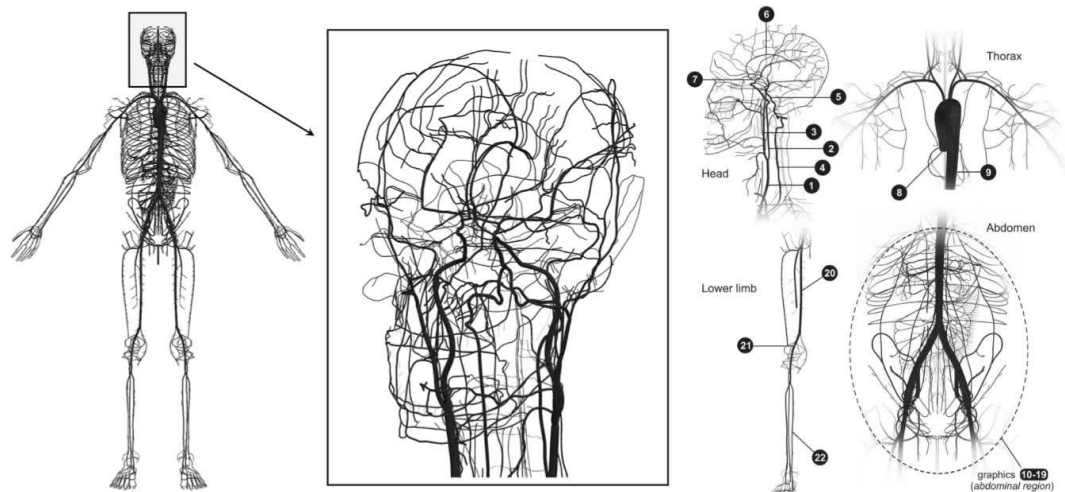
Source: (BLANCO et al., 2015; BLANCO et al., 2020). Left: ADAN model for the complete body; center: zoomed-in arterial network in the head; right: arterial networks for other parts of the body.

An even more recent model, the Arterial-Venous model (ADAVN) (MÜLLER et al., 2023), contains veins alongside arteries for the entire human body, allowing also the study of the circulation in the venous vascular network in different regions of the body. Figure 14 shows the ADAVN model.

Although the cerebrovascular network in the ADAN model includes many branches of the ACA, MCA and PCA that run over the pial surface, and permit the simulation of blood flow with a high degree of detail, the description of the smaller vessels that cover the entire pial surface down to the level of descending arterioles is not present in the model, imposing a limit to the scale of events that can be modeled in the human brain. This makes it impossible to describe the complete blood flow phenomena in smaller vessels, and the study of pathologies that commonly unfold in these scales is hindered, since smaller arteries beyond the larger scales are needed to fully comprehend the behavior of the cerebral circulation. Therefore, an expansion of the cerebrovascular network in these models is of the utmost importance, and this is why the use of automatic algorithms for the expansion of existing cardiovascular models in the literature is highly valuable.

Figure 14 – ADAVN: the Anatomically Detailed Arterial-Venous Network model.
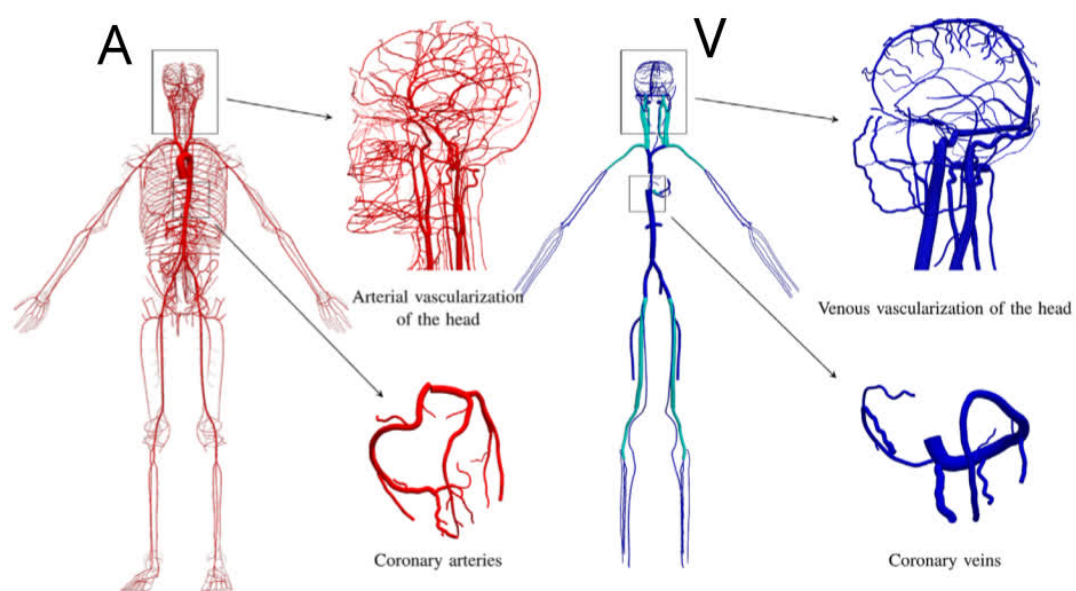
Source: (MÜLLER et al., 2023). Left: Arterial model; right: venous model.

3 Constrained Constructive Optimization

3.1 Automatic generation of vascular trees

In order to circumvent the limitations of data acquired from medical images, diverse methods have been proposed to model the circulation in the human brain. As viewed in chapter 2, the reconstruction technique used for blood vessels depends on the spatial scale considered (HEINZER et al., 2006), since different scales demand specialized techniques according to anatomical observations.

One class of automatic algorithms to build vascular networks is given by fractal methods (ZAMIR, 1999; ZAMIR, 2001), considering the general properties of blood vessels in a particular tissue, regardless of the geometry of the organ. An alternative strategy for generation of blood vessels, however, is via the use of space-filling optimization algorithms, where the geometry is considered when generating the network of blood vessels for a specific organ, and this sequential generation is commonly evaluated by using a metric. This permits the continuation and expansion of existing blood vessel models into a more complete representation of the cardiovascular system.

When dealing with large arteries, image techniques can be used to reconstruct the vascular network (HEINZER et al., 2006), and obtain their distribution along the cortical domain (BERNIER; CUNNANE; WHITTINGSTALL, 2018). Regarding medium-sized and smaller arterioles, automatic vasculature growth algorithms, such as the Constrained Constructive Optimization (CCO) (SCHREINER, 1993; SCHREINER; BUXBAUM, 1993), are much more promising for reconstructing the blood vessel network. The formalization of the algorithm for three-dimensional spaces (KARCH et al., 1997) allows the use of the technique for blood vessel network generation in vascular territories.

In the face of the limitations of the current vascular models of the human brain, and the limitations of imaging previously discussed, it is desired to vascularize the 3D regions of the human brain via an automatic algorithm to extend the larger cerebral vessels into smaller segments that perfuse the human brain tissues down to more refined scales. For this, the Constrained Constructive Optimization technique (SCHREINER; BUXBAUM, 1993) is highly valuable as a method to create these fine blood vessels in an anatomically consistent manner within a three dimensional domain of the human cortical brain.

3.2 The Constrained Constructive Optimization

3.2.1 The method

The Constrained Constructive Optimization (CCO) algorithm is a computational method used to generate a realistic network of blood vessels embedded in a predefined geometrical domain (KARCH et al., 1999). The CCO iteratively fills the bounded space with a sequential appending, and connecting, of blood vessel segments in a way that mimics the anatomical structure of the region, following a set of constraints, or fundamental rules, inspired by the biological and anatomical structure of the real vasculature (SCHREINER et al., 1996). Figure 15 shows a 3D visualization of a vascular tree generated using the CCO algorithm. Some examples of constraints are the vessel bifurcation laws, the geometrical limitations for aspect ratio of vessels (KARCH et al., 1999), boundary penetration, predetermined inlet and outlet flow (BLANCO; QUEIROZ; FEIJÓO, 2013), total resistance of the network (LINNINGER et al., 2019), among others (TALOU et al., 2021).

Figure 15 – CCO-generated arterial network in a spherical domain.
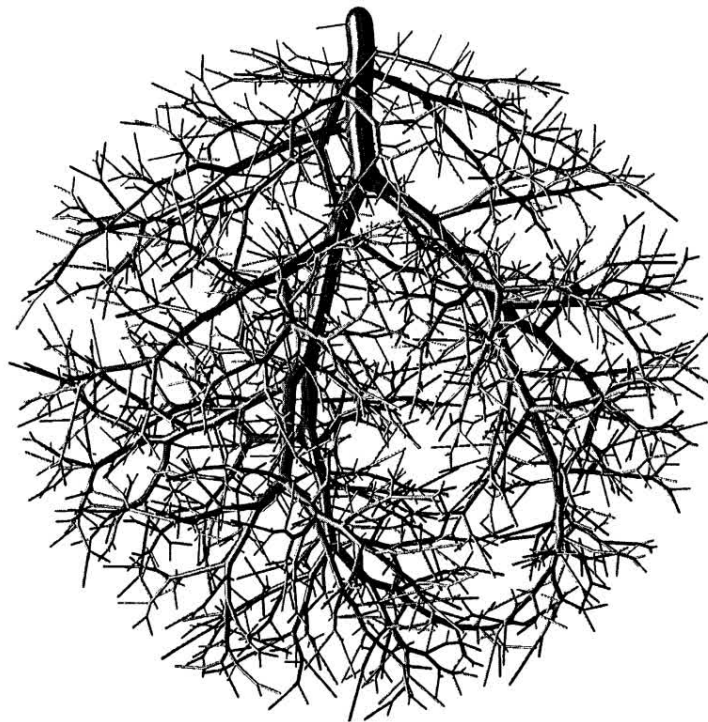
Source: (KARCH et al., 1997).

The CCO method can be used to create a completely new network of blood vessels starting from an inlet point, or also possibly by expanding a previous existing network delimited by the three-dimensional domain (KARCH et al., 1997). This construction is guided by the optimization of a cost functional of the network at each step of generation

(KARCH et al., 1999) in order to construct the most optimal network, trying to result, at each step, in the best coverage of the domain with the minimal cost possible. This cost functional is most commonly associated with the intravascular volume of blood in the network, where the minimization aims to reduce the blood necessary to vascularize the region of interest, but it can be modified for each desired problem, targeting the total length of segments, the surface area, or other expressions based on alternative criteria (SCHREINER et al., 1995).

In (SCHREINER; BUXBAUM, 1993) and (KARCH et al., 1999), the CCO method is formalized and the definitions and considerations for automatic vascularization are briefly presented below. In the region to be vascularized, called perfusion domain, the algorithm generates a binary tree of vessel segments starting from a root node, a point, or a previous network, from where bifurcations are created, until the desired condition, stage, or number of segments is generated. This filling of the perfusion domain is considered to be quasi-uniform in terms of the random sampling of terminal points. Along the generation, vessel intersection is forbidden, and blood is considered an incompressible fluid. These works consider blood with constant viscosity, but further expansions of the algorithm support variable viscosity for smaller blood vessels during construction (TALOU et al., 2021).

3.2.2 Bifurcation power law

One of the physiological constraints embedded in the algorithm is the relation between the diameters of the children vessels when bifurcating from the parent. The relation between the diameters of the tree obey a power law from (MURRAY, 1926) in the form of

$$r_p^\gamma = r_{c1}^\gamma + r_{c2}^\gamma. \tag{3.1}$$

Equation 3.1 shows the relation between the parent blood vessel radius r_p, and their children radii r_{c1} and r_{c2} after the bifurcation, and the parameter γ is the Murray's power law exponent, being directly related to the values of decay of diameters along each level of bifurcation. Larger values of γ result in bifurcating children with larger radii values, and the opposite happens for smaller values of the parameter. A few special cases should be noted: when $\gamma = 2$, the sectional area is conserved in the bifurcation, however when $\gamma = 3$, the endothelial shear stresses in the vessels are homogeneous, which corresponds to a condition of minimal cost when balancing homogeneous perfusion and amount of blood in the network (MURRAY, 1926). In the cerebral circulation, however, the values of γ vary between 2.7 and 3.6 across different regions of the cortex (CASSOT et al., 2010). After each iteration of the algorithm, the diameters of the tree are updated according to this power law.

3.2.3 The Fåhræus-Lindqvist effect

The human blood is not a Newtonian fluid, that is, its rheology cannot be explained by a linear variation purely between flow velocity and stress. This behavior is due to the fact that the viscosity of human blood is not a constant value, but instead it varies depending on the diameter of the blood vessels it flows, and this is the result of the interaction of red blood cells and the plasma, and how these interactions are triggered as a function of the shear rate experienced by the blood (PRIES et al., 1994). Also, it is important to note that blood exhibits a Newtonian behavior in large and mid-sized vessels, where the scale of red blood cell interactions is much smaller than the characteristic vessel caliber.

The human blood viscosity varies according to a function found in (FÅHRÆUS; LINDQVIST, 1931), and while larger vessels present a value surounding the viscosity of 3.6 cP (centipoise), flow inside vessels with smaller lumen area has its viscosity lowered to values down to 2.6 cP. The phenomena explaining this behavior occurs from the alignment of red blood cells, or erythrocytes, during the flow, and their elongation to better accommodate tighter sections.

In (PRIES et al., 1994), the expression for the in-vivo variable viscosity law $\eta(d)$ as a function of the vessel diameter d given in microns (µm) is:

$$\eta(d) = \left[1 + (\eta_{0.45} - 1)\frac{(1 - H_d)^C - 1}{(1 - 0.45)^C - 1} \cdot \left(\frac{d}{d - 1.1}\right)^2\right] \cdot \left(\frac{d}{d - 1.1}\right)^2, \qquad (3.2)$$

$$\eta_{0.45} = 6\exp\left(-0.085d\right) + 3.2 - 2.44\exp\left(-0.06d^{0.645}\right), \qquad (3.3)$$

where

$$C = (0.8 + \exp\left(-0.075d\right))\left(-1 + \frac{1}{1 + 10^{-11}d^{12}}\right) + \frac{1}{1 + 10^{-11}d^{12}}. \qquad (3.4)$$

In these expressions, H_d is the hematocrit, i.e. the volume fraction of red blood cells in the blood, while the reference hematocrit is 45%, and $\eta_{0.45}$ is the viscosity at the reference hematocrit. These expressions result in a formula for the viscosity of the blood vessel according to vessel diameter, and are used in the algorithm when recalculating the tree diameters, its viscosity, resistance, and pressure drop. Figure 16 shows the variation of the viscosity in relation to the vessel diameter.

The computation of viscosity in compartment models, and in consequence the CCO algorithm, are directly affected by this relation. The CCO algorithm uses this formula with $H_d = 50\%$ as a function of radii to compute the pressure drop and the update of vascular tree properties, as it will be seen in the following sections.

Figure 16 – Fåhræus-Lindqvist effect for variable vessel diameter.
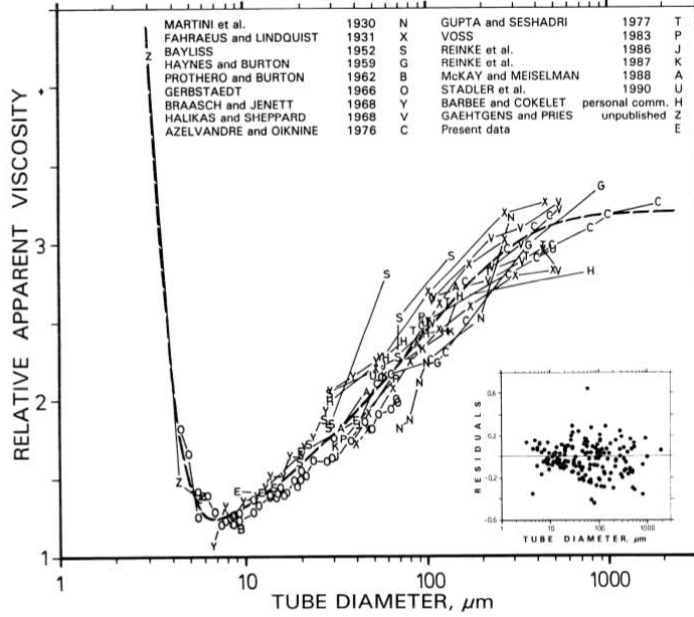
Source: (PRIES; NEUHAUS; GAEHTGENS, 1992). Note: viscosity units are given in cP (centipoise).

3.2.4 Compartmental models

The model underlying the CCO algorithm is a simplified steady-state compartment model in a sense that properties are condensed in a point, and as it will be seen, it is purely resistive during the stage of generation (LINNINGER et al., 2019), while subsequent simulations can add more complexity, such as time-dependence, inertia and vessel compliance. In (KARCH et al., 1997), blood flow is assumed laminar due to low Reynolds number, and we can define a hydrodynamic resistance R due to Poiseuille's law.

Among the physiological principles governing the compartmental models we can cite the conservation of mass, and the conservation of momentum via Poiseuille's law. Equations coupling the boundaries of each compartment are also present. For each vessel, we have a relation for the inlet and outlet flow Q and the pressure drop Δp in the form of

$$Q_{in} = Q_{out}, \tag{3.5}$$

$$\Delta p = p_{in} - p_{out}, \tag{3.6}$$

and the coupling of these properties at the bifurcations from parent p and children $c1$ and $c2$ is

$$Q_p = Q_{c1} + Q_{c2}, \tag{3.7}$$

$$p_{p\,out} = p_{c1\,in} = p_{c2\,in}. \tag{3.8}$$

The resistance R_i of a segment in the tree is calculated individually as

$$R_i = \frac{8\eta(r_i)l_i}{\pi r_i^4}, \tag{3.9}$$

where $\eta(r_i)$ is the radius-dependent viscosity of the blood, and l_i and r_i are the length and radius of segment i. The flow at each terminal Q_k is considered fixed, and calculated from the total flow Q_{total}, being proportional to the cubic radius of each vessel as

$$Q_k = Q_{\text{total}}\frac{r_k^3}{\sum_{j=1}^{N} r_j^3}, \tag{3.10}$$

in which N is the total number of vessels. By fixing the pressure at each terminal equal to the capillary bed pressure (KARCH et al., 1997), this allows the calculation of the blood pressure at each bifurcation of the tree, correlating the blood flow Q_i and pressure variation Δp_i in each segment as

$$\Delta p_i = R_i Q_i. \tag{3.11}$$

As seen in (LINNINGER et al., 2019), the resistance element dominates for low velocity and small vessels. The consequence is that the nature of the blood flow is mainly resistive in smaller vessels, due to the low values of the Reynolds number (Re<1) and Womersley number (Wo<0.1), allowing the authors to ignore the inertial, pulsatility and compliance terms (LINNINGER et al., 2013).

The model becomes largely simplified with purely the resistance terms. The total resistance of the tree can be calculated by associating the individual resistances of the network in series and parallel, analogously to electrical circuits (LINNINGER et al., 2019). Figure 17 present an association of cumulative resistances of a CCO generated tree.

3.2.5 The algorithm

For a vascular domain previously defined where blood perfusion occurs, the iterative algorithm begins the automatic vascularization by appending blood vessels segments to an inlet or an existing network. The CCO algorithm for constructing the blood vessel network from (KARCH et al., 1999) can be seen in algorithm 1.

Hence, a new point is randomly selected, the iterative procedure is repeated, and the algorithm finishes when the number of terminals in the network reaches a pre-defined value. Figure 18 shows the steps in adding the vessels using the algorithm. The result is a vascular network of blood vessels inside the perfusion volume. Previous works have used this algorithm for generation of vascular networks, by filling a domain to model the cerebral arterial network of a rat brain (LINNINGER et al., 2019) and using this sequential and iterative method for adding blood vessels.

Figure 17 – Association of cumulative resistances in a CCO binary tree.
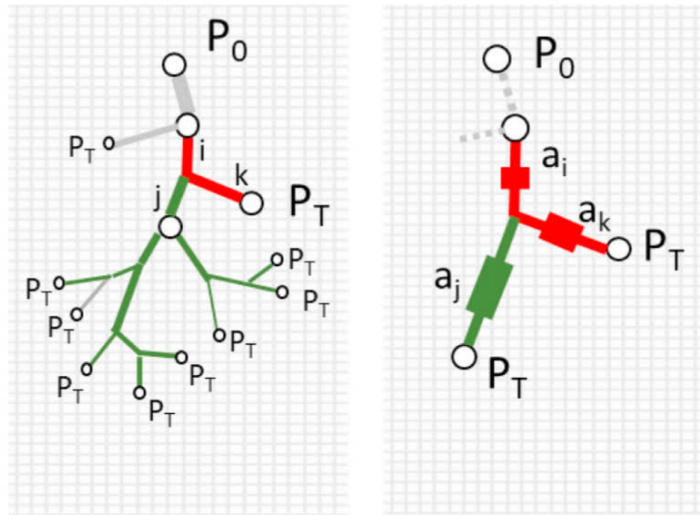
Source: (LINNINGER et al., 2019). Association of resistances follows from terminal upwards.

Figure 18 – Steps for appending of a vessel in the CCO algorithm.
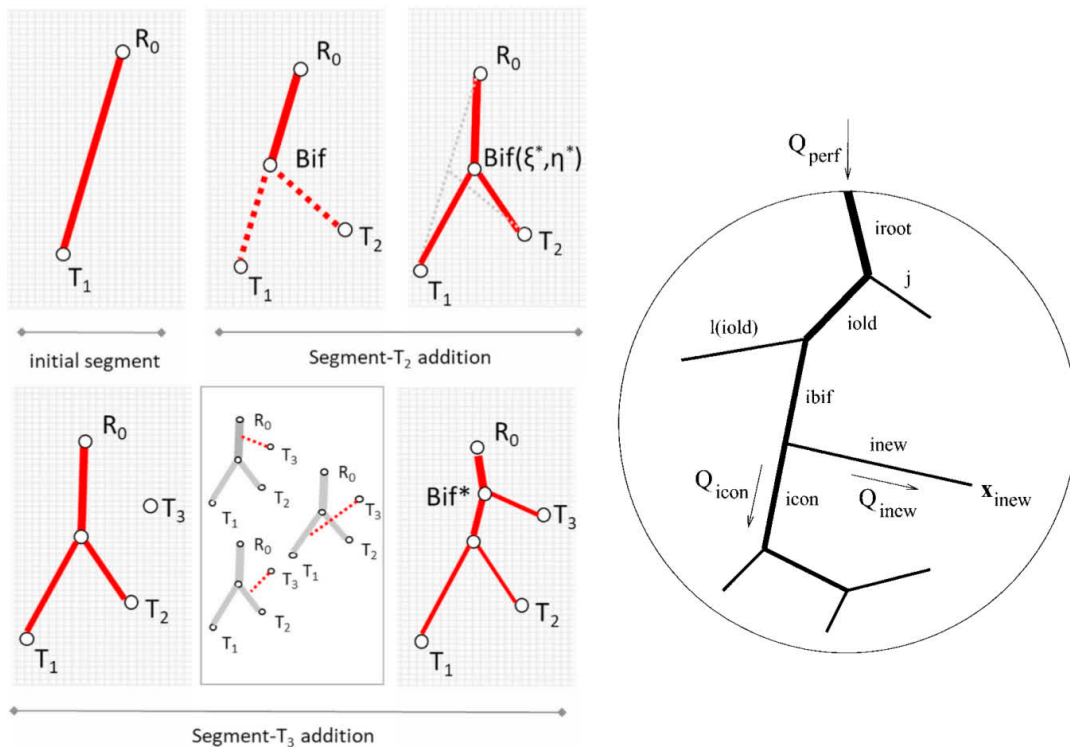
Source: (LINNINGER et al., 2019) (left) (KARCH et al., 1999) (right). Left shows the steps that occur during bifurcation, and selection of best parent vessel candidate, and right shows a tree after a few steps.

Algorithm 1 Constrained Constructive Optimization algorithm (KARCH et al., 1999).

1: **procedure** CCO GENERATION(initial tree, domain, parameters)
2:   **repeat**
3:     sort a point in the domain as a terminal candidate
4:     **if** initial tree does not exist **then**
5:       connect terminal to inlet, create root node
6:     **else**   ▷ *continue generation from previous tree*
7:       find all neighbor vessels to this terminal
8:       filter them as parent vessel candidates
9:       **for** each parent candidate **do**
10:         bifurcate towards the terminal
11:         create a vessel between the parent and the terminal point
12:         **if** geometrical constraints are satisfied **then**
13:           ▷ *parent is suitable candidate*   ◁
14:           connect the new vessel to the tree
15:           update the diameters of the tree according to Murray's law
16:           calculate the total cost of the tree $\mathcal{F}[T]$
17:           calculate the cost of adding the new vessel $\mathcal{J}(v_i)$
18:           remove this vessel and move to next candidate
19:         **else**
20:           parent is not suitable candidate, discard it
21:           **continue** for next parent candidate
22:       choose the parent vessel candidate with the lowest $\mathcal{J}(v_i)$
23:       select it as the best candidate
24:       permanently append the vessel between parent and terminal to the tree
25:       update all tree diameters, pressure, and viscosity levels
26:     **continue** with the next terminal
27:   **until** number of terminals is reached

3.2.6   Minimization of the cost functional

The CCO technique, as mentioned before, aims to minimize a cost functional that is interlaced with the state of the blood vessel tree in order to obtain the most optimal network arrangement. It is generally associated with the total intravascular volume of blood in the perfusion domain, which is a combination of the lengths and radii of the network. Some other functional evaluations include the surface area of the vessels, the total length of the tree, or a combination of these characteristics, enabling the construction of more complex functional evaluations, that considers the sprouting of an initial tree. This functional can be altered and adapted to other criteria when needed.

For one segment of vessel v_j with length l_j and radius r_j, one commonly used expression for the functional cost $\mathcal{J}$ is

$$\mathcal{J}[v_j] = \pi l_j^{\mu} r_j^{\lambda}, \tag{3.12}$$

where parameters μ and λ are commonly 1 and 2 respectively to generate a volumetric cost for the vessel. This supposition is reasonable, since the higher the volume of blood,

the more costly it is to maintain it, and this results in networks that are consistent with real specimens, in a probabilistic sense, as shown in the literature (KARCH et al., 1999). Due to linearity, the total cost of the tree $\mathcal{F}[T]$ is the sum of all the costs of the N vessels in the tree

$$\mathcal{F}[T] = \sum_{j=1}^{N} \mathcal{J}[v_j],\tag{3.13}$$

and the volumetric functional $\mathcal{F}$ for a tree T is given by

$$\mathcal{F}[T] = \sum_{j=1}^{N} \pi l_j r_j^2.\tag{3.14}$$

This can be extended into a more generic functional $\mathcal{J}$ for the sprouting behavior of the vascular network to include the proteolytic and diffusive costs of the tree. These costs are respectively the cost associated from sprouting from a parent with larger diameter, and the cost associated with the length of the newly generated vessel, and represent the cost associated with angiogenesis (TALOU et al., 2021). For that, the sprouting cost $\mathcal{J}$ for adding a new single vessel v_i is

$$\mathcal{J}(v_i) = c_v \left\{ \mathcal{F}[T](v_i) \right\} + c_p \left[r_p(v_i) \right] + c_d \left[l_i(v_i) \right]^2.\tag{3.15}$$

In this expression, $l_i(v_i)$ is the candidate vessel's length and $r_p(v_i)$ is the parent vessel's radius, and the coefficients c_v, c_p and c_d characterize the predominance of the volumetric, proteolytic and diffusive cost mechanisms in the network (TALOU et al., 2021). This last expression, together with the volumetric cost, were the two cost functionals adopted for this work.

3.2.7 Current limitations of the conventional CCO technique

The CCO algorithm has a few limitations in its most basic form, which can be circumvented by the implementation of alternative versions to the method. Some of the past implementations of the CCO have fixed many of the parameters during the generation of the network, locking the optimization procedure in an implementation with a predefined configuration that could not be adapted to different domains or stages of generation. The required flexibility for the construction of anatomically-correct networks has been discussed in previous works, and one implementation proposes the use of adaptive features to the optimization procedure (TALOU et al., 2021) that permit the changes of parameters for different stages in the network, or even different functionals for separate stages. For example, while initial stages of the network may require one set of parameters for generation, subsequent stages with smaller vessel diameters follow a different parameter configuration.

Another fundamental limitation is related to the high computational cost of the algorithm. The conventional CCO implementation follows a sequential generation of the

vascular tree, and the cost increases substantially when the number of vessels in the tree is large. In fact, as the network increases, the time required for calculating the possible minima of the functional increases quickly. Although difficult to circumvent in the conventional CCO due to the sequential nature of the algorithm where the most recent vessel alters the functional cost calculated for the next vessels, this obstacle has been discussed in previous works while designing a way of distributing the load of execution among separate calculations (CURY et al., 2021).

Another current limitation of the CCO lies in the nature of the binary tree generation, where closed loops and collateral vessels, not uncommon in the cardiovascular system, are not considered in the CCO binary tree generation. In fact, these graph-like structures cannot be modeled solely by a parent-children structure. The modeling of deep cerebral perfusion involves an elevated number of capillaries inter-connected following a graph-like topology, and the approach to model them requires specific coupling between the tissue and the vessels. Therefore, different algorithms are required to the correct vessel-tissue coupling, as discussed in previous works in chapter 1.

In the next sections, we review modifications of the algorithm which have been proposed to fill some of these gaps in the generation, enable multistage generation, and implement the partitioned strategies, where independent generation happens in separate partitions that are then merged into a final network.

3.3   The Adaptive CCO implementation (DCCO)

The aDaptive CCO method (DCCO) (TALOU et al., 2021) is a modification to the original CCO method that has been proposed to better manipulate the variations of parameters along different stages of generation, allowing to generate networks that present higher degree of complexity and heterogeneity along the branching levels, and tackle complex vascularization tasks. The generation can be broken into stages with different optimization parameters according to each territory as needed, called the vascular domains.

These constraints, when modified along stages and regions, can better mimic real vascular structures, and improve the consistency with the human anatomy, as observed in the literature. For instance, a first stage with larger vessels has one set of parameters, and the smaller additional stages have a different set of parameters adapted to smaller vessel scale. A few constraints used in the DCCO algorithm are the Murray's exponent γ, the symmetry ratio parameter δ between post-bifurcation vessels which limits the bifurcation radii of children vessels r_{c1} and r_{c2} as

$$\frac{\min\{r_{c1}, r_{c2}\}}{\max\{r_{c1}, r_{c2}\}} > \delta, \tag{3.16}$$

and the aspect ratio of each segment

$$\frac{l_i}{r_i} > 2, \tag{3.17}$$

which is considered to be at least 2 (TALOU et al., 2021). Also, the angle of bifurcation defined by the direction of bifurcating segments can be constrained.

Aditionally, the DCCO algorithm makes use of the compartmental steady-state flow model, therefore purely resistive model, with variable viscosity for blood, where each vessel is considered a straight rigid cylinder.

The cost functional can also be changed to accommodate the necessities in the creation of the network. For instance, it is possible to minimize any combination of the length and radius, notably the volume with exponents 1 and 2 respectively, differently for each stage of generation. In addition to this, more complex functional expressions for the cost of the tree can be formulated in this method, such as the sprouting functional used in this work. Each functional can be applied for its corresponding stage in generation, can be switched between large and small blood vessels.

In summary, the algorithm adds vessels sequentially to the tree, which is remodeled after every step (TALOU et al., 2021). One difference from other algorithms is that the root radius of the tree and the domain to be vascularized are fixed.

The DCCO implementation makes use of a characteristic length named l_{min} to ensure that terminal points have the minimal distance l_{min} from other terminal points by

$$l_{min} = l_c \sqrt[3]{\frac{\nu}{NT + 1}} \tag{3.18}$$

where l_c is the radius of the sphere with the 3D domain's volume, ν is a factor to adjust for slender domains, and NT is the current number of terminals. This l_{min} length is reduced by a factor f_r if enough unsuccessful attempts to find a valid parent vessel have been performed.

When connecting to the parent vessel, the algorithm adjusts the bifurcation point in a triangular mesh with edge containing Δv vertices (TALOU et al., 2021) to find the most optimal point of connection. Vessel radii and viscosities are iteratively updated when testing for the optimal segment, and the CCO algorithm continues with these considerations.

The DCCO implementation also allows to generate vessels whose bifurcating condition depends on their position in the domain, i.e. if they are completely or partially inside the geometry, being:

    a) distribution vessels, which only bifurcate when completely inside the domain;

    b) perforator vessels, which bifurcate from points inside the domain;

c) transport vessels, which can bifurcate regardless of their location.

Vessels also have their limitation on how to bifurcate, i.e., how they will adapt when creating the bifurcation point. They can be set as:

a) non-bifurcating vessels;

b) rigid parent, that do not deform when bifurcating;

c) deformable vessels, being flexible when bifurcating;

d) distal branching mode, appending new vessels at the endpoint of the parent vessel.

Regarding staged growth, the concept lies around sequential vascularization stages with stage-specific configurations such that they render a certain architecture. In other words, each stage runs an independent CCO algorithm with its own set of parameters, and changing into a new stage is triggered when a number of terminals is present in the tree, allowing to mimic complex vascular structures. A list of the important parameters for each stage $\mathcal{S}$ of the DCCO implementation (TALOU et al., 2021) are

a) the domain Ω, or the perfusion domain, which can be considered simple or a boolean composition;

b) the geometrical parameters $\mathcal{P}_{geo}$, including

– the Murray's power law exponent γ;

– the symmetry coefficient ratio δ, which relates to the ratio between diameters of segments in a bifurcation;

c) the optimization parameters $\mathcal{P}_{opt}$, including

– the perfusion area factor ν, which affects the characteristic length when searching for nearby candidate parent vessels, to ensure uniform generation in slender domains;

– the characteristic length reduction factor f_r after n unsuccessful attempts, which reduces the characteristic length to connect to closer segments;

– the neighborhood factor f_n, i.e. a factor that multiplies the characteristic length as a radius to search for nearby candidates of parent vessels;

– the number of possible bifurcating spots per segment Δv when searching for the optimal connection in a parent vessel;

d) the initial tree $\mathcal{T}_{init}$ passed to the algorithm from outside or from a previous stage;

e) the number of terminals NT_{final} desired for the generation in a certain stage;

f) the cost functional $\mathcal{F}$ which can be volumetric, sprouting-like, or a combination;

g) the vessel type, being distribution, perforator, or transport;

  h) the bifurcating angle constraints.

3.4 The Parallelized DCCO (PDCCO)

An additional modification to the CCO routine is the Parallelized DCCO version (PDCCO) (CURY et al., 2021). This expansion of the existing algorithm enables the construction of massive networks of blood vessels with an unprecedented level of detail, making it viable the construction of networks with the quantity of segments in the order of hundreds of thousands in a feasible time. The accomplishment of this endeavor is performed via the division of the domain to be vascularized into smaller disjoint subdomains, where independent vascularization processes take place appending to an existing base network. In other words, this partitioned decomposition strategy is used to concurrently expand a given base vascular network.

  This divide and conquer strategy in PDCCO (CURY et al., 2021) is used to decompose the domain using the following procedure:

  a) start with a base tree $\mathcal{T}$ generated previously with DCCO in the full domain Ω;

  b) define a partition into subdomains Ω_i, $i = 1, \ldots, N$, N the number of subdomains, of the domain Ω, or a subset of it, where independent vascularization processes are going to be performed.

  c) for each disjoint partition Ω_i of the domain, expand the base tree by generating terminal points in Ω_i from vessels inside this partition, thus creating $\mathcal{T}_i$; only terminals inside Ω_i have their flow updated;

  d) the coordinates of the new vessels and their parent vessels are saved in a list $\mathcal{L}_i$;

  e) the vessels of each list $\mathcal{L}_i$ are sequentially added to the base tree $\mathcal{T}$;

  f) when the vessels for all partitions are added, the diameters are updated normally using hemodynamic and geometric constraints.

  This parallelized generation can be easily distributed into several threads in order to accelerate the generation of the vascular network. After the generation, all independently generated networks are combined into a single final massive network according to the procedure described in (CURY et al., 2021). While the generation happens independently, the final result is close to a sequentially-generated tree, and thus the resulting network presents itself as a valid model of a vascular generation in a determined organ. The time consumed, however, is significantly shorter compared to the original sequential alternative, removing another limitation originated from the sequential counterpart of the algorithm. Results in (CURY et al., 2021) show that for 100 000 terminal vascular segments, the sequential estimated time is around 2230 hours, while the PDCCO method takes 3.27 hours for a base tree with 5000 terminals and an average of 3 hours per partition when

using 25 sub-domains to perform the partitioned vascularization. As mentioned in (CURY et al., 2021), the DCCO/PDCCO algorithm has a complexity in the order of $O(n^3)$.

3.5 The VItA library

The implementation of the CCO used in this work is a continuation of the DCCO and PDCCO versions of the algorithm (TALOU et al., 2021; CURY et al., 2021), that were developed in the HeMoLab/LNCC group, and were published as a library named VItA, which can be downloaded from `https://github.com/GonzaloMaso/VItA`. The VItA library, written in C++, contains the extensions from the adaptive version described in (TALOU et al., 2021), and the parallelization proposed in (CURY et al., 2021), permitting to build CCO networks with high complexity and variety according to the desired use case and domain.

This work also contributed to the VItA library, through the following improvements

a) the creation of a class to generate the penetrating vessels in the cortical domain, and another class to append vascular subtrees at distal points of the penetrating segments, providing the necessary tools to generate the network desired in this work, including the manipulation of segments and subtrees for the work here presented was also implemented;

b) a method to manually update the vessel segment diameters in the subtree after the appending, according to the power law exponent.

c) propose a new constructor for the stage generator allowing the modification of a per-stage Branching Mode setup;

d) complement the aspect ratio of vessels with a new length-ratio to avoid bifurcations when one of the resulting segments is less than 10% of the original length;

e) updated the overlapping criterion for added vessels in the optimization, by checking the distance to the vessel;

f) evaluate the criterion for transport vessels when checking for parent vessel candidates;

g) enable filtering for terminal vessels;

h) fix smaller bugs in the point sampling, and in the generation of the plane angle conditions for rigid parent vessels.

4 Methodology: input data and model setup

This chapter presents the workflow elements, key choices, and model setup for the development of this work, which includes the input data used for the generation of vascular networks in the brain. In summary, this involves the preparation of the geometrical model of the cerebral cortex and the existing vascular model as a starting point for generation. The details of the methodology are presented in the following sections.

4.1 Geometry of the human cerebral cortex

The geometry of interest consists of the cortical region of the human brain, delimited by two surfaces: the pial surface and the surface between grey matter and white matter. This geometry, which was acquired via MRI scans, was provided as 3D STL image files for this work. The STL for the pial surface, and for the boundary between the gray and white matter, were provided for both hemispheres, that is, the inner and outer boundaries of the gray matter. This geometry can be seen in figure 19.

In this work, we chose the left hemisphere as a proof-of-concept example, noting that the same procedures can be applied to the right hemisphere to obtain a vascular network of the entire brain. The present work obeys the ethics and committee guidelines, according to the following statement: all data collection and analyses used in the manuscript were conducted in accordance with the ethics approval from the New Zealand Health and Disability Ethics Committees (HDEC approval number 20/CEN/107). All participants involved provided written informed consent prior to study participation.

4.1.1 Processing and preparation of the cortical cerebral geometry

The geometrical domain was prepared in the Blender 3D modeling software (`https://www.blender.org/`) for the correct delimitation of the perfusion domain used in the generation of the vascular networks. The following geometrical domains are important for the generation of the network:

a) the pial space, where generation in the first stages occurs;

b) the delimitation of each vascular territory for each of the three main cerebral arteries (ACA, MCA, and PCA);

c) the partitions used in the parallelized generation when generating the massive pial network;

d) the gray matter space, where arterioles penetrate the brain tissue.

Figure 19 – 3D geometric image of the brain obtained from MRI.
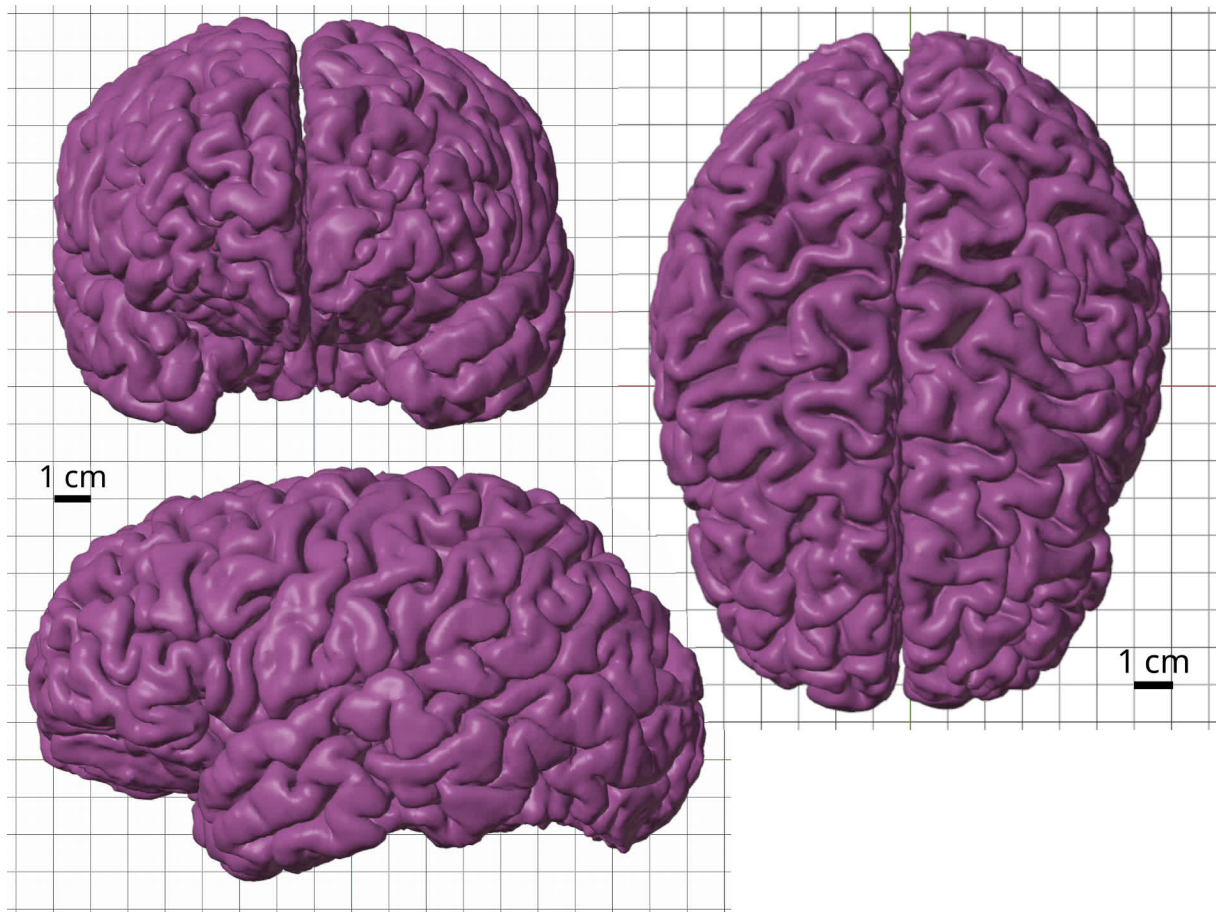
Top left: coronal view; right: transverse view; bottom left: sagittal view. One square in the image is 1 cm.

These domains for the left hemisphere are imported in Blender, the original geometry is given in mm, so it is converted from mm into cm using a 0.1 scale factor.

4.1.2   Definition of the pial space

The volume considered for the pial space was obtained from the outer layer of the gray matter (i.e. the pial surface), which is imported into Blender for the 3D manipulation. In order to define a volume where the DCCO (and posteriorly the PDCCO) algorithm will vascularize, the pial surface is extruded with a thickness of 0.2 cm using the *solidify* filter, with 75% of extrusion occurring outwards, and 25% inwards. The inner and outer layers of the domain are separated with *separate by loose parts* function in edit mode, and the *remesh* filter is applied to each of the resulting solid volumes to remove any geometrical inconsistencies such as overlapping faces, with voxel size 0.05 cm and adaptivity 0.1. Surfaces have their normal orientation set outwards from each domain before being merged

into a single volume. Figure 20 illustrates the domains used in this work, along with their delimitation.

Figure 20 – Layers of the cerebral regions used for generation and projection.
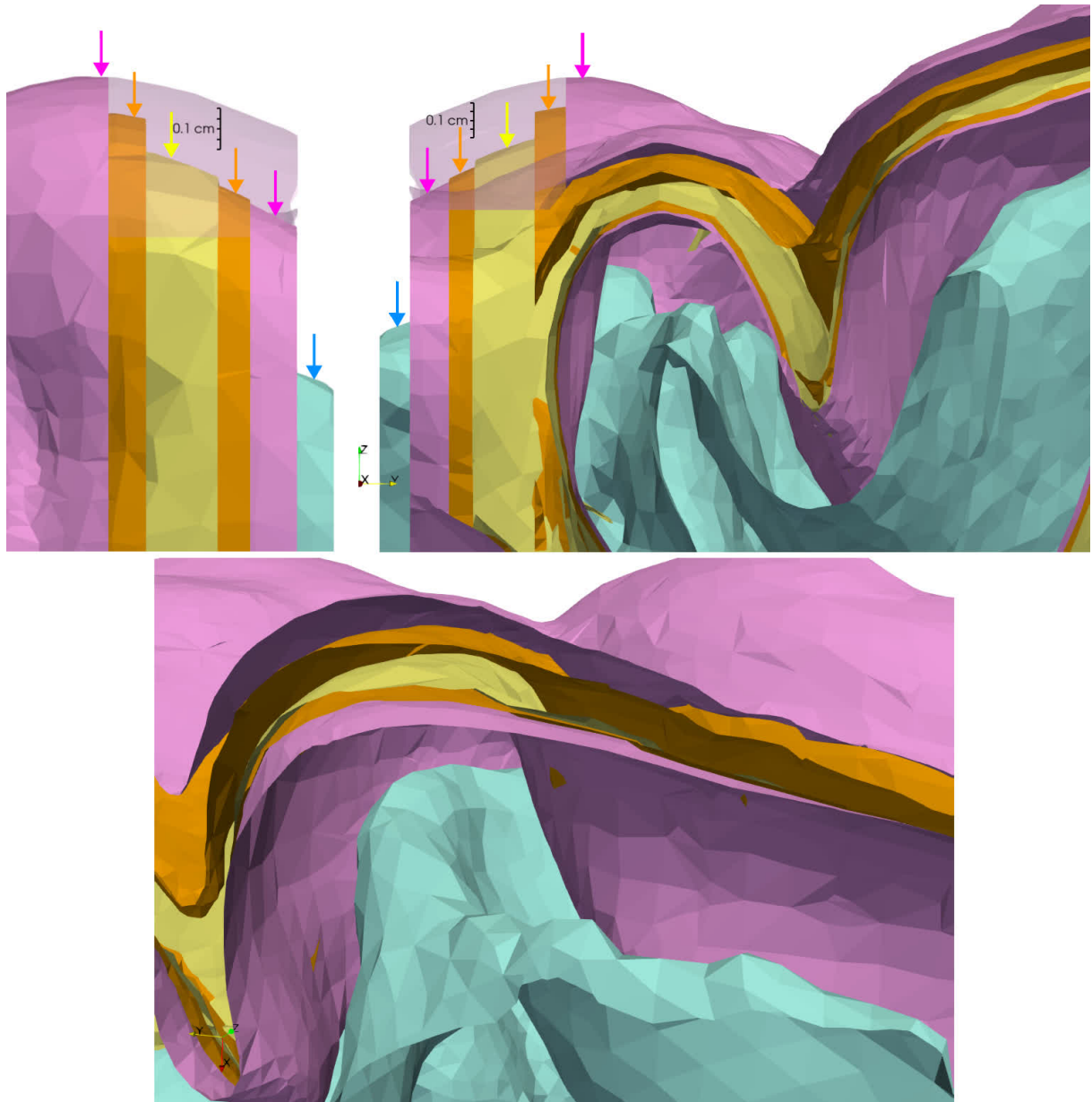
Top left: sagittal view from inside, ACA parietal region, orthogonal view. Top left, saggital slice from outside of the same region. Bottom: transverse view shown from below, same region. The original pial surface is shown in yellow. The pial space is shown in magenta for outer and inner boundaries. Projection surfaces are shown in orange. The interface between gray and white matter is in cyan.

This single-volume domain is what we call the pial space (or also pial domain), and is the domain where pial vessels are to be generated. The resulting total volume of the pial domain is 170.2 cm³. This spatial domain is ready to be used to generate the pial

vascular network. However, before that it is necessary to separate the domain into three territories representing the areas vascularized by the major cerebral vessels.

An additional surface, called projection surface, for the projection and registration of the initial vasculature from the ADAN model (BLANCO et al., 2015) was also prepared. The *solidify* filter is applied again to the original pial surface, but with 0.1 cm of thickness, 75% outwards and 25% inwards, to obtain a surface in the middle between the gray matter surface and the outward boundary of the pial domain. The *remesh* filter is applied with the same parameters (voxel size 0.05 cm, adaptivity 0.1) to remove inconsistencies. This surface is used for the baseline model registration and projection, which is presented later in this chapter.

4.1.3 Definition of the major vascular territories

As stated in chapter 2, the blood perfusion of the cerebral cortex is delivered by the three main cerebral arteries, the Anterior (ACA), Middle (MCA) and Posterior Cerebral Arteries (PCA). In order to be consistent with the knowledge available in the specialized literature, the brain was subdivided into three territories, one for each main artery. These three territories were obtained by sculpting regions in Blender according to (SCHÜNKE; SCHULTE; SCHUMACHER, 2010). Through boolean operations, we defined the major cerebral territories where each one of the major cerebral vessels will vascularize. The boolean operations are illustrated in figure 21.

The three regions of the brain are presented in figure 22. A small intersection region between the territories was maintained to guarantee redundancy in the blood flow supply, and to avoid occlusion spots in the boundaries of each vascular territory. Moreover, these overlapped regions provide a natural spot for the introduction of inter-territorial collateral connections in future versions of this model.

Following the definition of the vascular territories, the volumes for each region can be fully characterized, and are presented in table 1, along with the total volume and overlapping volumes at territory intersections. The number of partitions for later generation is also presented, and will be discussed in the next subsection. The overlapping of the regions results in a total effective volume of 195 cm³. Out of this volume, 14% are due to the overlapping.

Table 1 – Volume and surface area for each major vascular territory of the cortex.

Parameter	ACA	MCA	PCA	Sum	Cortex
Volume [cm³]	63.6	86.2	46.8	195.0	170.2
Surface Area [cm²]	315	430	230	975	850
Number of partitions	7	8	6	21	—

The volume of each domain was calculated in Blender, and the total surface area

Figure 21 – Illustration of boolean operations applied over the brain geometry.
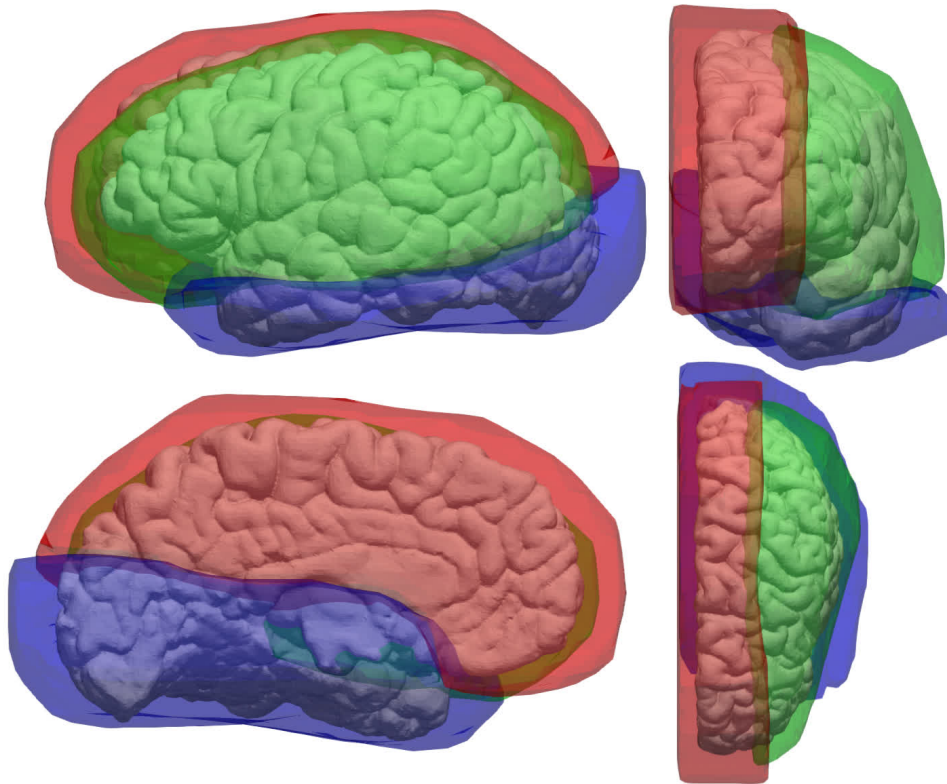
Region colors of the boolean operations are red for ACA, green for MCA, and blue for PCA. Top left: sagittal view from outside; top right: coronal view; bottom left: sagittal view from inside; bottom right: transverse view.

for each region was calculated considering the uniform thickness of the surface being 0.2 cm, uniformly distributed along the surface. This gives a factor of 5 in order to obtain the surface area of each partition based on the volume of each territory. The areas of each domain are presented in table 1 as well.

4.1.4 Domain decomposition for parallel vascularization

Considering a baseline pial network, the following stage is performed in parallel, and for that, the domain was partitioned into separate regions where parallelized generation occurs according to the PDCCO version of the algorithm (CURY et al., 2021). For that, each partition was created in Blender as a set of adjacent, disjoint hexahedral volumes delimiting the region for each sub-territory. The merging of the networks will be carried afterwards according to (CURY et al., 2021). Figure 23 presents the division of the territories into the subdomains.

As presented in table 1, the ACA territory was subdivided into 7 partitions, the MCA territory into 8, and PCA into 6 partitions. The volume of each partition is presented

Figure 22 – Division of the three territories of the brain geometry.

Region colors are red for ACA, green for MCA, and blue for PCA. Top left: frontal coronal view; top center: sagittal view from outside; top right: transverse view from above; bottom left: rear coronal view; bottom center: sagittal view from inside; bottom right: transverse view from below.

in table 2. This information is important to calculate the number of terminals generated in each partition as will be discussed in chapter 5.

Table 2 – Volumes for each partition in the three main cerebral territories.

Partition	ACA [cm³]	MCA [cm³]	PCA [cm³]
1	7.71	7.96	7.84
2	5.86	10.86	8.12
3	10.73	12.61	6.27
4	8.54	10.28	7.40
5	9.24	9.01	12.15
6	10.23	16.57	4.97
7	11.29	11.22	—
8	—	7.68	—

Figure 23 – Partition of the pial domain for each vascular territory.
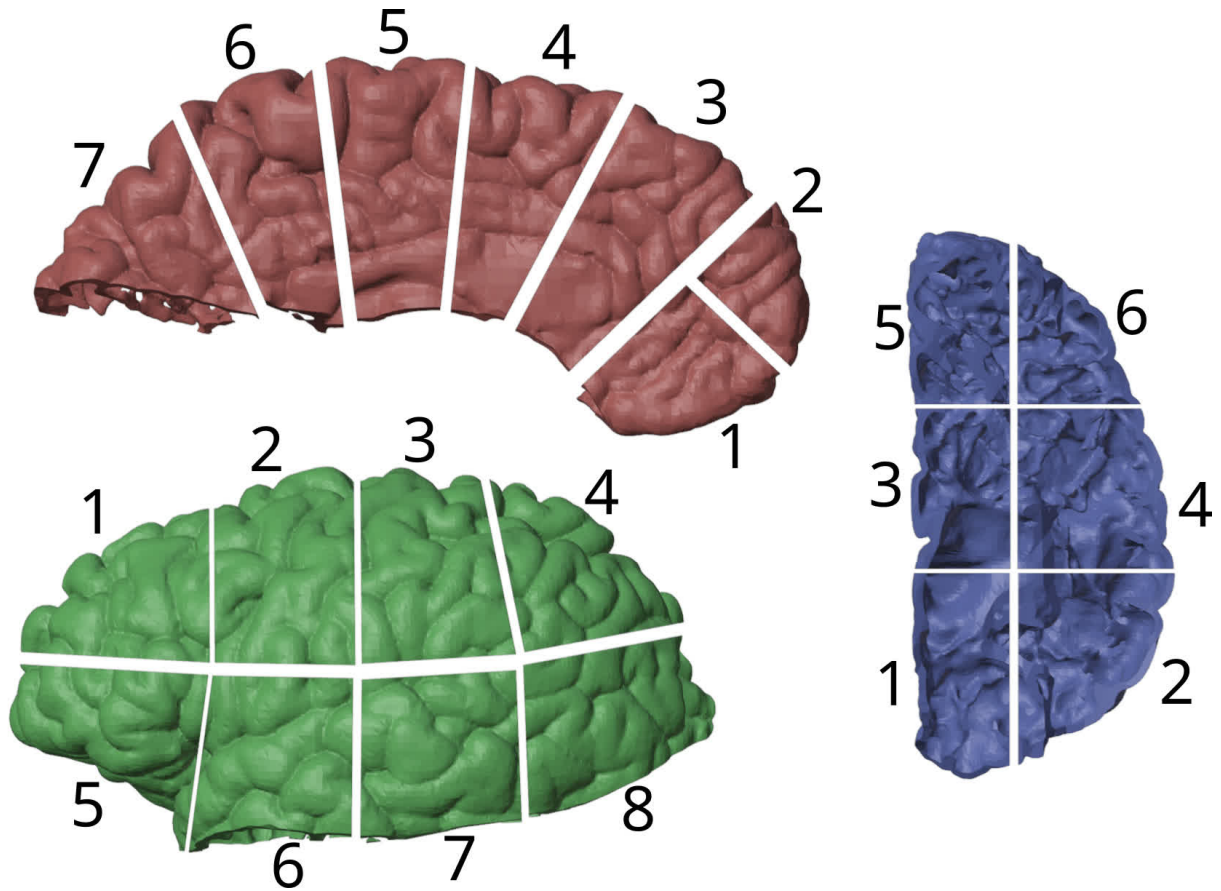
Partitions for each region. Top left: ACA territory (red), sagittal view from inside. Bottom left: MCA territory (green), sagittal view from outside. Right: PCA territory (blue), transverse view from above.

4.1.5 Gray matter space

The perfusion domain for the gray matter was defined between the pial surface and the surface between the gray and white tissues. These two surfaces are obtained directly from the provided STL files.

The steps for data processing are similar, both surfaces are imported into Blender, a *remesh* filter is applied to smooth irregularities with parameters *voxel size* 0.05 cm and *adaptivity* 0.1. Orientation of the surfaces is set outwards from the perfusion domain, and the surfaces are merged into a solid via a *boolean* operator, and another *remesh* is applied to improve the regularity of the domain. Artifacts of the boolean operation, caused by geometrical imprecision of the imaging technique, were removed using the function *separate by loose parts.* Figure 24 shows the layers of the gray matter space. Figure 25 shows both the pial and gray matter spaces overlaid together. Figure 26 shows the surfaces that delimit the gray matter space.

Figure 24 – Layers of the pial and gray matter spaces.
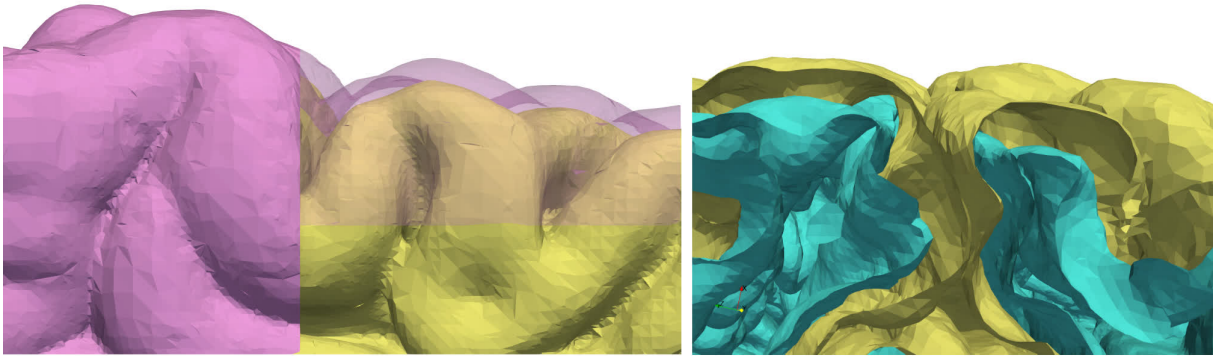
Left: ACA parietal region, sagittal view from inside; right: ACA parietal region, transverse slice from below. Pial domain is shown in magenta, pial surface is shown in yellow, gray-white matter interface is shown in cyan.

Initially, projecting the pial network over the gray matter was considered, however, this idea was discarded due to distortions introduced in the tree. A new methodology for generation in the gray matter is proposed later in this section.

The total volume of the gray matter region, considered as a single domain for this case, is 288.32 cm³, and the outside surface area is 884.87 cm², obtained from half the total area (inside + outside). The gray matter domain was not separated into three territories, but the corresponding volumes for each territory are 94.9 cm³ (ACA), 165.6 cm³ (MCA), and 76.9 cm³ (PCA).

4.2 Initial vascular network

The cerebral arteries of the ADAN model (BLANCO et al., 2015) that run over the cortical region were used as the initial vascular network for the construction of the pial vascular network. To maintain anatomical consistency between the brain geometry (pial surface) and the initial vascular network, the later needs to be adjusted and registered on top of the former. The arteries from the ADAN model that supply the brain with blood are presented in figure 27.

Visualization and model manipulation were performed in Visualization Toolkit (VTK) (`https://vtk.org/`) and ParaView (`https://www.paraview.org/`), as explained in the following sections. The ADAN vascular network is described in the Visualization Toolkit format (VTK). This is a common format used in the calculations and results of computational simulations, and is widely used by the VItA library presented in chapter 3. VTK file formats can be visualized with the Paraview software.

Figure 25 – Overlay of the pial domain and the gray matter domain.

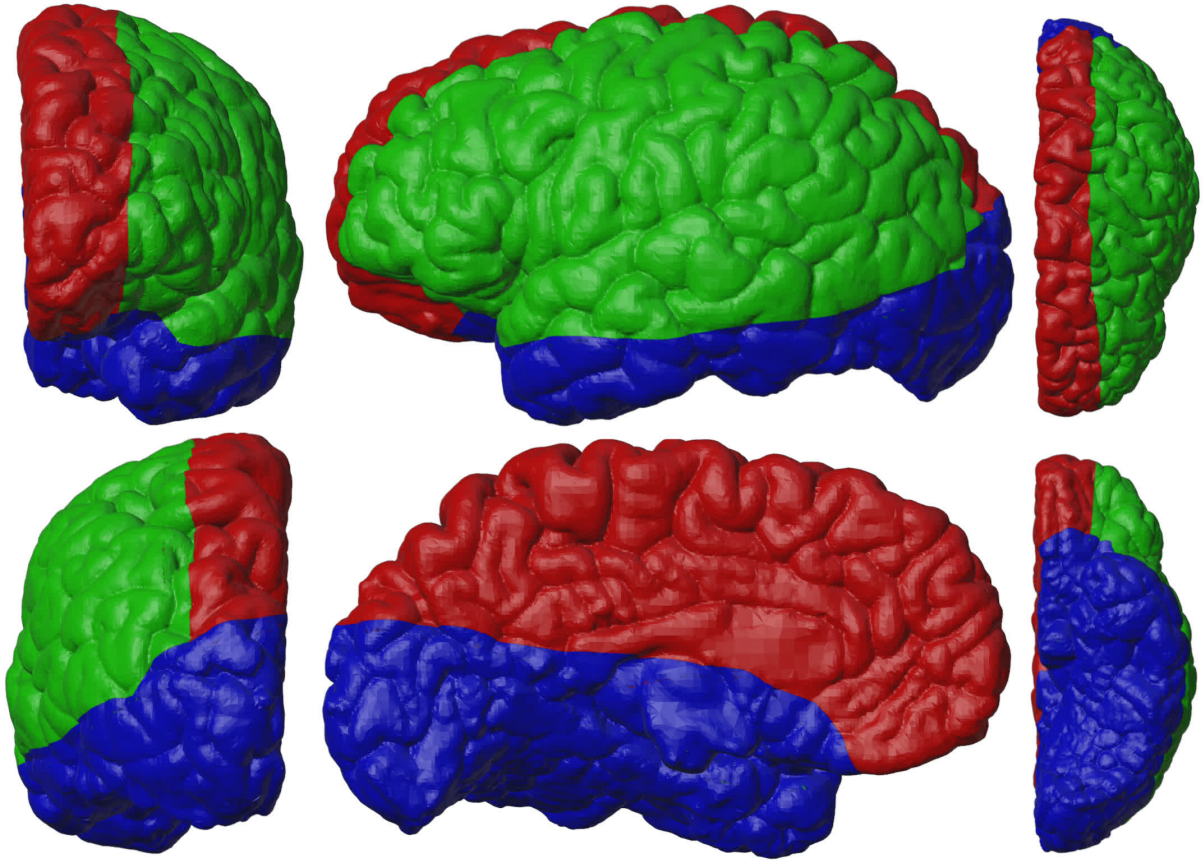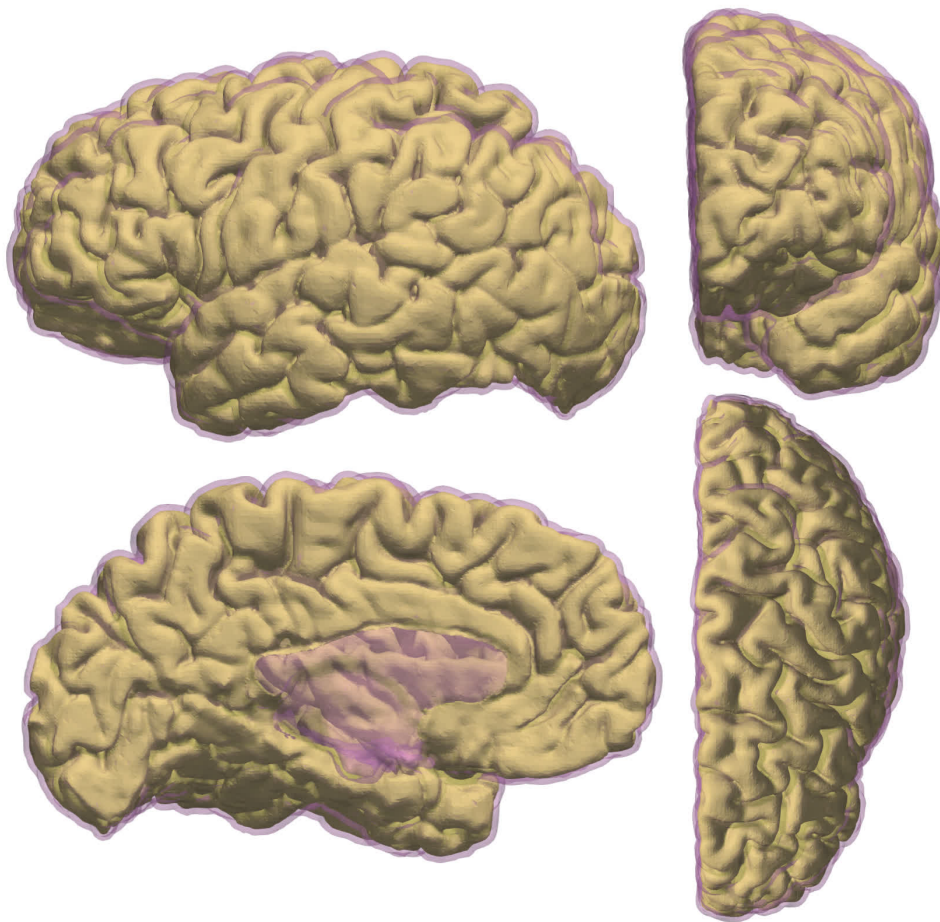Top left: sagittal view from outside; top right: coronal view; bottom left: coronal view from inside; bottom right: transverse view. The outer boundary of the pial domain is shown in magenta translucent tint. Gray matter space is located below the pial surface, which is shown in yellow. Notice the lack of gray matter in the corpus callosum in the sagittal view from inside.

4.2.1   Processing and preparation of the ADAN vascular model

The cerebral network of the ADAN model was adjusted for the generation of the pial network. The vessels from the ADAN mesh were de-refined and their number of points was reduced to improve mesh uniformity, and facilitate the subsequent vascularization stage. The script works by splitting and segmenting again the vessels into new VTK poly-lines, where each segment has 1 cm length composed of three points. Segments smaller than this length are not altered. This de-refined model continues to the registration and projection onto the pial surface as explained in the following subsections.

Figure 26 – Pial surface and gray/white matter surface.
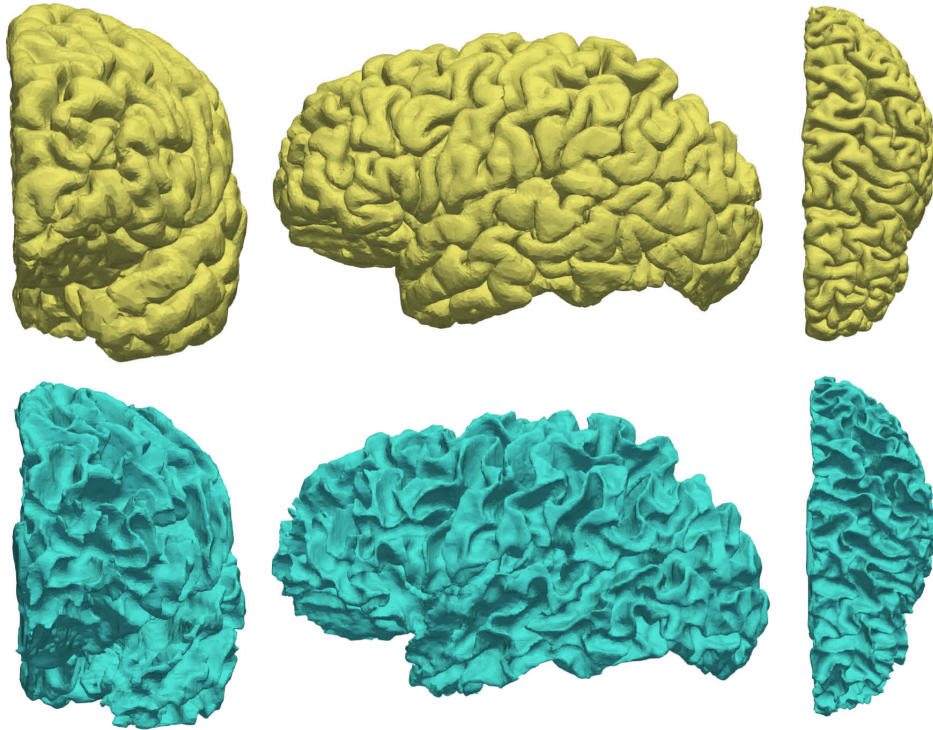
Top row: pial surface in yellow, coronal, sagittal and transverse views respectively. Bottom row: interface between gray and white matter in cyan, coronal, sagittal, and transverse views respectively.

Figure 27 – Three dimensional cerebral vascular model used as baseline for the registration of both hemispheres, starting from the circle of Willis.
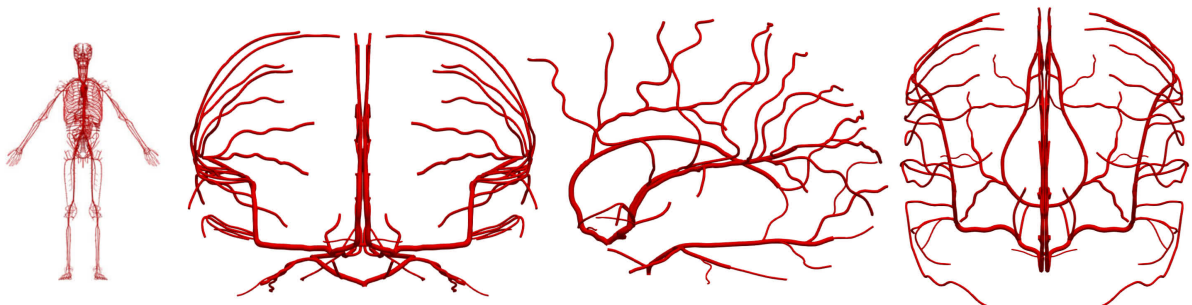
Left: full adan vascular network (BLANCO et al., 2015); second column: coronal view for both hemispheres; third column: sagittal view for both hemispheres; right: transverse view from both hemispheres.

4.2.2 Extraction of the ADAN model to a CCO-ready ASCII file format

The VTK model of the ADAN network was imported into Paraview 5.11, and an in-house plugin was used to convert the structure into a text file containing the baseline vascular network. This file contains the geometry points, the diameters for each vessel, and the connectivity matrix.

The left and right hemispheres of the model were extracted and separated from the ADAN model, and for each hemisphere, the three major arteries that derive from the circle of Willis and their bifurcations are separated, namely:

a) the Anterior Cerebral Artery (ACA), starting after the Anterior Communicating Central Artery;

b) the Middle Cerebral Artery (MCA), starting from the Middle Cerebral Artery;

c) the Posterior Cerebral Artery (PCA), starting from the Posterior Cerebral Post-Communicating Artery branch.

Figure 28 shows these initial networks branching from the circle of Willis for the left hemisphere.

Figure 28 – Cerebral arteries used as initial networks for the generation one one hemisphere, starting from the circle of Willis.
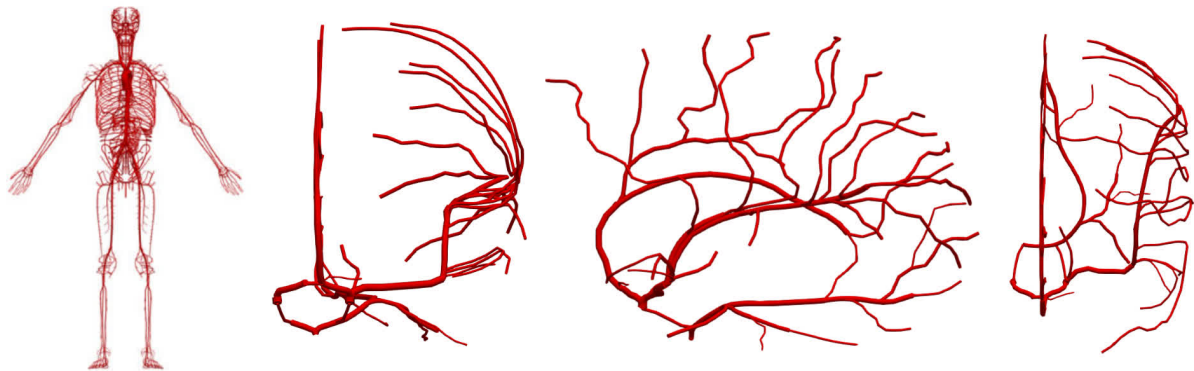
Left: full adan vascular network (BLANCO et al., 2015); second column: coronal view; third column: sagittal view; right: transverse view.

For the preparation of this baseline network, a few considerations were made. Due to the binary tree limitation of the CCO algorithm, arterial loops in the vascular model were trimmed into separate parts, and vascularized separately. So, the Medial Occipital Dorsal to Corpus Callosum artery was cut in half, and included in both the ACA and PCA territories, with the segment in the PCA region correctly reoriented for the algorithm by swapping the proximal and distal points for each vessel. The Circle of Willis (CoW) and the carotid arteries, initially thought as starting points, were not considered in the

vascularization, and the initial segments used for generation in each territory were derived from the three main cerebral arteries that bifurcate from the CoW. This overcomes the limitations of CCO and simplifies the generation.

The three vascular networks for each territory are exported in Paraview to an ASCII-based internal format used in HeMoLab/LNCC, which can be viewed in details in (TALOU et al., 2021) and (CURY et al., 2021). This results in the initial vascular network for each region.

4.2.3 Registration of the ADAN vascular model

The ADAN model was registered to a vascular description of the larger cerebral arteries of the brain, that consists of the vessel centerlines extracted from the MRI scan, and later to the pial surface of the brain. Registration of the ADAN model is performed in two steps:

a) the first step is a linear mapping comprising translation, rotation, and resizing to the correct position according to the vessel centerlines obtained from MRI, by transforming the coordinates of the network;

b) the second step is a projection of the coordinates of the vascular model onto a surface extracted 0.1 cm from the pial surface, to position the vessels inside the pial space.

For the first step, the centroid for the Circle of Willis for both descriptions, ADAN vessels, and MRI vessels, was calculated, as well as the three-dimensional orientation of the vessels obtained from the normal of the plane that best adjust to the points via least squares method. With both centroids moved to the origin, rotation of the ADAN vessels towards MRI vessels is achieved via Rodrigues' formula (LIANG, 2018), and resizing is done via a scale factor based on the variance of the distance of all the points from the centroid.

The registration results in three parameters:

a) a translation vector between the centroids;

b) a rotation matrix from the ADAN model towards the MRI vessels;

c) a scale factor applied to each direction independently.

The resulting parameters for the registering in this case are presented in table 3. The rotation matrix is

$$R_{\mathrm{Rot}} = \begin{bmatrix} 0.997 & 0.047 & 0.056 \\ -0.031 & 0.965 & -0.271 \\ -0.067 & 0.258 & 0.964 \end{bmatrix}. \tag{4.1}$$

Table 3 – Translation and scale factors for each coordinate between the ADAN model and the brain arterial centerlines.

Parameter	x	y	z
ADAN CoW centroid [cm]	$-1.397 \cdot 10^{-1}$	$-1.336 \cdot 10^{-1}$	$1.574 \cdot 10^{2}$
MRI CoW centroid [cm]	$-1.249 \cdot 10^{-2}$	$-1.839 \cdot 10^{1}$	$-6.830 \cdot 10^{-1}$
Translation vector [cm]	$1.475 \cdot 10^{-1}$	$-1.826 \cdot 10^{1}$	$-1.643 \cdot 10^{2}$
Scale factor	1.186	1.187	1.000

Note: CoW: Circle of Willis.

The result of registration is presented in figure 29. Having obtained these parameters, the registration using linear mapping is carried for each territory, and the next step is the projection of points onto the pial surface.

Figure 29 – Linear mapping of the ADAN model over the pial surface.
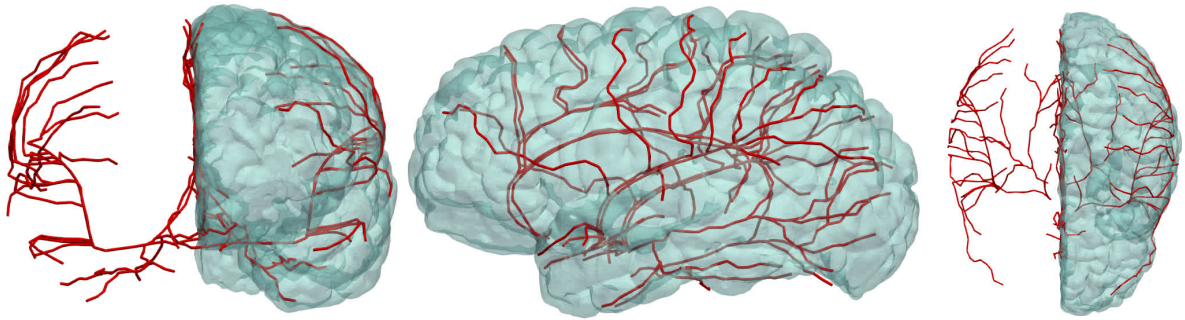
Left: coronal view; center: sagittal view; right: transverse view.

For the fine adjustment, a Python script is used to export the coordinates to Blender with the projection surfaces. The points are selected in *edit mode*, and snapped to the geometry with the *snap to face nearest* option, positioning them on the surface of the domain previously defined, and applying the transforms in Blender. This is repeated for each one of the arterial regions of the left hemisphere, ensuring the points are correctly projected onto the surface and follow a smooth path. Only the cerebral arteries that run over the cortex are projected, while the internal vessels are not. This is because they do not form a part of the pial network, are not in the perfusion domain, and serve the purpose of transporting the blood to the vascular network lying over the convexity. Figure 30 shows the points that define the cerebral vessels from the ADAN model onto the pial surface.

Finally, these already registered and projected points are saved in the original file (notice that connecvivity was never changed). The vessels in this initial vascular network are configured as rigid parent segments (TALOU et al., 2021), since they are not allowed to deform during the subsequent vascular generation. After this registration procedure, the initial vascular network follows for the next stage, which is the generation of the first

Figure 30 – Projection of coordinate points over the geometry.
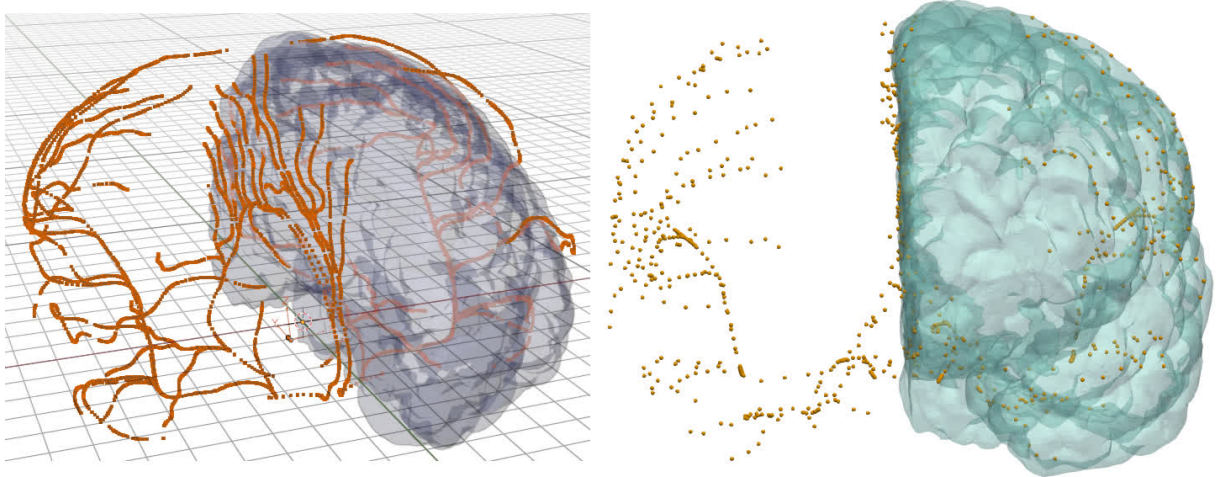
Left: projection of the mesh over the brain surface, in Blender; right: resulting projection after the mesh de-refinement, in ParaView, coronal view. Note: ADAN mesh points are shown in orange (left) and yellow (right), and the projection surface is shown in gray (left) and blue (right).

vascular vessels over the cortex, within the pial domain.

4.2.4 Boundary conditions: blood flow and pressure for the ADAN model

The boundary conditions of the model can be obtained from either a real patient or the literature. For this work, typical values of blood flow obtained from the ADAN model (BLANCO et al., 2015) were used for the inlet of each one of the initial vascular network corresponding to the three vascular territories. The values of inlet blood flow at the three entrances of the network are presented in table 4, together with the root radius at the entrance of each territory. That information is crucial in determining the conditions for the following generation stages.

Table 4 – Inlet parameters for blood flow and root vessel radius for each cerebral territory.

Parameter	ACA	MCA	PCA
Inlet blood flow [ml/min]	70	125	65
Root vessel radius [μm]	965	1041	869

Source: (BLANCO et al., 2015)

Since the cerebral vessels of the ADAN model were used as the initial vascular network with their respective diameters, it is not unreasonable to use the corresponding mean value of the blood flow as a boundary condition. These diameters were considered

for the generation of the vascular pial network. As will be discussed in chapter 5, smaller deviations in the order of 5% in the value of these diameters result in large discrepancies in the distribution of pressure in the generated networks. This is because a linear variation in these diameters results into a fourth-power variation in the hemodynamic resistance. This is why proper adaptations to the initial vascular network are needed, and will be carried after the generation of the full pial network (see chapter 5), in order to minimize the total discrepancy between the pressure distribution along vessels in each one of the three vascular territories.

(LINNINGER et al., 2013) also reports typical values used in the modeling of the human brain vascular system. Among these values, arterial blood pressure is important to verify the proposed procedure and also to guide the adaptations required in some of the initial vascular networks, while the capillary diameters assist in assessing the depth of generation. Table 5 presents these values. Regarding the pial arteries size, their diameters vary between around 150 µm down to 40 µm, where penetrating arterioles start to dominate.

Table 5 – Typical values used in the modeling of the cerebral microcirculation.

Parameter	Value
Vessel density [vessel/mm³]	9.487
Surface area per volume ratio [mm²/mm³]	13.60
Capillary diameter [µm]	6.46
Average capillary length [µm]	56.16
Fraction of vascular volume	2.49%
Pressure of arterial blood [mmHg]	85
Pressure in capillary vessels [mmHg]	50
Pressure in arterioles at 38 µm [mmHg]	65
Pressure in venules at 100 µm [mmHg]	18

Source: (LINNINGER et al., 2013)

4.3 Gray matter vascularization

Initially, the penetrating arterioles would be generated via CCO with a cost function depending on the length of the penetrating segment, without volumetric factor, restricting the plane angle to an orthogonal direction from the network. A cost functional evaluating an orthogonal direction was considered but discarded, as was the projection of the network onto the gray matter due to deformations created in the geometry of the network. The results of the optimization for this stage were not satisfactory, leading to terminals bifurcating multiple times, increasingly high cost of execution, deformations in projecting the pial network, among other issues.

The solution proposed next combines these ideas and uses a geometrical construction that iterates along the terminal vessels, and generates penetrating arterioles geometrically, without minimizing a functional, i.e. not making use of the CCO for this step. This permits to create the network following anatomical patterns reported in the literature (LAUWERS et al., 2008).

4.3.1 Geometric generation of penetrating arterioles

For generating penetrating vessels, two options were considered:

a) bifurcation of terminal vessels from terminal segments, exclusively, generating two penetrating vessels per terminal: one from the endpoint of the vessel, and one from the midpoint of the vessel;

b) free bifurcation from any vessel segment with diameter smaller than 60 µm.

A variation of the first technique was chosen. The optimization technique was replaced with the idea of a geometrical projection of the penetrating arterioles towards the gray matter domain, which mimics the patterns followed by the gray matter blood vessels found in (Reina-De La Torre; Rodriguez-Baeza; Sahuquillo-Barris, 1998), (LAUWERS et al., 2008), (SCHMID et al., 2019) and (HIRSCH et al., 2012). Notice that no CCO optimization or cost functional is used in this step, and generation is conducted sequentially without the use of partitions.

Descending segments bifurcate from the pial terminal vessels into the gray matter domain, delimited by the 3D geometrical volume between both the pial and the white matter surfaces. For each terminal, the algorithm creates two projection vessels that bifurcate towards the closest point lying over the pial surface, one from the endpoint of the terminal vessel, and one from the midpoint of the terminal vessel. Their maximum vessel length is set to 5 mm to avoid bifurcation in regions that do not contain gray matter, especially in the corpus callosum in the ACA territory (see figure 25).

Both the endpoint and midpoint of terminal vessels bifurcate to include upper boundaries in estimations of density of long and short penetrating vessels in the network (HARTUNG et al., 2021). In this work, only long penetrating vessels are generated, but the algorithm accounts for this possibility to further generate penetrating vessels in this situation.

At the end of each projection vessel, an additional segment, here called virtual trunk segment, continues penetrating the gray matter, in the direction of the surface normal at the point where the projection vessel touched the pial surface. The change in direction is not unreasonable as (Reina-De La Torre; Rodriguez-Baeza; Sahuquillo-Barris, 1998) presents descending and penetrating segments in different directions. This virtual trunk segment is where the gray matter network will continue to be generated, and it

stops when it reaches the opposite boundary (i.e. the interface between the gray and white matter tissues), or when its length reaches a maximum of 2.5 mm (SCHMID et al., 2019) to avoid crossing the domain, especially in the gyri.

Their aspect ratio is also verified, having their length at least the size of the parent vessel diameter, otherwise the segment is removed. Figure 31 illustrates how this bifurcation occurs from the pial domain towards the cortex.

Figure 31 – 2D and 3D illustration of the penetrating vessels from the pial network towards the gray matter.
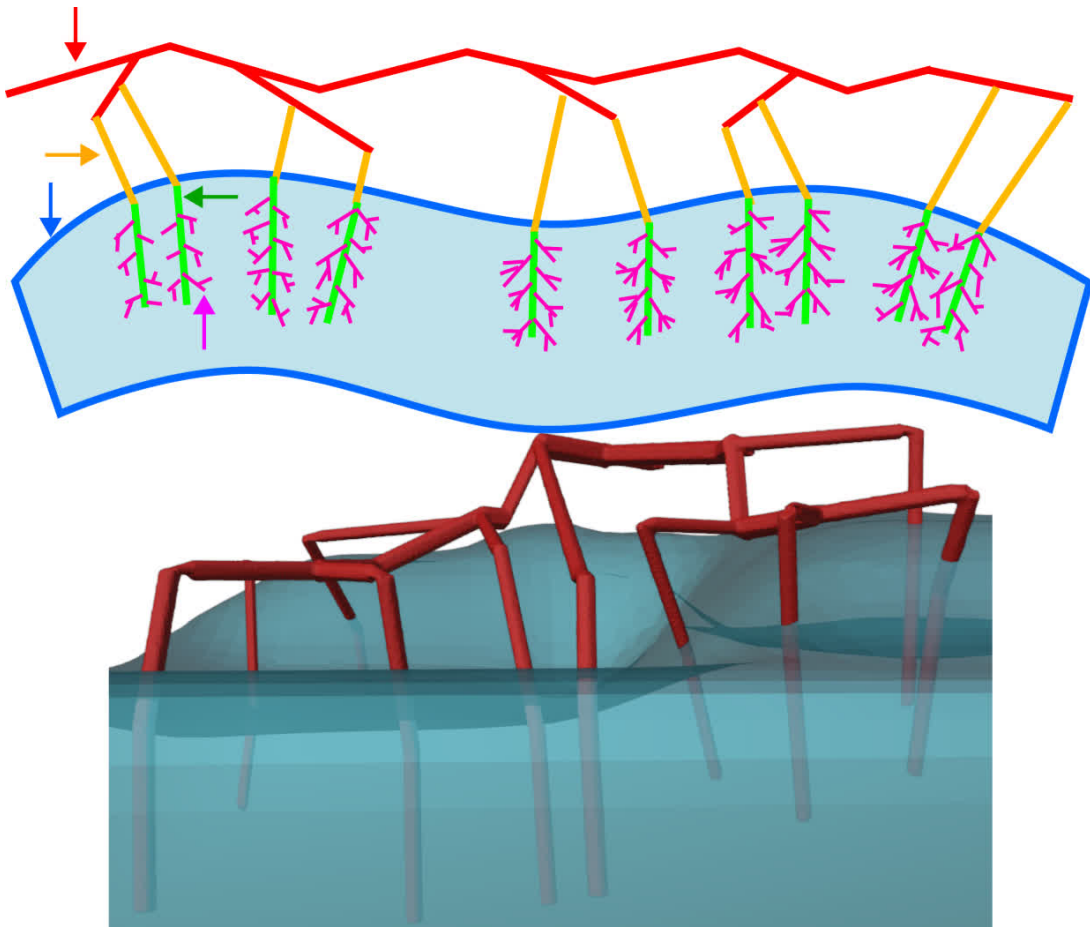
Top: 2D illustration, the gray matter is presented in blue, pial network is shown in red, penetrating vessels are shown in orange, virtual trunk segments are shown in green, and the gray matter arborization, still to be explained, is shown in magenta. Bottom: 3d illustration, gray matter is shown in cyan, and pial network, penetrating vessels, and virtual trunk segments are shown in red.

For this step, the segments in the pial network had to be modified using a Python script, with the following properties:

a) terminal vessels, where descending arterioles start, had its function set as *transport*, and branching mode set as *distal parent* when bifurcating from the

endpoint, and *rigid parent* when bifurcating from the midpoint of the vessel;

b) non-terminal vessels are kept as distribution, and set as *no-branching* mode.

Penetrating arterioles should be generated as *perforator* vessels with *distal branching* mode.

The generation of the penetrating segments given the pial surface and the interface boundary between gray and white matter tissues occurs as described by algorithm 2. The results are the penetrating vessels added to the pial network, and the coordinates of the virtual trunk segment where gray matter microvasculature will be constructed. Tree diameters are updated for each territory according to (MURRAY, 1926) and equation 3.1 when the vascularization is completed.

Algorithm 2 Penetration of the gray matter.

1: **procedure** PENETRATING VESSELS GENERATOR(pial network, gray space, parameters)
2:    filter all terminal vessels in the pial network
3:    **for** every terminal vessel in the pial network **do**
4:        **for** both endpoint and midpoint of the vessel **do**
5:            set the initial point to endpoint or midpoint, depending on the case
6:            calculate the projection of this point towards the closest point over the pial surface
7:            obtain this closest point
8:            find the triangle over the pial surface that contains this point
9:            obtain the normal vector in the triangle over the pial surface
10:            check if geometrical constraints are satisfied
11:            ▷ *maximum distance, aspect ratio*   ◁
12:            **if** projection vessel does not satisfy the geometrical constraints **then**
13:                discard this vessel
14:                **continue** the for-loop at the next case
15:            **else**   ▷ *penetrating vessel is valid*
16:                add the projection vessel bifurcating from the initial point towards the closest point
17:                navigate inwards in the normal direction to find the opposite boundary, or stop at 2.5 mm
18:                **if** aspect ratio is satisfied **then**
19:                    save the coordinates of this new vessel as a virtual trunk segment
20:                **else**   ▷ *vessel is too short*
21:                    discard this penetrating vessel and move to next case
22:        repeat for the endpoint/midpoint
23:    iterate for the other terminal vessels in the pial network

---

4.3.2 Generation of gray matter sub-trees

These sub-trees are small, pre-generated networks carried in a small domain, that comprehend the cortical columns viewed in chapter 2. The parameters for the generation

of the population of sub-trees are detailed in chapter 5.

The population of gray matter microvascular arborizations, also called the sub-trees, are generated via CCO before the appending into the network. These arborizations replace the virtual trunk segments created in the previous stage when penetrating the gray matter space. For the generation domain, hexagonal prisms were chosen for the space filling with 2 mm of length and 1 mm of diameter of the circumscribed cylinder. These hexagonal prisms are an improvement of the original cylinders, and are considered easier to be stacked in the domain, reducing overlapping, and filling better the domain. Other works (LINNINGER et al., 2013) considered cuboids for the space filling. Figure 32 shows other possible sub-trees that can be generated with the method.

Figure 32 – Various models of sub-trees that can be generated.
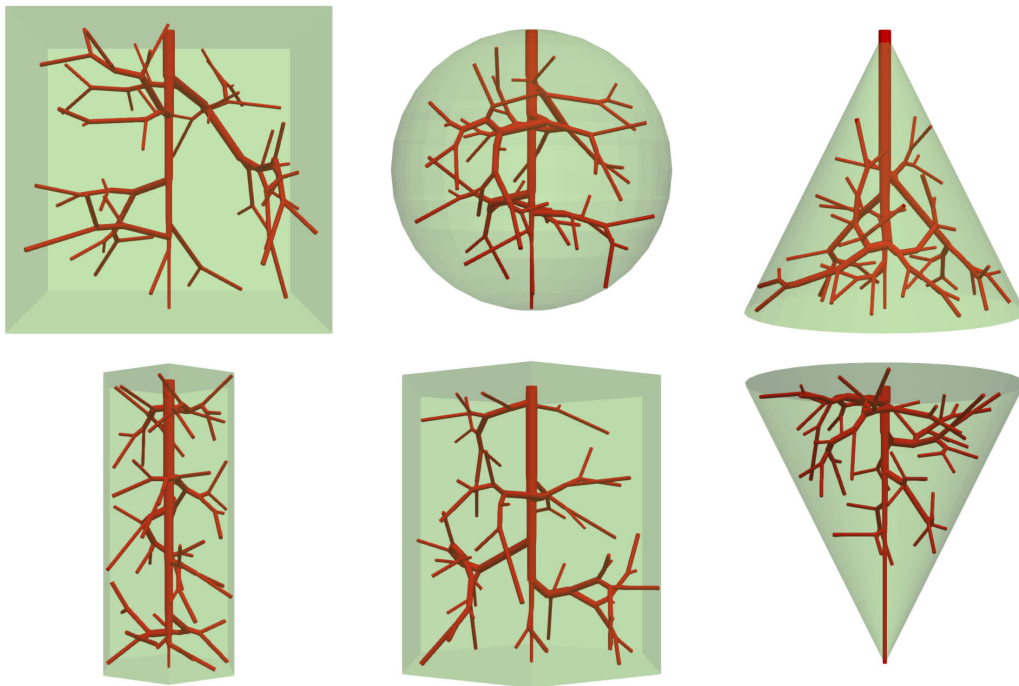
Top row: cubic domain, spherical domain, inverse conical domain. Bottom row: hexagonal domain (1 mm diameter), hexagonal domain (2 mm diameter), conical domain. Sub-tree networks are shown in red, and the sub-tree domain in light green. The hexagon with 1 mm of circumscribed diameter was chosen for this work.

Each sub-tree consists of an axial segment from where bifurcating vessels sprout from the center, as shown in (CASSOT et al., 2006). A population of 100 different sub-trees was generated by altering the seed of generation. Each sub-tree contains 51 terminal segments, or 101 segments of blood vessels.

For generating the population of sub-trees, the following steps were made:

a) create a hexagon in Blender, with 2.0 mm of length and 1 mm of circumscribed diameter, i.e. between vertices;

b) prepare this geometry to be a perfusion domain of the sub-tree;

c) create one initial segment, axially, representing the penetrating arteriole;

d) bifurcate this penetrating vessel into 100 more segments using CCO;

e) vary the seed and generate a population of cortical structures.

The entrance of the penetrating vessel starts at the origin $(0, 0, 0)$ and continues axially until the point $(0, 0, h)$, where $h = 2.0$ mm is the height of the hexagon. These coordinates will later be mapped to the virtual penetrating vessels in the network. The inlet diameter of these sub-trees is initially set as 50 µm, and they will be updated after their appending. The height $h = 2.0$ mm can be varied when testing for long and short penetrating vessels, between 1.0 mm and 2.5 mm, and the majority between 2.0 mm and 2.5 mm (WEBER et al., 2008; LAUWERS et al., 2008; CASSOT et al., 2006). The diameter $0.86\,\text{mm} \leq D \leq 1.0\,\text{mm}$ of the cortical structures varies between 600 µm and 1000 µm for a single penetrating arteriole (HIRSCH et al., 2012; NISHIMURA et al., 2007), while other papers list the diameter between 250 µm and 500 µm wide (Reina-De La Torre; Rodriguez-Baeza; Sahuquillo-Barris, 1998). The parameters for the generation of the sub-tree population will be presented in chapter 5 Figure 33 presents a sample of the sub-tree structure generated inside the hexagonal prism domain. Figure 34 shows a small sample of 10 sub-trees generated to be appended to the network.

Figure 33 – Hexagonal prism domain with one penetrating sub-tree generated.
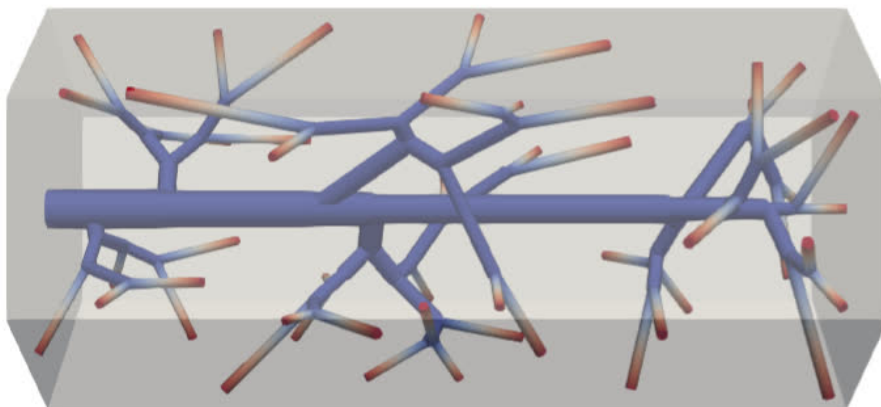
Note: Red tips are terminal points of the penetrating sub-tree.

In the end, the result is a population of sub-trees representing the penetrating structures in the gray matter, that can be appended in the correct position of each

Figure 34 – Sample of 10 sub-tree structures generated.
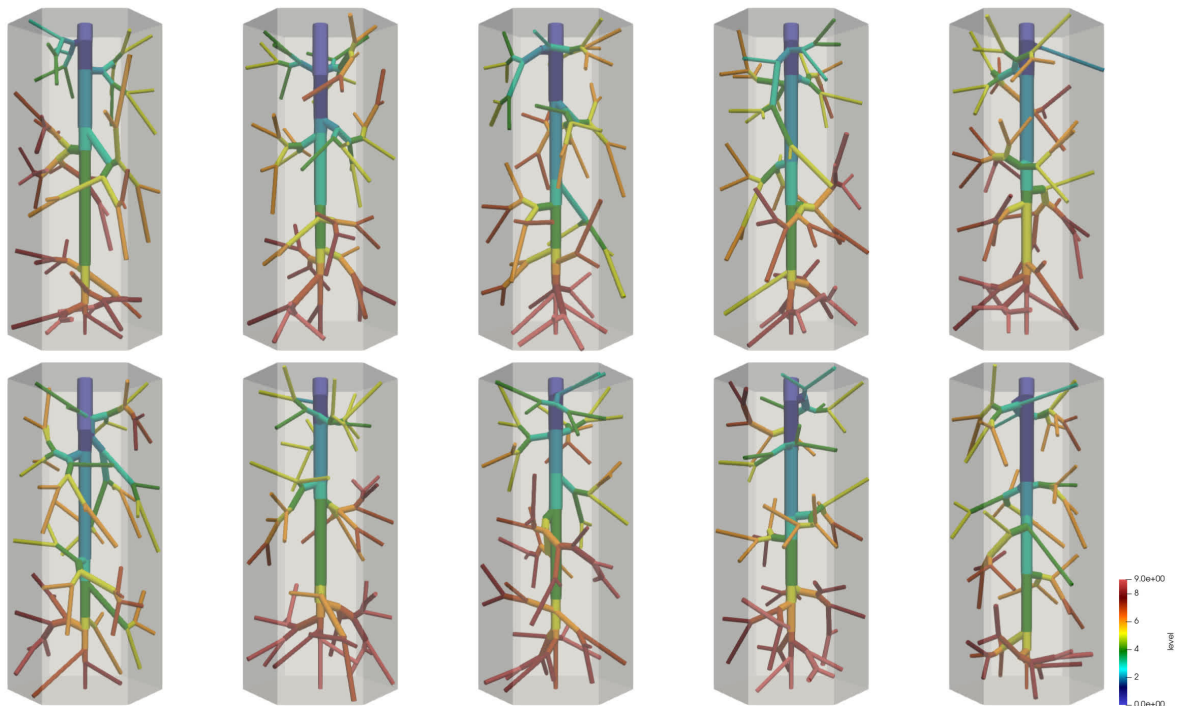
Note: Colors denote levels of bifurcation further away from the entrance of the structure.

penetrating arteriole, considering length and diameter sizes. Regarding the distribution of long and short penetrating vessels, the bias reported by the literature is around 70% and 30% respectively (HARTUNG et al., 2021), however this work considers them a single type, long, for establishing the proper grounds of generation.

4.3.3 Appending of the gray matter microvasculature

The gray matter microvasculature is generated separately from the penetrating arterioles, extending from the latter to perfuse the gray matter in the cerebral cortex. Generation via classic optimization techniques faces problems due to the large number of vessels, in the order of millions. Dividing the task into smaller partitions still results in an expensive task, increases complexity, and rises challenging issues in the merging of the network. Other obstacles include the amount of computational memory needed to accommodate the generation, and the impracticability of loading and saving larger files when partitioning the tree.

The solution proposed here circumvents the cost by efficiently pre-generating the cortical arborizations, or sub-trees, akin to what was done in (LINNINGER et al., 2013). A collection of penetrating structures is generated mimicking the gray matter network to comply with the morphology (CASSOT et al., 2006), and this population is sampled

and appended to the penetrating vessels, by replacing each virtual trunk segment with a corresponding arborization. By appending an entire sub-tree instead of single vessels, the number of operations is simplified, and the algorithm iterates relatively fast.

The algorithm for appending the pre-generated arborizations to the network and replacing the virtual trunk segments with the sub-trees is presented in algorithm 3. The population of the sub-trees was done as described in the previous subsection.

Algorithm 3 Gray matter vascularization.

1: **procedure** APPENDING SUBTREES(penetrating vessels, subtree population, parameters)
2:     load and instantiate the base tree
3:     get the list of the sub-trees
4:     load the sub-tree population
5:     filter the penetrating vessels in the base tree
6:     select appropriate parent vessels of the sub-tree
7:     **for** each penetrating segment **do**
8:         get the coordinates of the virtual trunk vessel
9:         get the virtual trunk vessel length
10:        sample a sub-tree from the population
11:        instantiate and import the structure with its coordinates
12:        ▷ *apply a linear map to the subtree into the correct position as dictated by the*
           virtual trunk segment   ◁
13:        resize the sub-tree coordinates to the correct length
14:        rotate the sub-tree to the correct orientation
15:        translate the sub-tree to the correct position
16:        append the sub-tree to its parent in position
17:        **continue** to the next penetrating arteriole
18:    ▷ *after all the sub-trees have been appended, do the following*   ◁
19:    update the tree diameters
20:    update the viscosity and blood pressure

The linear map described in algorithm 3 for the proximal and distal points of the sub-tree vessels, contains the following steps:

a) resize the sub-tree coordinates to the correct length of the virtual trunk segment;

b) rotate the sub-tree to the correct alignment in the orientation of the virtual trunk vessel;

c) translate the sub-tree so that the root vessel matches the endpoint of the parent vessel where it is appended.

Note that the diameters of the sub-tree structure are not updated at this step, as they are updated at the end of the algorithm 3, since updating at every step would vastly increase the cost. The illustration of this process is presented in figure 35.

Figure 35 – Illustration of the linear mapping for a sub-tree into the virtual vessel trunk.
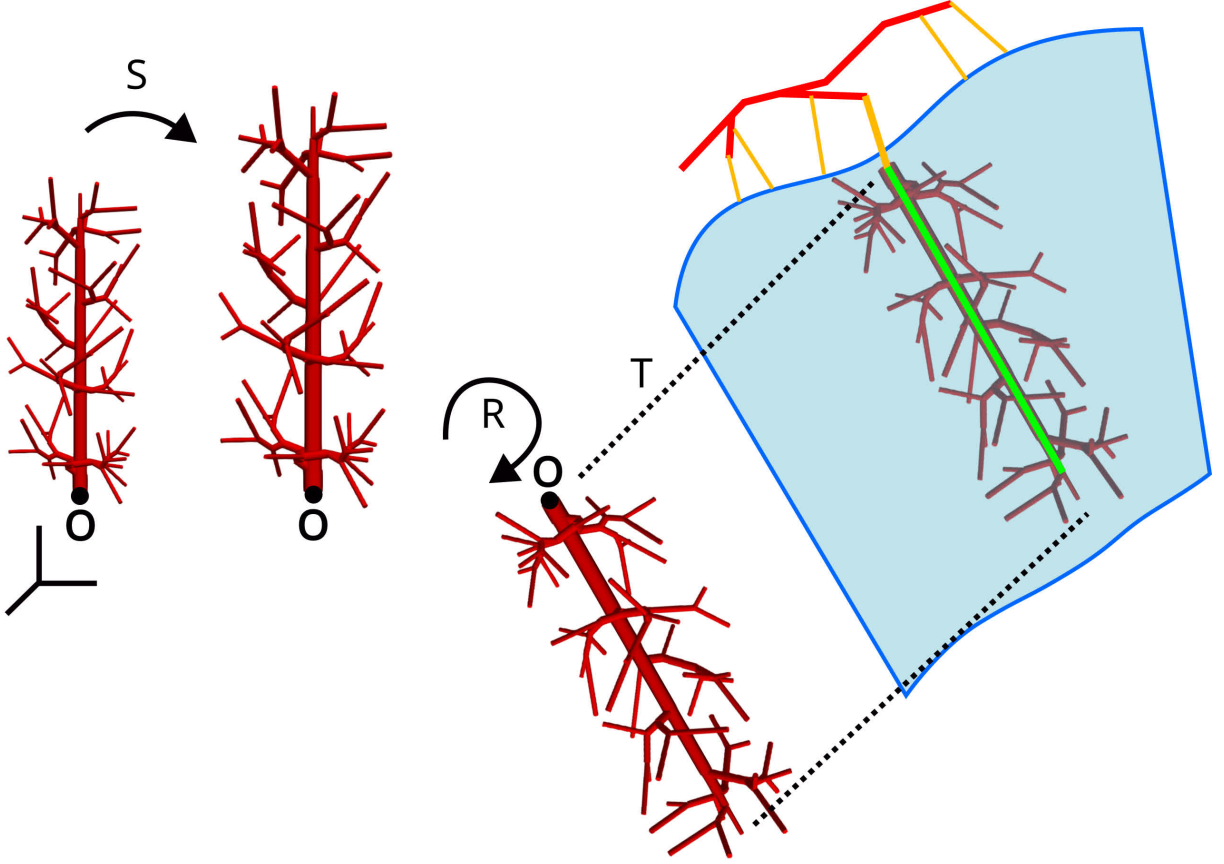
Note: Resizing is denoted by **S**, rotation by **R**, and translation by **T**. The virtual vessel trunk is the segment in green. In this system of coordinates, **O** is the origin.

The resizing for a point p_0 into p_s is

$$p_s = p_0 \times f_s \tag{4.2}$$

and the scale factor f_s is the ratio between the virtual trunk vessel length and the sub-tree height h, which is determined by

$$f_s = \frac{||x_{\text{dist}} - x_{\text{prox}}||}{h}, \tag{4.3}$$

where x_{dist} and x_{prox} are the distal and proximal points of the virtual trunk segment to be replaced. The scale factor is limited to a lower bound where the length of the sub-tree must be at least the diameter of the parent vessel.

After the resizing of the sub-tree, the rotation transforms the point p_s into p_r, aligned with the virtual vessel trunk, and this rotation is calculated by a matrix R_{rot} obtained via the Rodrigues' algorithm (LIANG, 2018),

$$p_r = R_{\text{rot}} \, p_s, \tag{4.4}$$

where

$$R_{\text{rot}} = I_{\text{Id}} + K + \frac{(K^2)}{1 + \cos(\theta)}, \quad (\theta \neq \pm\pi), \tag{4.5}$$

and

$$K = v \wedge u - u \wedge v. \tag{4.6}$$

In these equations, u is the original sub-tree direction vector, and v is the virtual trunk segment direction, θ is the angle between them, I_{Id} is the identity matrix, and $v \wedge u$ denotes an outer product. If θ is close to 0 or $\pm\pi$, then R_{rot} is the identity or its negative.

Finally, the translation of p_r into p_t, the final position of the sub-tree, is obtained by adding the displacement x_p between the virtual vessel and the sub-tree root node proximal points, that is

$$p_t = p_r + x_p. \tag{4.7}$$

The sub-trees in this work are generated in chapter 5 with its associated parameters. The method proposed in this work results in possible collisions of sub-tree structures along the gray matter space, due to possible penetrating vessels that are sufficiently close to each other. This limitation was not circumvented for this work, since the computational steps required for checking all sub-tree collisions would greatly increase the cost of generation. In the end, the gray matter network for each territory is generated thoroughly with relatively low computational cost, even without parallelization.

5 Results: Vascular generation

This chapter presents the generation for the vascular network, and its results. First, the pial network for the entire left hemisphere is generated, and after that, the vascularization for the perfusion of the gray matter in the cortex is built, by penetrating arborizations bifurcating from the pial network. The anatomical characteristics of the cortex were presented in chapter 2 and 4. Before starting this chapter, a few definitions for the nomenclature are useful for clarity: a *domain* is a geometrical space where vascularization is generated, either pial surface or gray matter; a *territory* is a portion of the domain fed by one large cerebral artery, being the Anterior (ACA), Middle (MCA), or Posterior Cerebral Artery (PCA), and a *partition* is a subdivision of any territory where parallelized generation occurs.

The PDCCO algorithm (CURY et al., 2021) is used to fill the pial domain of the brain by creating a network of blood vessels to fill each one of the three arterial territories, covering along the entirety of the gyri and sulci on the pial surface between the cortex and the cerebrospinal fluid. This network is built following a multi-staged approach, which considers the Fahraeus-Lindqvist effect (FÅHRÆUS; LINDQVIST, 1931), and has boundary conditions for the blood flow at the inlet point obtained from the ADAN model (BLANCO et al., 2015) in table 4. After the generation of the pial network, the gray matter vasculature is generated from its terminal vessels, penetrating the cortical matter and generating the gray matter deep network. In a nutshell, the generation follows the workflow below:

a) first, generate the pial network, by sprouting growth of the base tree for each territory;

b) then, subsequent stages of space-filling expand the the pial domain into a denser network by growing more segments;

c) penetrating arterioles are created from the terminal vessels of the pial network;

d) from the penetrating arterioles, smaller vessel networks are created to perfuse the gray matter region.

The following sections present each step of generation.

5.1 Generation of the pial network

This section presents the generation of the pial network, along with considerations and parameters used. Starting from the CCO input file obtained from the adjustment of the initial ADAN model, and the geometry of the pial domain, the VItA algorithm

in C++ is used to create the pial network. Generation of the pial network was found to run faster when the domain is considered as a single solid, rather than two delimiting surfaces, therefore the *SimpleDomain* domain was considered in VItA. The parameters for generation were based on the cortical parameters from (TALOU et al., 2021), and were adapted to understand the behavior in the generation, especially the ones related to network sprouting.

Murray's power law for bifurcating branches in the blood vessels (MURRAY, 1926) has been mentioned in chapter 3. This parameter, denoted gamma (γ), influences the generation as larger values of γ result in slower decay of diameters in the network for each bifurcation. Similarly, smaller values of γ result in faster decaying diameters. This results in the variation of pressure drop to the terminals of the network for different values of γ.

The generation of the pial network was conducted for two values of gamma, $\gamma = 3.0$ and $\gamma = 3.5$, to account for the pial arteries ranging between 3.0 and 3.6 as reported in (CASSOT et al., 2010), and they are kept constant throughout generation of the ACA, MCA and PCA territories. The results for both values 3.0 and 3.5 of γ are presented below. After generation, the results are evaluated to compare and find the best value of γ to model the pial network, and chosen to continue the gray matter perfusion.

5.1.1   Sequential generation for the initial pial network

For each territory, generation starts with the base tree extracted from the ADAN model, correctly registered onto the vascular domain, as explained in chapter 4. The first stage considers the *Sprouting* functional type from equation 3.15, with volumetric, proteolytic and diffusive costs, favoring the branching from smaller diameters rather than large diameters, and favoring new shorter vessels. This way, the fundamental aspects of the initial network are mostly unchanged, while the second stage makes use of the purely-volumetric functional from equation 3.14, providing greater uniformization of the network in smaller scales. The first and second stages of generation of the base pial network used the parameters in VItA presented in table 6 to expand the initial tree.

The number of terminals generated in the first stage is proportional to the volume of each cerebral territory (ACA, MCA, PCA), and is presented in table 7. The total quantity of terminals is obtained from the surface area of the territories, shown in chapter 4. Figure 36 shows the first two stages of the generation in the pial network, and figure 37 shows for each territory.

The sequential generation stops when reaching 20 000 terminals in the entire hemisphere. Following the sequential generation becomes expensive, as explained in (CURY et al., 2021), and a distributed parallel generation is a more viable approach for an equivalent tree, as time required to generate is considerably shorter when most terminals

Table 6 – Parameters used for generation of the first two stages of the pial network.

Parameter	First stage	Second stage
Gamma exponent	3.0 and 3.5	3.0 and 3.5
Symmetry factor	0.4	0.0
Perfusion area factor	0.1	0.1
l_{min} reduction factor	0.9	0.9
Neighborhood factor	100	100
Segments per bifurcation	7	7
Number of terminals	(See tab. 7)	(See tab. 7)
Functional type	Sprouting	Volumetric
Sprouting parameters	$C_v = 1.0 \cdot 10^4, C_p = 0.5, C_d = 1.0$	—
Vessel type	Distribution	Distribution
Minimum bifurcation angle	20 deg	20 deg
Minimum plane angle	0 deg	0 deg

Table 7 – Number of terminals generated in the pial base network for the first two stages.

Number of terminals	ACA	MCA	PCA	Hemisphere
First stage	1 300	1 700	1 000	4 000
Second stage	6 500	8 500	5 000	20 000

are saved for the partitioned stages. Some parameters, e.g. the characteristic length l_{min}, are passed to subsequent stages to avoid artifacts in the generation and keep the network consistent.

5.1.2 Parallelization of the pial network

This stage is responsible for the completion of the vascular network within the pial vascular domain, completing the spatial range and vascular density targeted before the penetration of the gray matter. The partition of the territories follows the PDCCO procedure in (CURY et al., 2021), and as shown in table 2, the ACA is subdivided into 7 partitions, 8 for MCA, and 6 for the PCA territory, each territory having its own stage number associated. After the parallelized generation, the networks are merged into a final network.

The parameters used for the parallel generation of the pial network are presented in table 8, and they are generated as distribution vessels for proper merging into the final pial network.

The targeted number of terminals NT_{total} in the pial network to reach 100 penetrating vessels per cm² (SCHMID et al., 2019) is obtained from the area calculated from the volume in table 2 by considering the thickness of partitions being 0.2 cm. The number of terminals generated is 20% above the projected quantity, by multiplying the pial surface area by a factor of 1.2, creating a safety threshold to fully cover the pial surface in compensation for eventually discarded terminals when generating penetrating vessels. To

Figure 36 – Generation for the first two stages of the network.
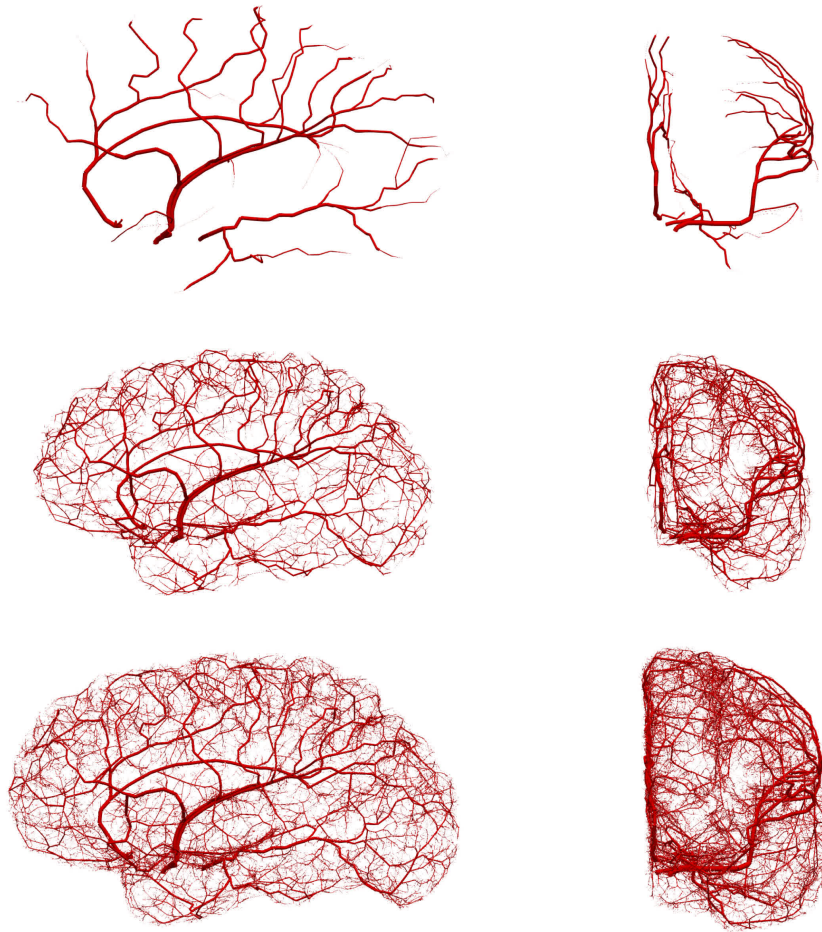
Note: Top row: initial tree; middle row: first stage; bottom row: second stage. Left: sagittal view; right: coronal view.

Table 8 – Parameters used for generation of the parallelized stages in the pial network.

Parameter	Parallelized stage
Gamma exponent	3.0 and 3.5
Symmetry factor	0.0
Perfusion area factor	0.1
l_{min} reduction factor	0.9
Neighborhood factor	100
Segments per bifurcation	7
Number of terminals	(See tab. 9)
Functional type	Volumetric
Sprouting parameters	—
Vessel type	Distribution
Minimum bifurcation angle	20 deg
Minimum plane angle	0 deg

Figure 37 – Generation for the first two stages of the network in each territory.
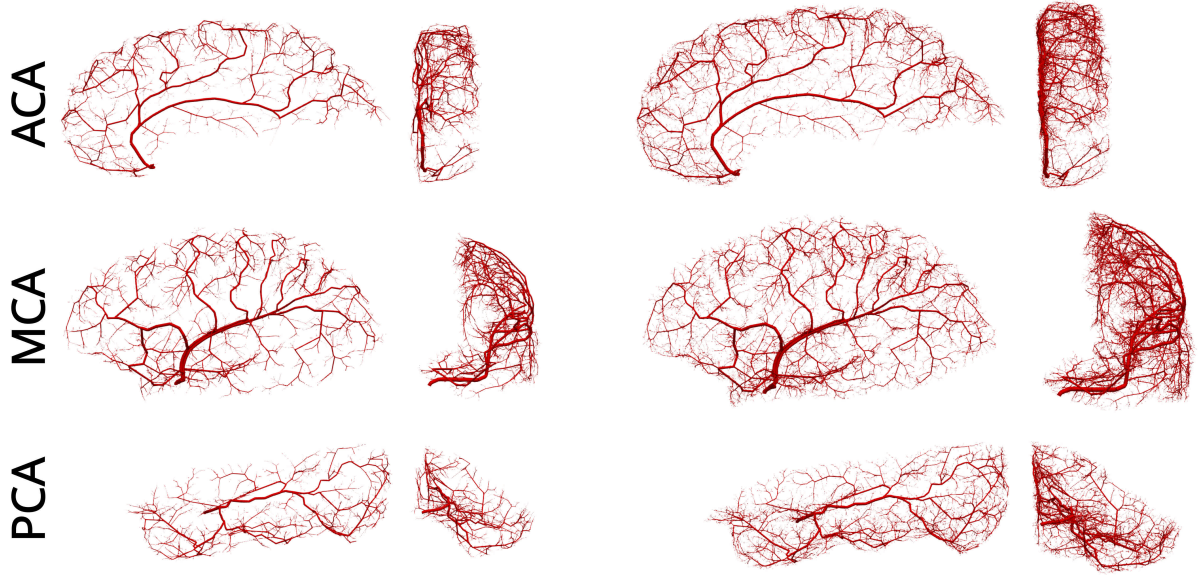
Note: Left column: first stage; right column: second stage. Sagittal and coronal views respectively.

find the number of terminals targeted in this stage for each partition NT_{part}, we calculate the number of terminals in the base network BT plus the number of terminals added for each partition PT_{added}

$$NT_{\text{part}} = BT + PT_{\text{added}} \quad \text{(for each partition)}, \tag{5.1}$$

and PT_{added} is proportional to the fraction of volume f_{vol} for the partition, the ratio between its volume Vol_i to the total volume of the territory calculated from table 2, and is defined by

$$f_{\text{vol}} = \frac{\text{Vol}_i}{\sum_{i=1}^{N} \text{Vol}_i}. \tag{5.2}$$

In other words, we find the quantity needed to add in each partition as follows

$$PT_{\text{added}} = (NT_{\text{total}} - BT) \times f_{\text{vol}} \quad \text{(for each partition)}, \tag{5.3}$$

in which $NT_{\text{total}} - BT$ is the total number of terminals added in this stage, remembering BT is considered redundantly in all partitions and the total quantity is not obtained from the sum of each final target. This way, each partition contains a proportional number of terminals, and when added up, yields the expected total target number of the network as

$$NT_{\text{total}} = BT + \sum_{i}^{N} PT_{\text{added}} \quad \text{(in total)}. \tag{5.4}$$

The quantity of terminals generated in each partition for each territory is listed in table 9, including the quantity in the final pial network. These quantities are passed to

the algorithm together with the partitions, and added to the base terminals of the tree. The generations colored for each partition for each territory are shown in figure 38.

Table 9 – Quantity of terminals generated in the parallelized stage, for each partition, for each territory.

Part.	ACA (new)	ACA	MCA (new)	MCA	PCA (new)	PCA	Hemisphere
Base	—	6 500	—	8 500	—	5 000	20 000
1	3 795	10 295	3 980	12 480	3 786	8 786	—
2	2 884	9 384	5 430	13 930	3 922	8 922	—
3	5 281	11 781	6 305	14 805	3 028	8 028	—
4	4 203	10 703	5 140	13 640	3 574	8 574	—
5	4 548	11 048	4 505	13 005	5 868	10 868	—
6	5 035	11 535	8 285	16 785	2 401	7 401	—
7	5 557	12 057	5 610	14 110	—	—	—
8	—	—	3 840	12 340	—	—	—
Total	31 303	**37 803**	43 095	**51 595**	22 579	**27 579**	**116 977**
%	—	32%	—	44%	—	24%	100%

Note: when adding the total number of terminals, the correct method is adding the new vessels, and then adding the base network, to avoid counting multiple times the base tree in each partition.

After all the partitions have finished their generation, the resulting networks for each partition of the pial territories are now merged in VItA according to the methodology in (CURY et al., 2021) into one single vascular network for each territory. This merge occurs by comparing each partition tree to the base tree, and sequentially appending the newly generated segments into each parent segment with the appropriate coordinates. This is the reason why partitions have to be disjointed, otherwise, the same segment could bifurcate in two partitions, and the merging process would fail. It is important that this merge occurs before the generation of any gray matter structure, since this pial network is the base tree for the gray matter generation.

The resulting pial network for the case of $\gamma = 3.0$ is presented below in figure 39, and the steady-state pressure field, as given by the PDCCO algorithm, is shown in figure 40. The results for $\gamma = 3.5$ are almost identical, and will be analyzed in the following sections.

Figures 41 and 42 show the resulting network, by applying a threshold in vessel diameter for each step.

5.2   Analyses in and properties of the pial network

5.2.1   General characteristics of the pial network

The final pial network is analyzed to evaluate its characteristics, and define the network with best value of γ for subsequent stages. The distribution of terminal vessels

Figure 38 – Full pial network for all the three territories with colors for each partition.
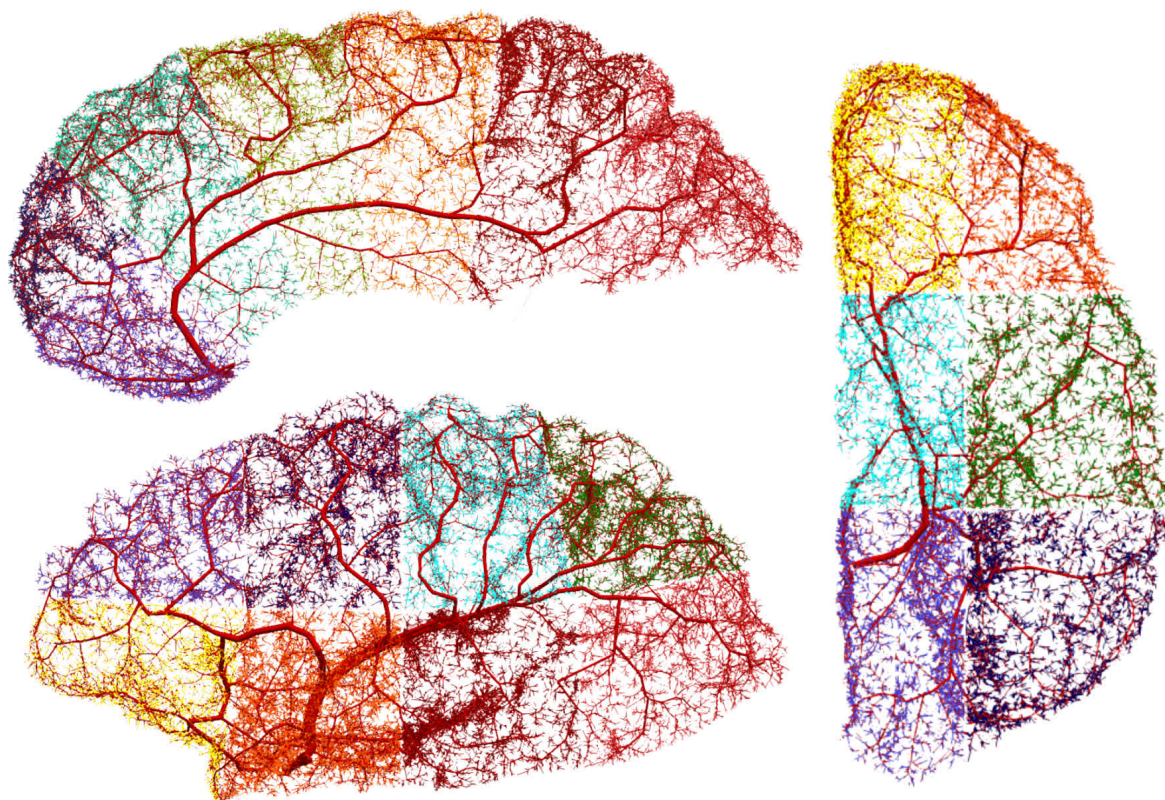
Note: Partitions are colored differently for better visualization in the network.

Figure 39 – Full pial network including the vascularization in the partitions performed in a distributed manner.
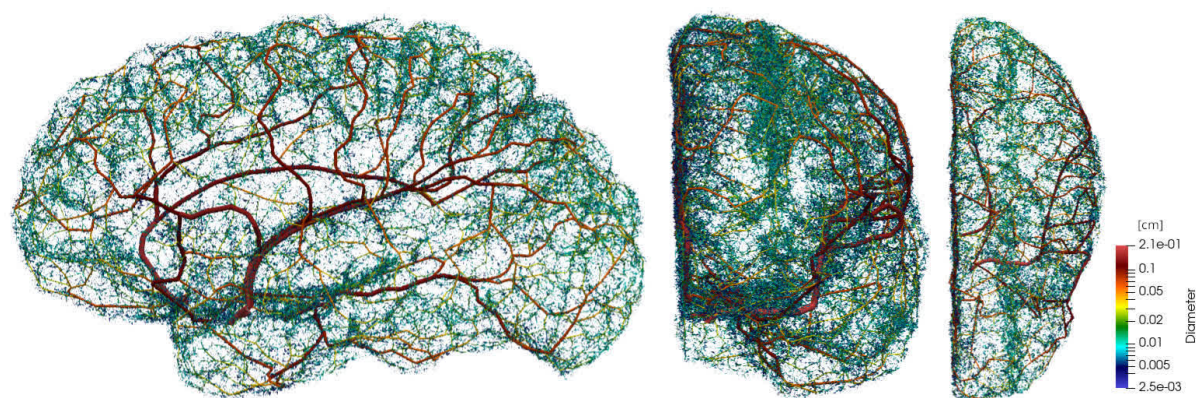
Note: Vessels are colored by diameter, in cm.

Figure 40 – Steady-state pressure field in the pial network including the vascularization in the partitions performed in a distributed manner.
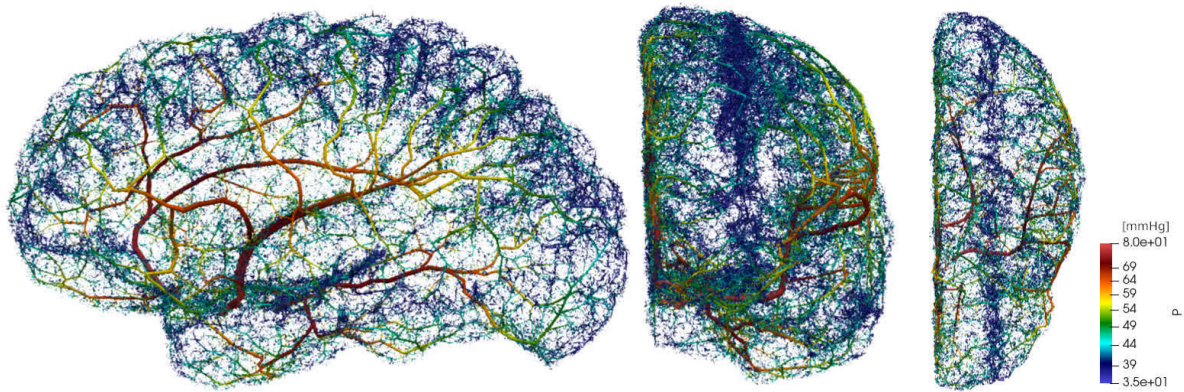
Note: Vessels are colored by pressure, in mmHg.

shown in table 9, and summarized below in table 10, presents 32% of the blood vessels in the ACA territory, 44% of the terminals in the MCA region, and 24% of the vessels in the PCA territory. The total number of terminal vessels is 116 977, and the total number of segments reaches 233 984.

Table 10 – Number of terminals and segments in the pial network.

Quantity	ACA	MCA	PCA	Hemisphere
Terminals (pial)	37 803	51 595	27 579	116 977
Segments (pial)	75 700	103 048	55 236	233 984
Percentage	32%	44%	24%	100%

Considering the volume and surface area for each major vascular territory presented in table 1 (see chapter 4), these values result in a density of 120 terminals per cm², or 1.2 terminal per mm², which is within the desired range of generation for the pial domain. For the total number of segments in the pial domain, the blood vessel density is or 1.199 vessel per mm³, which is way below the value found in the literature (LINNINGER et al., 2013), but this is only for the pial surface, and thinner capillary vessels are not included. The values of terminal density and vessel density are numerically similar because the terminal quantity in binary trees is proportional to the number of segments, and the domain has uniform thickness. The values for all territories are shown in table 11.

The total length of the pial network is 171 103.7 mm, or 171.1 m. The total volume of the blood vessels in the pial network is 2877.21 mm³ resulting in a fraction of vascular volume, with respect to the volume of the pial space (occupied by the cerebrospinal fluid), of 1.48%, and the MCA territory has a higher fraction due to being the largest territory and having the presence of larger cerebral arteries.

Figure 41 – Visualization of the pial network as a function of vessel diameter in lexicographic order, from larger vessels only down to the entire network, inclusion of vessels follows a given threshold for the diameter, sagittal view.
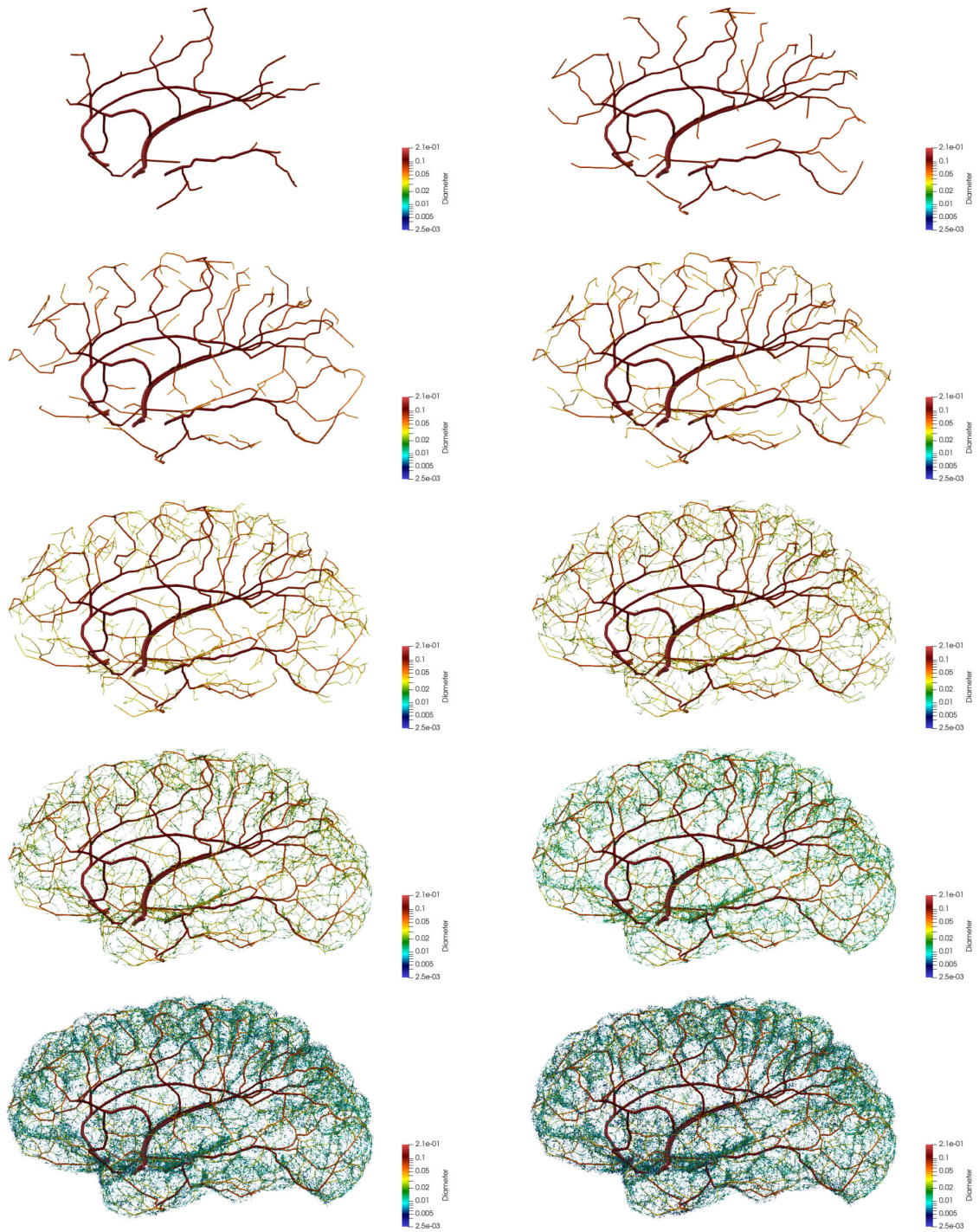
Note: Vessels are colored by diameter, in cm.

Figure 42 – Visualization of the pial network as a function of vessel diameter in lexicographic order, from larger vessels only down to the entire network, inclusion of vessels follows a given threshold for the diameter, coronal view.
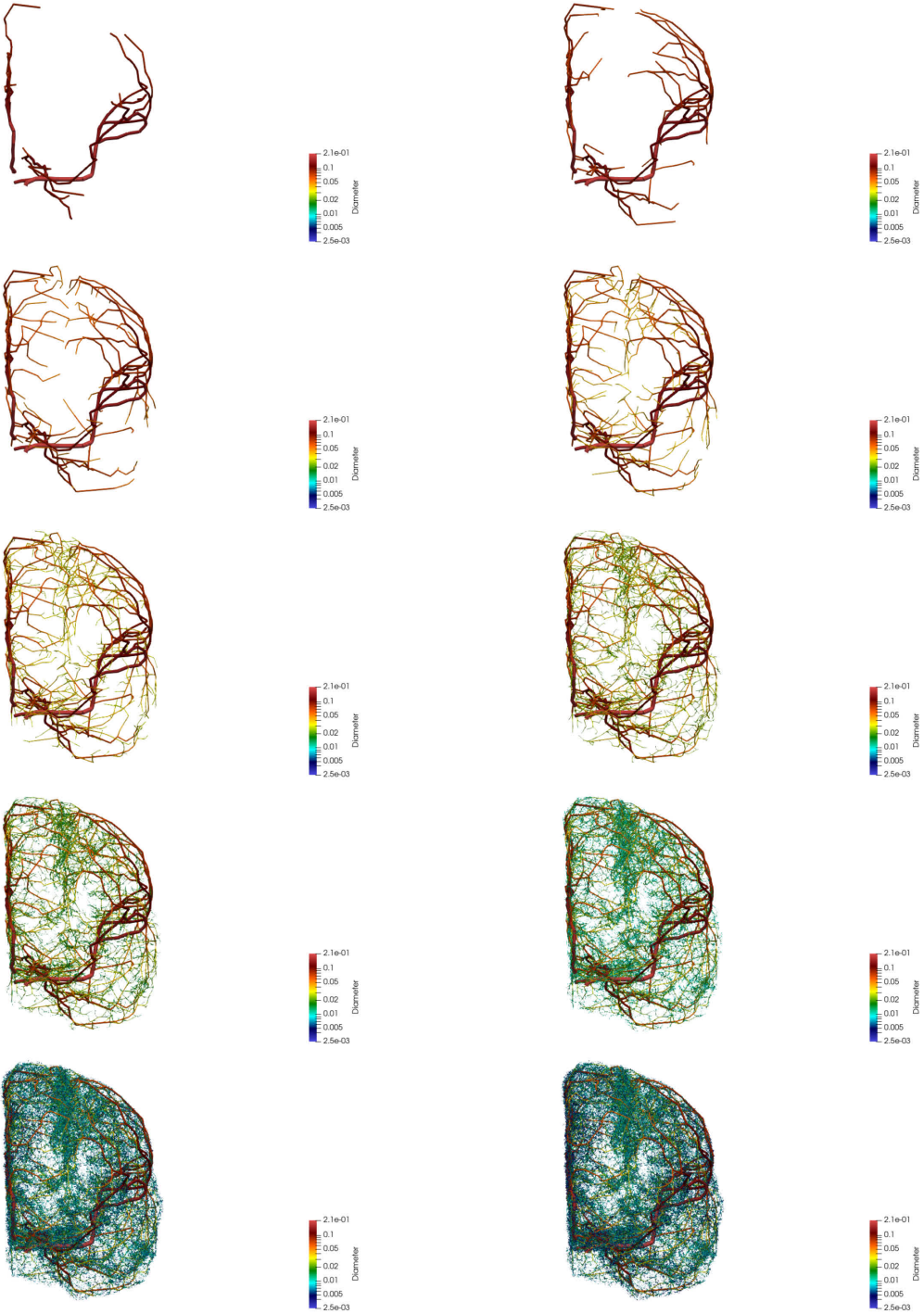
Note: Vessels are colored by diameter, in cm.

Table 11 – Resulting characteristics of the pial network.

Characteristic	ACA	MCA	PCA	Hemisphere
Terminal density [qty/mm²]	1.2001	1.1999	1.1991	1.1998
Vessel density [qty/mm³]	1.190	1.195	1.180	1.199
Network length [mm]	55 345.1	75 246.0	40 512.6	171 103.7
Vascular volume [mm³]	854.88	1442.78	579.55	2877.21
Fraction of volume (pial)	1.34%	1.67%	1.24%	1.48%

Note: (1) Vascular volume and fraction of volume are presented for the case when $\gamma = 3.0$. (2) These values are considered after the network equalization presented in this chapter (see section 5.2.5), that corrected the diameters of the ACA and PCA territories. (3) The fraction of volume for the pial network is calculated with respect to the volume of the pial space used in generation.

5.2.2 Distribution of blood vessel diameters in the pial network

The distribution of blood vessels and terminals is compared with values mentioned in chapter 2 and 4. When $\gamma = 3.0$, the diameters of the terminal vessels lie between 40 µm and 60 µm, thus being in the expected value of 50 µm in diameter, agreeing with the size of penetrating arterioles presented in (DUVERNOY; DELON; VANNSON, 1981). Furthermore, this is important because it achieves the expected value of vessel diameters in the correct terminal density, validating the assumptions proposed for the model in a typical human cerebral cortex, allowing the continuation of the model into the gray matter. For the entire pial network, vessel diameters range from 2100 µm for the larger vessels, down to 26 µm for the pre-arteriolar network. When $\gamma = 3.5$, the diameters of terminal vessels fall between 50 µm and 120 µm, a value too large in contrast with the assumed blood vessel density, and therefore not suitable for the model. This could be the case of the combination of these two models permitting better modeling of the tissue. Figure 43 shows the distribution of diameters for both values of gamma.

5.2.3 Distribution of lumen area

The lumen area per diameter of the network was evaluated, and a histogram with intervals of 2 µm per bin is presented in figure 44 and 45. The distribution presented an exponential decay, and when logarithmic scale is applied, this decay is linear.

All three networks presented similar decays for the distribution, with values of -0.0035, -0.0031, -0.0034 log(µm²) per µm when $\gamma = 3.0$, and -0.0021, -0.0010, -0.0021 log(µm²) per µm when $\gamma = 3.5$ respectively (ACA, MCA, PCA).

Figure 43 – Distribution of blood vessel diameters in the pial network for $\gamma = 3.0$ (left panel) and 3.5 (right panel).
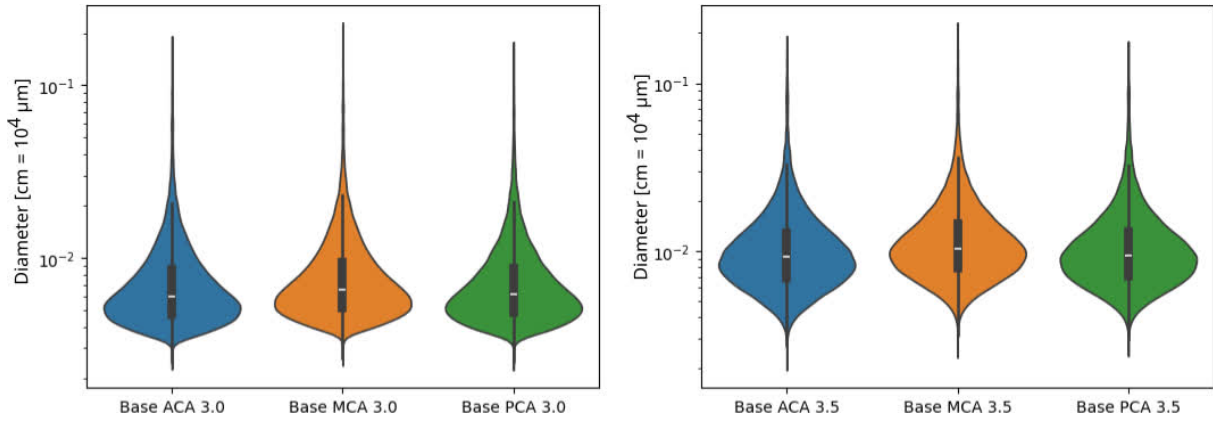
Note: Blue: ACA; orange: MCA; green: PCA.

Figure 44 – Distribution of lumen area by vessel diameter for $\gamma = 3.0$ in linear scale (left panel) and logarithmic scale (right panel).
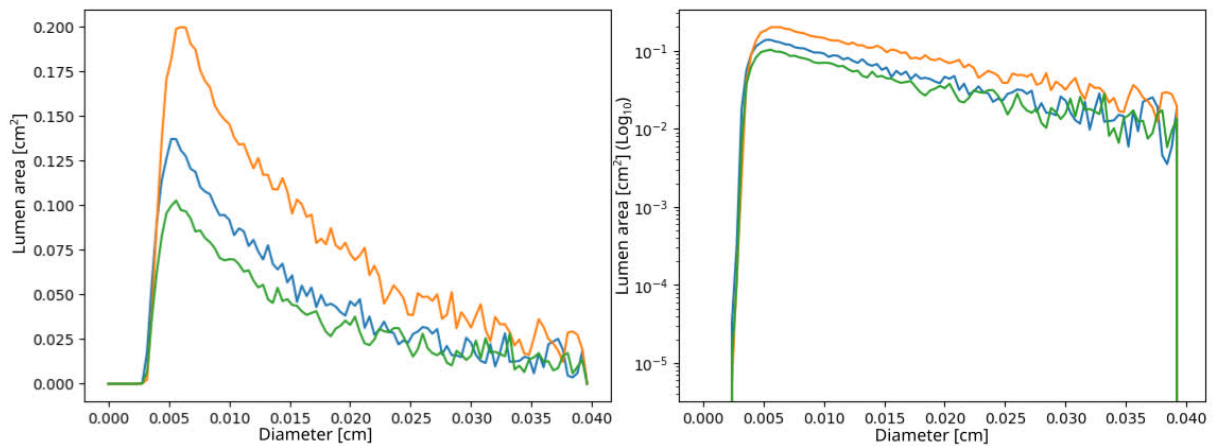
Note: Blue: ACA; orange: MCA; green: PCA.

Figure 45 – Distribution of lumen area by vessel diameter for $\gamma = 3.5$ in linear scale (left panel) and logarithmic scale (right panel).
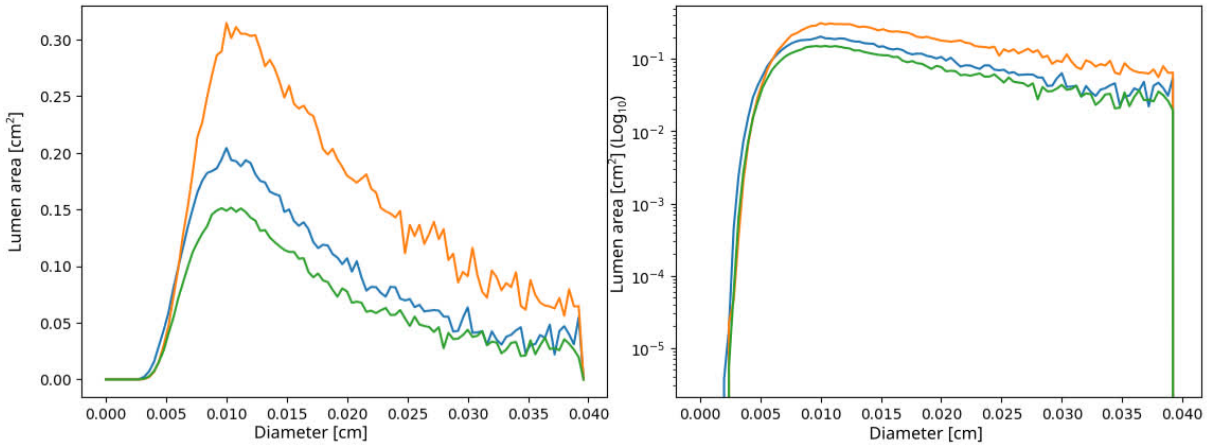
Note: Blue: ACA; orange: MCA; green: PCA.

5.2.4   Distribution of pressure in the network

The distribution of pressure is compared to expected values. In (LINNINGER et al., 2013) the authors report that small pial vessels (corresponding to pial terminals in this work), feature an average pressure between 60 mmHg and 65 mmHg, just before the penetrating arterioles. In (LIPOWSKY, 2005), arterioles of 50 µm in diameter resulted in pressure values between 75 mmHg and 60 mmHg. (KELLY; ROTHWELL, 2020) shows a plateau with arterial pressures ranging from 50 mmHg to 150 mmHg when the blood flow is 50 mL/100g/min.

In (BLANCO; MÜLLER; SPENCE, 2017), the authors cite that the posterior parietal branch of middle cerebral artery with 1 039 µm in diameter presents 85 mmHg for systolic and 54 mmHg for diastolic cases. Branching arterioles between 190 µm and 210 µm present 66 mmHg and 42 mmHg, and arterioles between 30 µm and 50 µm between 59 mmHg and 38 mmHg for systolic and diastolic pressures, respectively.

(SHIMA et al., 1988) and (MATANO et al., 2016) mention that arterioles with anastomoses may present the mean arterial pressure in the MCA ranging from 80 mmHg to 20 mmHg, most commonly 60 mmHg. (BAUMBACH; SIEMS; HEISTAD, 1991) cites the mean arteriolar pressure in the pial surface of rats between 63 mmHg and 73 mmHg, for arterioles between 50 µm and 63 µm in diameter.

Figure 46 presents the distribution of steady-state pressure field for all vessels, and for each cerebral territory in the pial network, after equalizing the inlet vessel to 80 mmHg, which a reasonable value of the blood pressure right after the Circle of Willis. The cumulative distribution of pressures is present in figure 47.

Figure 46 – Distribution of pressure along pial blood vessels for $\gamma = 3.0$ and 3.5.
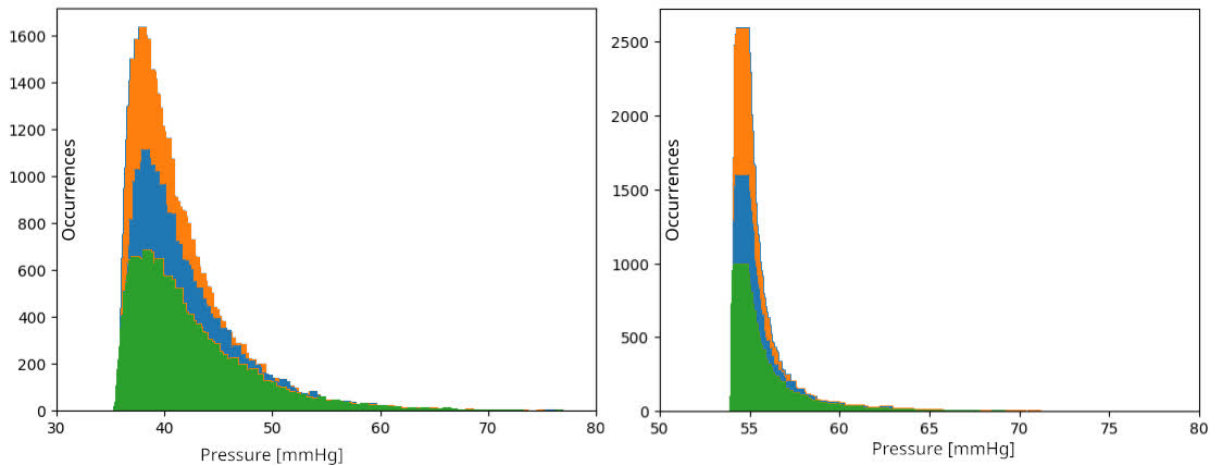
Note: Distribution of steady-state pressure when the inlet is at 80 mmHg of pressure. Blue: ACA; orange: MCA; green: PCA. Left: $\gamma = 3.0$, right: $\gamma = 3.5$.

Figure 47 – Cumulative distribution of pressure values along pial blood vessels for $\gamma = 3.0$ and 3.5.
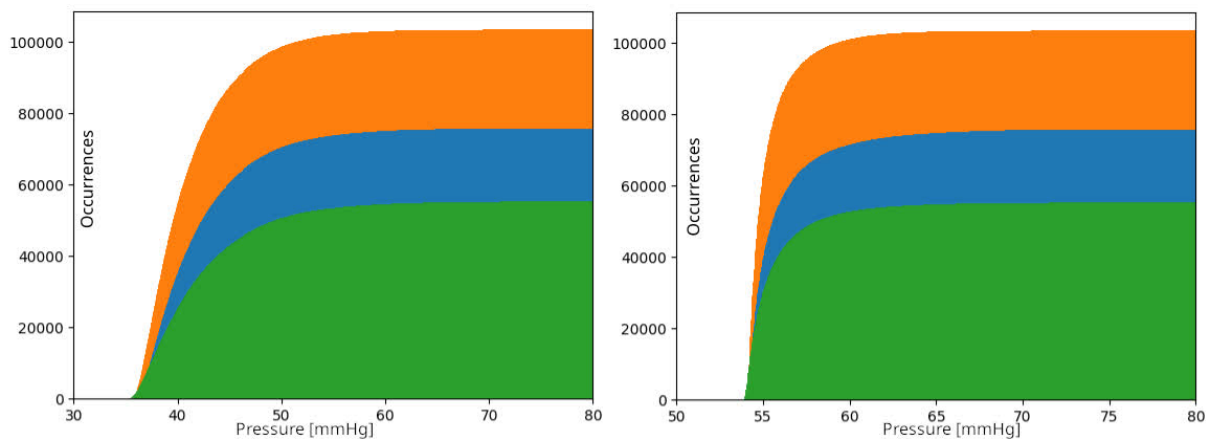
Note: Distribution of steady-state pressure when the inlet is at 80 mmHg of pressure. Blue: ACA; orange: MCA; green: PCA. Left: $\gamma = 3.0$, right: $\gamma = 3.5$.

After reaching the desired number of terminals per mm², the case for $\gamma = 3.0$ is more agreeable with the expected values of pressure for the terminal vessels. When the inlet is fixed at 80 mmHg, the terminal vessels in the pial network present a steady-state pressure distribution around 40 mmHg. When the inlet is fixed at 100 mmHg, the penetrating arterioles fall in the range of 60 mmHg, agreeing with the literature presented. That is, the steady-state pressure drop between the inlet at the circle of Willis and the terminals for penetrating arterioles is around 40 mmHg. Meanwhile, when $\gamma = 3.5$, the pressure distribution is more narrow, resulting in higher values of pressure for the penetrating vessels, not representing the expected values. In this case, the pressure drop is around 25 mmHg. Therefore, the value of $\gamma = 3.5$ does not contribute to a network with the desired qualities, even if the literature presents values slightly above 3.0 (CASSOT et al., 2010).

5.2.5 Pressure equalization across territories

One observation found is that the resulting networks for each territory have their pressure distribution displaced in each region. This is due to small variations under 10% in the inlet diameter from the ADAN model (BLANCO et al., 2015), according to values found in the anatomical literature, and how these values are related to the flow rates prescribed at each vessel in the ADAN model. A subtle lack of balance between vessel diameters and inlet flow rate is propagated to the fourth power when calculating the resistance, and greatly influences the pressure drop in the network by a shift of up to 20 mmHg in the terminal vessels. The probable cause for this imbalance is the variation between the mean inlet flow rate in the ADAN model and the patient-specific volumetric geometry of the cerebrum.

As seen in chapter 3, the pressure drop Δp_i for a vessel with resistance R_i and flow Q_i is given by

$$\Delta p_i = Q_i R_i, \tag{5.5}$$

and, this time as a function of the length l_i diameter D_i,

$$R_i = \frac{128\eta(D_i)l_i}{\pi D_i^4}. \tag{5.6}$$

While the viscosity $\eta(D_i)$ of blood in the network is non-linear, a change of 10% is low enough to assume quasi-linear behavior as seen by the Fahraeus-Lindqvist effect (FÅHRÆUS; LINDQVIST, 1931). Figure 48 presents the original distributions, as opposed to the equalized distributions reported in figure 46.

To solve this lack of balance among the pressure field in the territories, a small correction is done by resizing the root vessel and the tree diameters by a small factor, such that the modified tree results in a more consistent histogram of pressure among the three territories. The MCA network was chosen as the base comparison, and both the ACA

Figure 48 – Distribution of pressure along pial blood vessels before equalization.
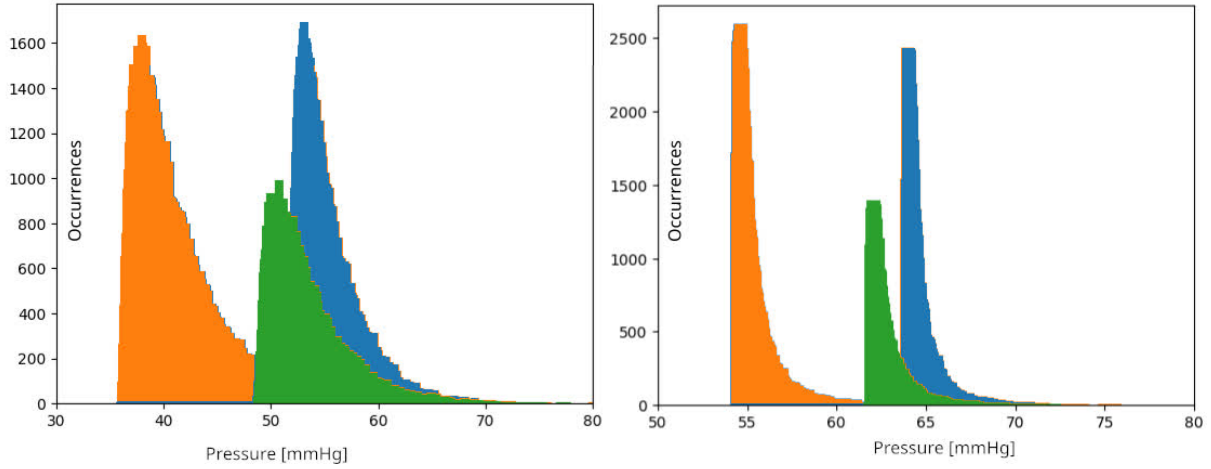
Note: Blue: ACA; orange: MCA; green: PCA. Left: $\gamma = 3.0$, right: $\gamma = 3.5$

and PCA networks had their vessel diameters updated, to reflect the same distribution of pressure in the MCA territory. The comparison aims to encounter the most accurate scale factor for each territory that results in a similar distribution of pressure.

The goal is to find the scale factor to the ACA and PCA networks, such that results in the lowest error between, either the ACA or the PCA distribution, and the MCA distribution, i.e., find the scale factor that removes the gap between distributions (see figure 48). The procedure is done as follows:

a) resize the diameters in the ACA and PCA territories from 1.00 down to 0.80 in steps of 0.05;

b) for each step, update the trees, and calculate the pressure distributions in all territories to have an inlet pressure of 80 mmHg, a typical value of pressure in the Circle of Willis;

c) create a histogram of values of pressure, and for each bin, count the number of vessels that fall in that bin;

d) calculate the distance of ACA and distributions with respect to the MCA distribution via the sum of the quadratic error of the cells for each bin;

e) continue with the next scale factor;

f) the scale factor with lowest error is chosen as the best.

The quadratic error is assumed as

$$e = \sum_{i=1}^{N} (\text{Bin}_{\text{Ref } i} - \text{Bin}_i)^2, \tag{5.7}$$

where $\text{Bin}_{\text{Ref } i}$ is the number of occurrences in the MCA territory, and Bin_i is for the ACA/PCA territories, for the $N = 1000$ bins between 0 and 100 mmHg. The error plot of the scale factors are present in figure 49.

Figure 49 – Quadratic error for different scale factors of the network.
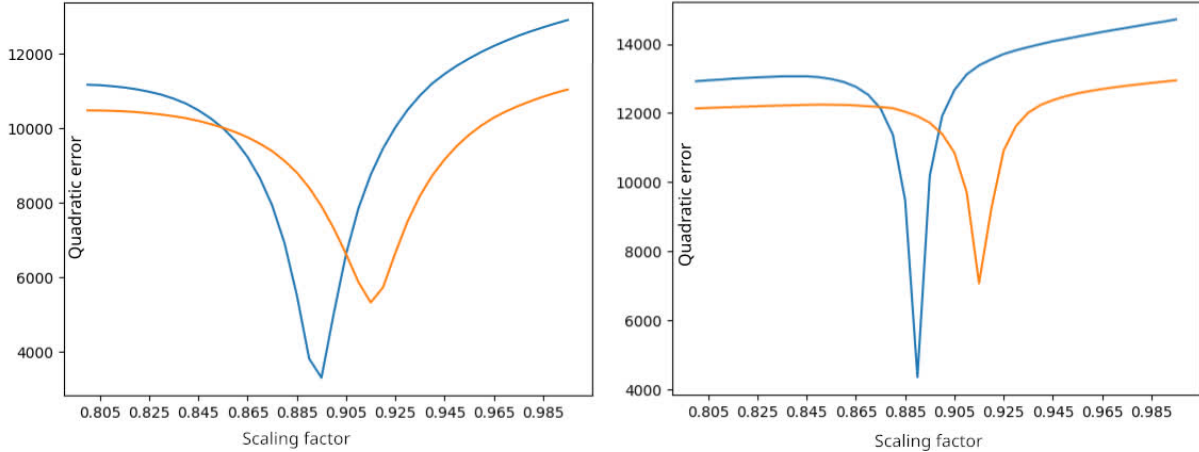
Note: Blue: ACA; orange: PCA. Left: $\gamma = 3.0$, right: $\gamma = 3.5$

The optimal scale factors that yield the best balance between ACA and MCA, and between PCA and MCA are reported in table 12. These factors are applied to the ACA and PCA networks correspondingly, and these equalized networks are the ones used in the gray matter generation.

Table 12 – Equalization factors for the pial territories.

Territory	ACA	MCA	PCA
Scale factor ($\gamma = 3.0$)	0.895	1.000	0.915
Scale factor ($\gamma = 3.5$)	0.890	1.000	0.915

5.2.6 Correlation between pressure and diameter

The correlation between the diameters and the pressure of the network was analyzed for the pial network and each territory. Figures 50 and 51 show this correlation. The trend follows a linear path until reaching the lowest values of pressure, reaching these values quicker when $\gamma = 3.5$ compared to $\gamma = 3.0$. We can observe that vessels fall above the linear trend, that is, low values of pressure are only present in smaller diameters, while the opposite is not true since smaller vessels may present high pressure.

Figure 50 – Correlation between pressure and diameter for the pial network when $\gamma = 3.0$.
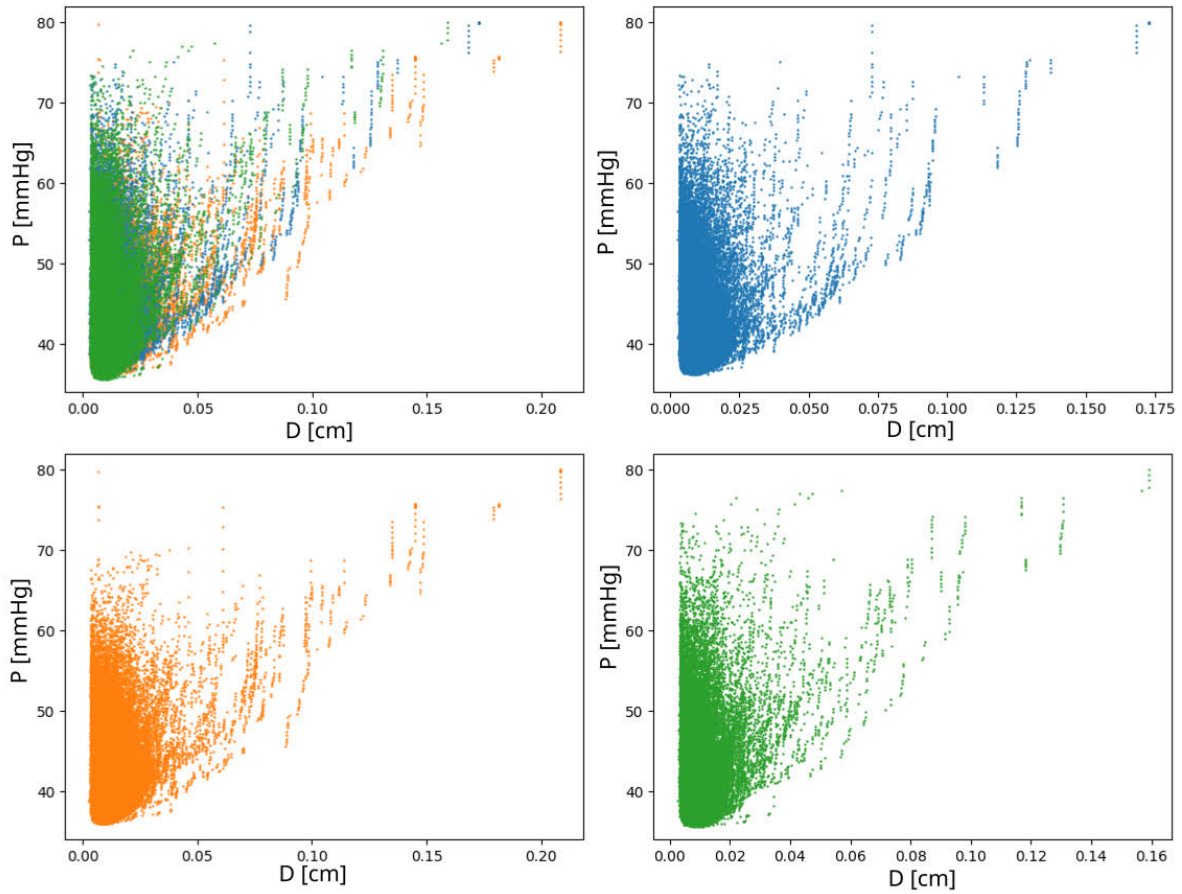
Note: The steady-state pressure is analyzed when the inlet pressure is 80 mmHg. Blue: ACA; orange: MCA; green: PCA.

5.3 Generation of the gray matter vascular network

The vascularization of the gray matter follows the methodology proposed in chapter 4. For the generation of the gray matter vascular network, two steps are fudamental:

a) generation of the descending arterioles from the pial domain into the gray matter domain;

b) generation of the gray matter deep network itself.

The value of the gamma exponent for the gray matter vascularization was chosen to be $\gamma = 3.0$, continuing the value of the pial network chosen as the best, and the networks with $\gamma = 3.5$ were not continued. Results with $\gamma = 3.0$ from previous stage present a more consistent result with reality (DUVERNOY; DELON; VANNSON, 1981), and bifurcating vessels into the gray matter fall within the correct range. For $\gamma = 3.5$, the distribution of diameters does not correspond to the values in the literature. It is known, however, that

Figure 51 – Correlation between pressure and diameter for the pial network when $\gamma = 3.5$.
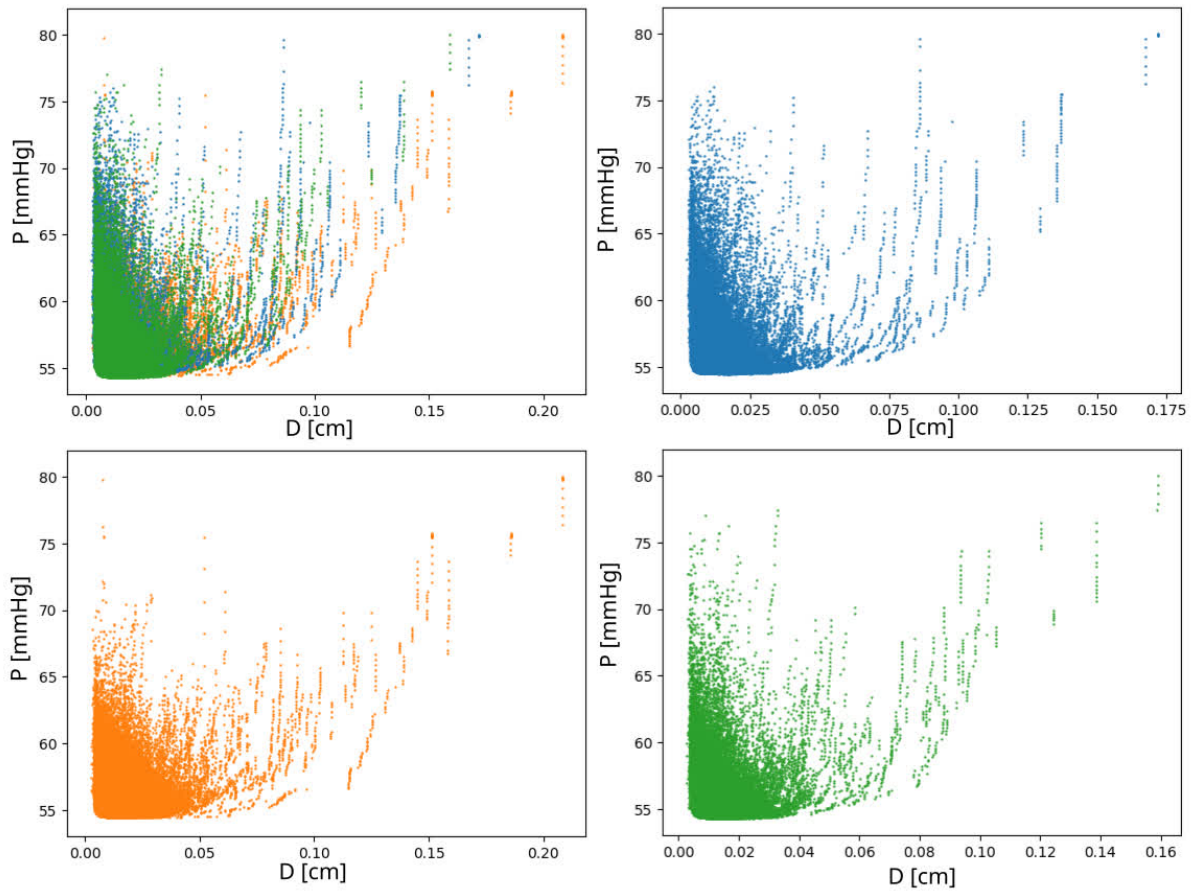
Note: The steady-state pressure is analyzed when the inlet pressure is 80 mmHg. Blue: ACA; orange: MCA; green: PCA.

the gray matter has different values of this parameter throughout levels of depth in the cortex (CASSOT et al., 2010), but for this work it is considered uniform.

5.3.1 Generation of descending arterioles

This stage consists of penetrating vessels continuing from the pial network into the gray matter domain. The quantity of descending arterioles generated is obtained from the quantity of terminal vessels in the pial network. It is important to reiterate that two vessels are generated from each terminal, one from the endpoint, and another from the midpoint of the terminal. However, the ratio between the gray matter volume to surface area for each territory is almost proportional, meaning the assumption of 1 penetrating arteriole per mm², or 2 when considering the possibility of extending to long and short penetrating vessels (HARTUNG et al., 2021), is quasi-proportional to the volume of the territories.

Following the methodology in chapter 4, each territory has its penetrating vessels generated at once. As mentioned in chapter 3, the characteristic length l_{min} relates to the spatial generation of blood vessels, and was carried throughout the generation of the pial network to minimize deformations. However, this parameter was not carried to the gray matter domain due to this step not making use of the CCO minimization.

The quantity of penetrating arterioles generated is 225 422 vessels, 73 053 for the ACA, 101 133 for the MCA, and 51 216 for the PCA. For the surface area in the gray matter of 975 cm² for the three territories, this results in 2.36 penetrating segments per mm². This accounts for both long and short penetrating vessels (HARTUNG et al., 2021). Figure 52 shows the penetrating vessels generated for a portion of the cerebral cortex.

Figure 52 – Penetrating vessels generated for the gray matter.
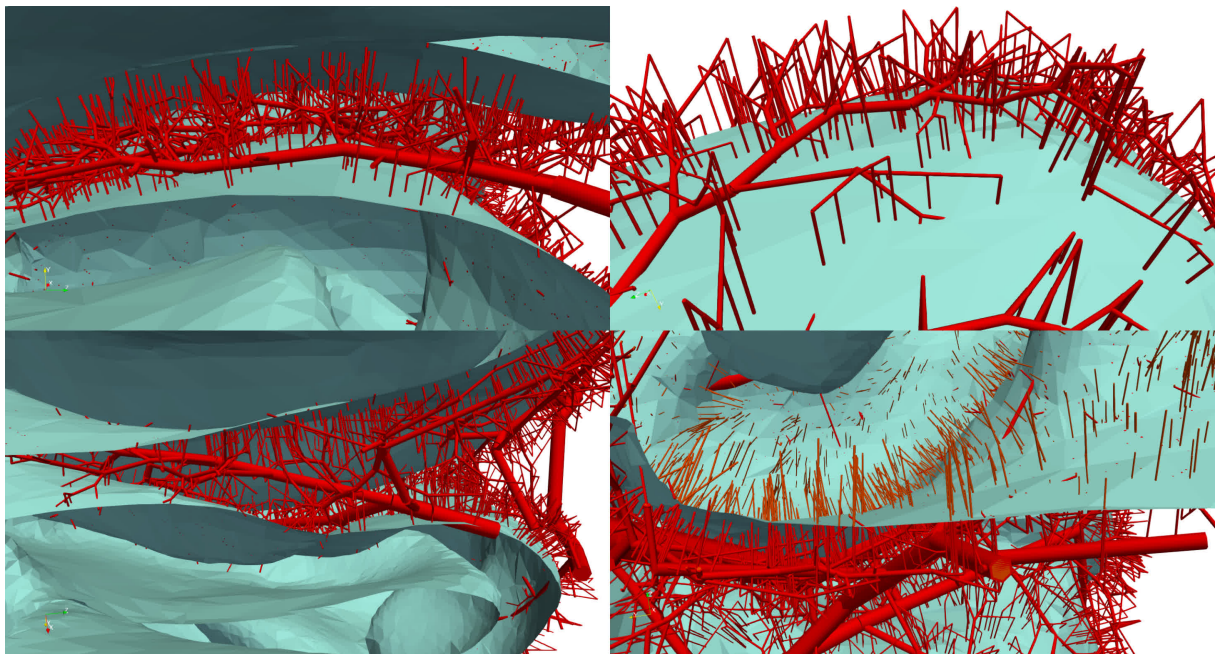
Note: Penetrating vessels (red) generated from the pial network into the gray matter (cyan). Top left: penetrating vessels for the parietal ACA territory; top right: portion of the occipital PCA penetrating vessels; bottom left: parietal MCA penetrating vessels; bottom right: penetrating vessels (red) and virtual trunk segments (orange) in parietal ACA territory.

5.3.2 Generation of the sub-tree population

The gray matter microvascular arborizations, also called sub-trees, were presented in chapter 4. These structures have their functional cost defined as sprouting from equation 3.15 adapted for this situation. As mentioned in chapter 4, a population of 100 different sub-trees was constructed by altering the generation seed. Generation was carried

out in hexagonal domains, and each sub-tree contains 51 blood vessel terminals, or 101 segments. The generation uses again the value of $\gamma = 3.0$ in this stage, continuing the pial network with the best exponent, knowing that (CASSOT et al., 2010) mentions values of $\gamma = 2.8$ for the Murray's exponent.

Figure 34 in chapter 4 presented a small sample of 10 arborizations constructed via this method. The parameters for the generation of the sub-tree population are presented in table 13.

Table 13 – Parameters used for generation of the microvascular arborizations (sub-trees) in the gray matter.

Parameter	Value
Gamma exponent	3.0
Symmetry factor	0.0
Perfusion area factor	0.5
l_{min} reduction factor	0.9
Neighborhood factor	2.0
Segments per bifurcation	7
Number of terminals	51
Functional type	Sprouting
Sprouting parameters	$C_v = 1.0 \cdot 10^3$, $C_p = 0.5$, $C_d = 1.0$
Vessel type	Distribution
Minimum bifurcation angle	$0\,\mathrm{deg}$
Minimum plane angle	$0\,\mathrm{deg}$

The perfusion factor was chosen 0.5 due to the ratio between the diameter and length of the hexagon relating to the characteristic length of the domain, and neighborhood was chosen to give result 1.0 when multiplying both parameters. The sprouting functional was used to prioritize bifurcations from smaller vessels and create shorter segments.

Generation of the sub-tree structures can be done in two steps, the second avoiding the main branch, however, the population was constructed in a single stage, with 51 terminals, or 101 segments. Variation of generation seed permits the construction of multiple structures with the same parameters chosen to mimic structures found in (CASSOT et al., 2010; LAUWERS et al., 2008). Figure 53 shows a small portion of the gray matter network with appended sub-tree structures in the network within the MCA parietal region.

5.4 The complete network

5.4.1 General characteristics

The number of the terminals in the final network results from the multiplication of the number of terminals in the pial network by a huge factor. Each pial terminal vessel bifurcates into two penetrating arterioles, and each arteriole gives rise to a sub-tree with 101 segments. The total number of terminals in the network is presented in table 14.

Figure 53 – Small region with appended gray matter structures, MCA parietal territory.
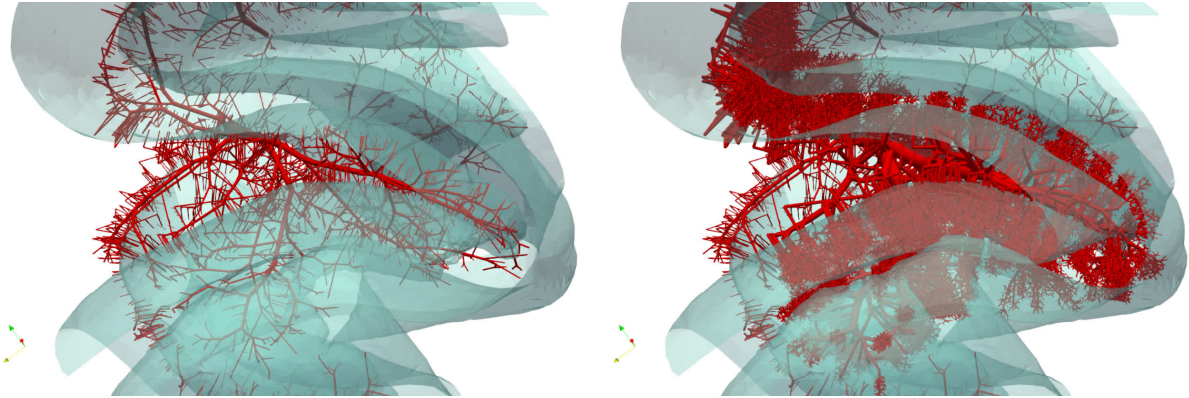
Note: Left: region before the appending of structures; right: same region with the appending of 100 cortical microvascular arborizations.

Table 14 – Number of terminals and segments in the complete network.

Quantity	ACA	MCA	PCA	Hemisphere	Factor
Terminals (pial network)	37 803	51 595	27 579	116 977	—
Segments (pial network)	75 700	103 048	55 236	233 984	—
Terminals (full network)	3 726 985	5 158 814	2 613 991	11 499 790	x 98.3
Segments (full network)	7 563 638	10 469 543	5 304 880	23 338 061	x 99.7
Percentage	32%	45%	23%	100%	

Therefore, the number of terminal vessels is increased, roughly, by a factor of 100. The vascular morphology generated in this way is in agreement with (Reina-De La Torre; Rodriguez-Baeza; Sahuquillo-Barris, 1998) and (CASSOT et al., 2006). Figures 54 and 55 show slices of the complete gray matter network for several regions of the brain, considering an inlet pressure in the Circle of Willis of 100 mmHg. Note that the penetrating vessels are always close to the range of 50 µm regardless of the region depicted. The pressure, however, varies for each region. Figure 55 shows vessels with a lower value of pressure in the frontal and occipital lobes of the MCA territory when compared to the values in the temporal lobe (MCA), or in temporal lobe for the PCA (figure 54). Vessels in the parietal lobe for the ACA presents the value closer to 50 mmHg in figure 54. This is an interesting finding from the networks that the region with the lowest pressure happens to be between the MCA and the ACA territories, where the distance from the Circle of Willis is greater.

The complete network presents 23 338 061 blood vessels, 23 104 077 being in the gray matter. This gives a density of 80.22 blood vessel segments per mm³ in the gray matter, or 48.3 vessels per mm³ if considering the average with the pial network. The full network has a total vessel length of 4 591 863.0 mm, or 4.59 km, along the three territories.

The total volume of the network is 3889.79 mm³, and 1193 mm³ in the gray matter.

Figure 54 – Views of the complete gray matter network in regions of the ACA and PCA territories.
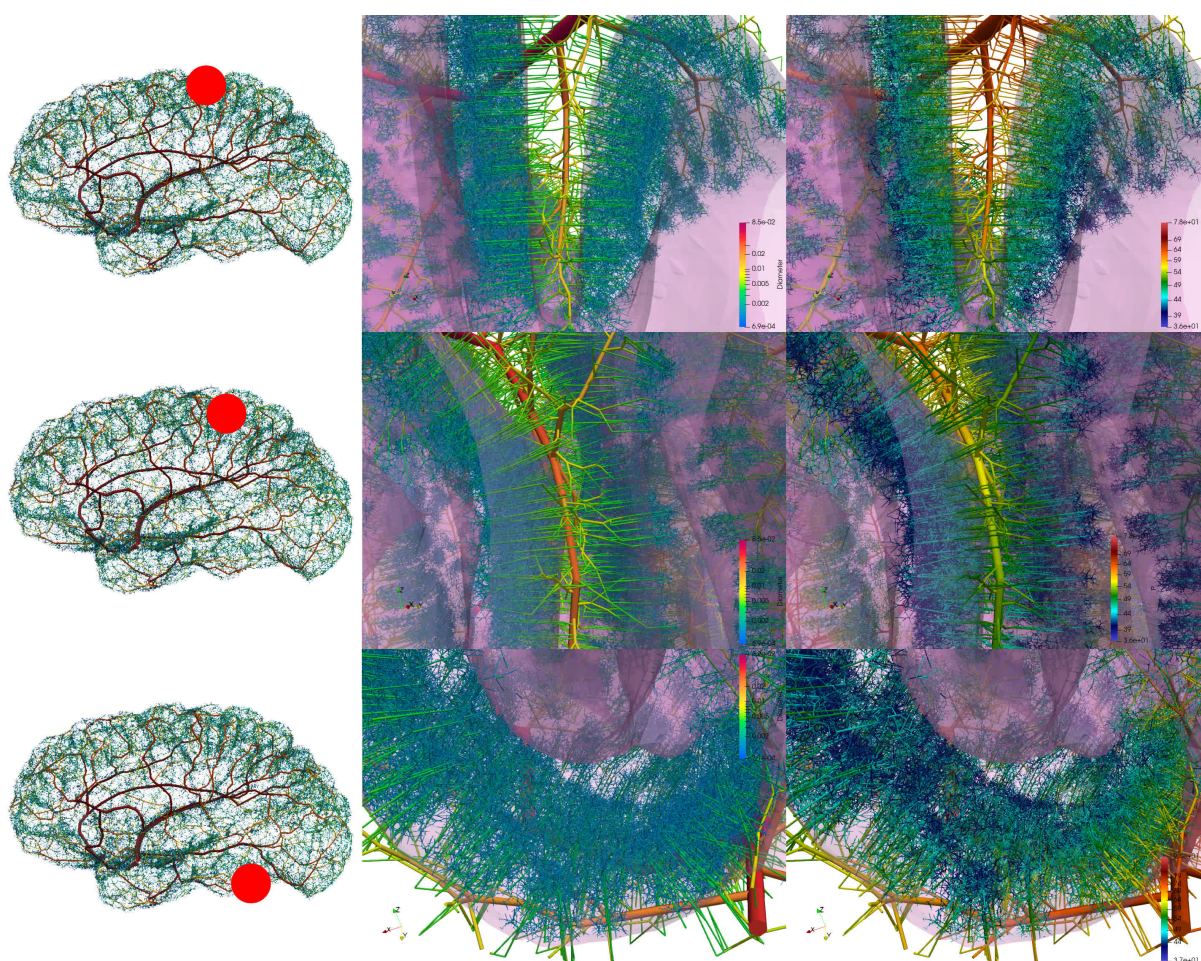
Note: Region (lobe), diameters and pressure respectively for each cerebral region. Top row: ACA territory, parietal region. Middle row: ACA territory, parietal region. Bottom row: PCA territory, temporal region. In all three pictures, penetrating vessels are in the range of 50 µm in diameter (green tones), and pressure in the penetrating segments varies around 50 mmHg.

Figure 55 – Views of the complete gray matter network in regions of the MCA territory.
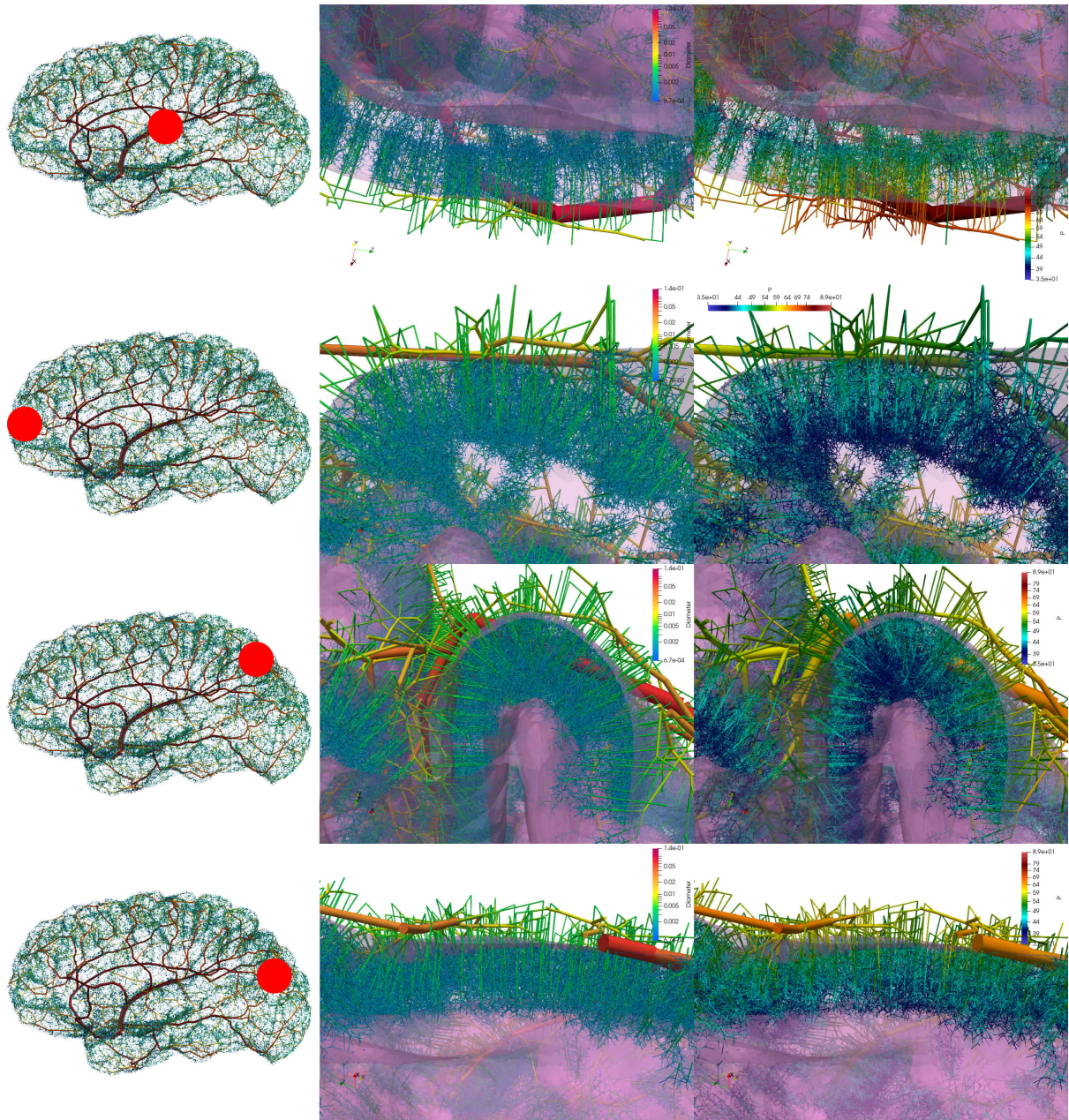
Note: Region (lobe), diameters and pressure respectively for the MCA region across the hemisphere. Top row: Temporal lobe. Second row: Frontal lobe. Third row: Parietal lobe. Bottom row: Occipital lobe. All penetrating vessels agree in diameter around 50 µm (green tones). Pressure in the frontal and occipital/back parietal regions are significantly lower than the temporal lobe.

The fraction of vascular volume is 0.80% for the entire network, and 0.41% for the gray matter vessels. These values are too low, below the values in (LINNINGER et al., 2013), which may be due to the small quantity of blood vessels in the penetrating structures, and, mainly, the lack of venous and capillary structures. Table 15 presents the results of the complete network, and the gray matter domain.

Table 15 – Resulting characteristics in the complete network, and in the gray matter section.

Characteristic	ACA	MCA	PCA	Hemisphere
Complete network				
Vessel density [qty/mm³]	48.9	48.1	47.7	48.3
Network length [mm]	1 481 239	2 067 142	1 043 483	4 591 863
Vascular volume [mm³]	1155.07	1928.25	806.47	3889.79
Fraction of volume	0.75%	0.89%	0.73%	0.80%
Gray matter vessels				
Vessel density [qty/mm³]	81.2	79.9	79.2	80.22
Network length [mm]	1 425 894	1 991 896	1 002 971	4 420 760
Vascular volume [mm³]	352.16	570.71	270.23	1193.10
Fraction of volume	0.38%	0.44%	0.41%	0.41%

5.4.2 Distribution of diameters

The distribution of diameters in the complete network is presented below in figure 56, in comparison with the pial network. The values of the distribution are present in table 16.

Figure 56 – Distribution of diameters for the pial network (left panel) and gray matter network (right panel).
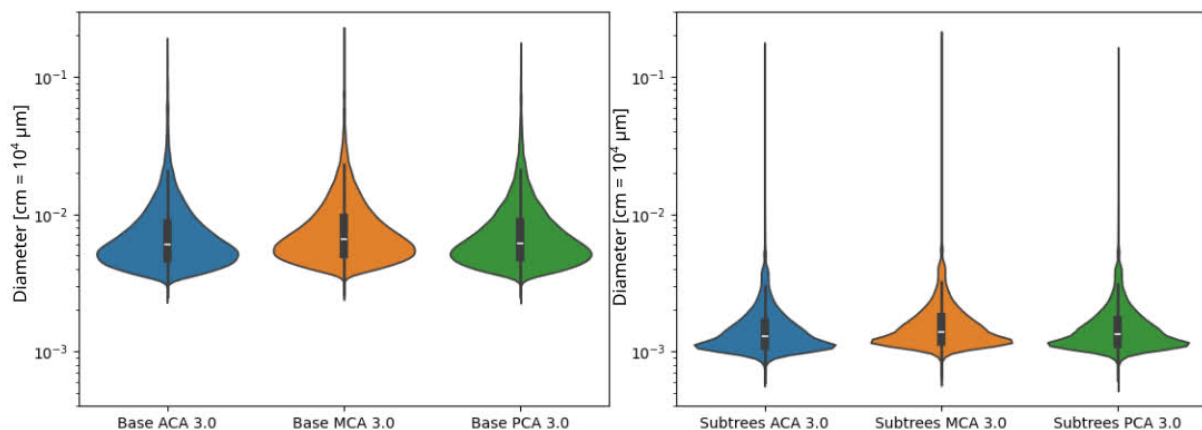
Note: Blue: ACA; orange: MCA; green: PCA. Region with 50 µm in diameter for the descending arterioles is seen in the full network, where accumulation occurs due to the non-bifurcating nature of the algorithm

Table 16 – Comparison of distribution of diameters for pial and gray matter network.

Diameters	ACA	MCA	PCA
Pial Network			
Median [µm]	60.0	65.7	61.3
Inter-quartile range [µm]	47.2, 85.5	51.5, 93.8	48.4, 87.2
Gray matter Network			
Median [µm]	12.9	14.0	13.4
Inter-quartile range [µm]	11.0, 16.7	11.9, 18.1	11.4, 17.3

As we can see, the distributions contain similar values of diameters, and the plot shows that most distributions end the pial network at between 50 µm and 60 µm. Aditionally, the diameters found in the gray network reach pre-capillary levels at 10 µm in diameter. The variation in the shape of the distribution when appending the sub-trees is a result of the change in the generation criterion, where CCO was not used in the interface between the pial and gray matter networks.

5.4.3 Lumen area by diameter

The accumulated lumen area, or vascular area, by vessel diameter is presented in figure 57. Bins are of 2 µm, and the graph shows a much steeper decline for values of diameter, having average values of -0.0052, -0.0051, and -0.0051 log(µm²) per µm, around 51% steeper. This sharper decline is an indication of the effect the appending of the sub-trees may have in the properties of the network, since the two intervals of diameter present two very characteristic inclinations, and a discontinuity in between. This reflects the two methods of generation, CCO and geometrical projection, when linked using the penetrating arterioles method.

5.4.4 Distribution of pressure in the full network

After generating the full networks, the distribution of pressure in the three territories is evaluated in figure 58. The values of the distributions are present in table 17. The three networks present similar distributions of pressure, but with displaced values to lower values, due to the smaller vessels presenting a large resistance to the blood flow (GOULD et al., 2017). The value reached in the gray matter network of 25 mmHg is around the expected value in pre-capillary levels (GOULD et al., 2017; HARTUNG et al., 2018).

5.4.5 Correlation between pressure and diameter

The correlation between pressure and diameters is shown in figure 59. The linear trend for the pial vessels is still visible, but for lower vessels in the gray matter this

Figure 57 – Distribution of lumen area by vessel diameter for the pial network (left panel) and the gray matter network (right panel).
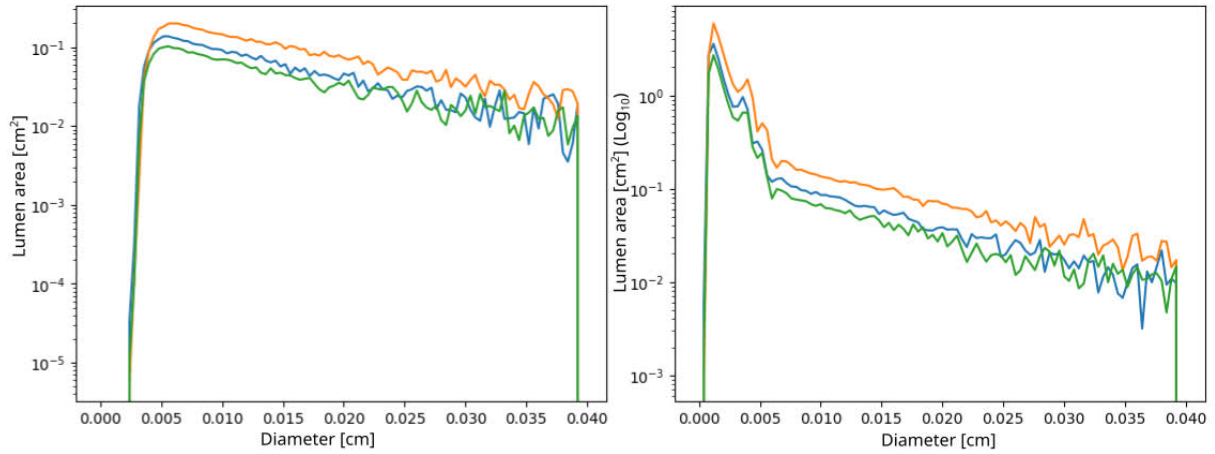
Note: Blue: ACA; orange: MCA; green: PCA.

Figure 58 – Distribution of pressure for the pial network and gray matter network.
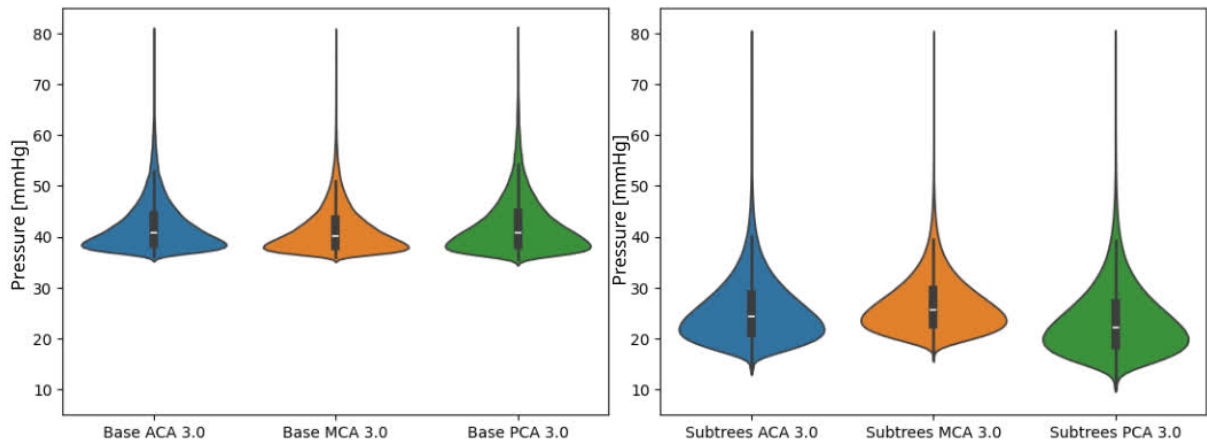
Note: Blue: ACA; orange: MCA; green: PCA. Left is pial, and right is gray matter.

Table 17 – Comparison of distribution of pressure for pial and gray matter network.

Pressure	ACA	MCA	PCA
Pial Network			
Median [mmHg]	40.7	40.1	40.8
Inter-quartile range [mmHg]	38.6, 44.3	38.2, 43.3	38.4, 44.7
Gray matter Network			
Median [mmHg]	24.3	25.6	22.2
Inter-quartile range [mmHg]	21.0, 28.6	22.7, 29.4	18.7, 26.9

trend occurs sharply when varying the diameter. This displays a different behavior in the correlation between pial and gray matter networks.

Figure 59 – Correlation between pressure and diameter for the gray matter network.
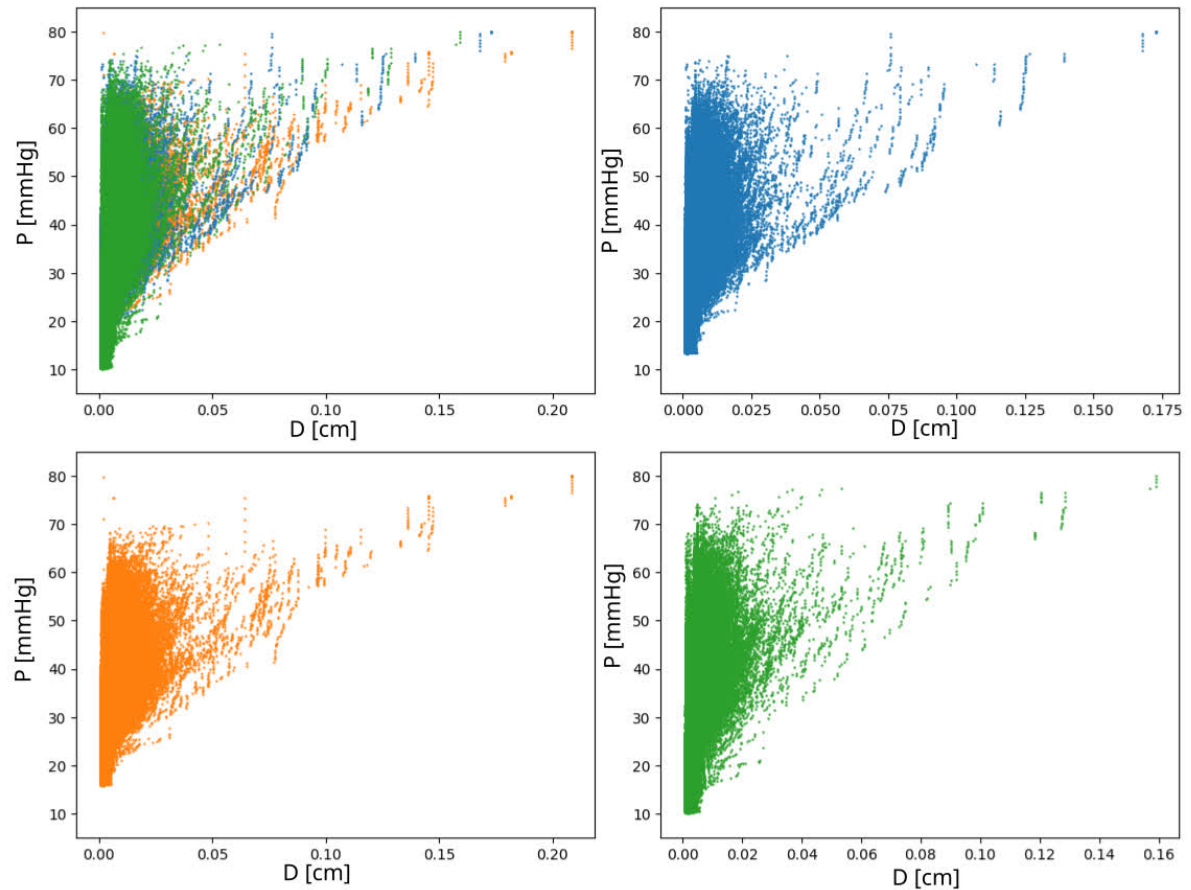
Note: The steady-state pressure is analyzed when the inlet pressure is 80 mmHg. Blue: ACA; orange: MCA; green: PCA.

5.4.6 Summary of generation

In summary, the full vascular network comprises the pial domain and the gray matter domain, including the three vascular territories of the left cerebral hemisphere. The pial network contains three stages, two sequential, and one parallelized generation that is merged afterwards. The gray matter domain contains two stages, the penetrating vessels, and the gray matter arborizations, along with another stage for the pre-generation of sub-trees.

Over the pial surface, diameters vary between 2100 µm and 26 µm, with terminals between 50 µm and 60 µm, and the variation of steady-state pressure from the circle of Willis towards the terminals is between 30 mmHg and 40 mmHg. In the gray matter,

vessel diameters reach values down to 12 µm, just before the creation of the capillary network. When the gray matter arborizations are appended to the gray matter network, the steady-state pressure reduces by 50 mmHg from the circle of Willis until the penetrating vessels, and it drops by around 65 mmHg and 70 mmHg at the smaller vessels in the gray matter vasculature when compared to the inlet. The distribution of blood pressure in the network suggests that the regions further from the circle of Willis present the lower values of blood pressure. The complete network reaches the tens of millions of blood vessels, completely beyond the current state of the art in the field.

The times of execution for each step of the network are the following:

a) stage 1 of the pial network takes 20 minutes;

b) stage 2 of the pial network takes 2 hours;

c) stage 3 of the pial network takes between 3 and 12 hours for each one of the 21 partitions, with an average time of 9 hours;

d) generation of penetrating arterioles takes 2 hours in total for all 3 territories;

e) generation of the population of 100 subtrees takes 5 minutes;

f) appending of subtrees range from 20 minutes (PCA, ACA) up to 50 minutes (MCA).

6 Conclusions

6.1 Major contributions

This work proposed a methodology and a strategy to automatically generate highly-detailed blood vessel networks *in silico* in a portion of the human brain. The scope begins with patient-specific geometry extracted from medical images in order to define the domain to be vascularized, the expansion of an existing hemodynamic model used as initial network, and the extension of an optimization algorithm to better suit the needs of the specific anatomical features displayed by the cerebral cortex. The resulting vascular network can be used to perform numerical simulations across the left hemisphere of the cerebral cortex, and could be repeated to obtain both hemispheres. These three, geometry, model, and algorithm, when combined, provide a proper ground for the study of complex hemodynamic mechanisms that take place in normal and pathological conditions and in a patient-generic setting, as well as in patient-specific scenarios. As a consequence, this allows the investigation of blood flow and blood pressure in the brain, and allows to shed light on the interactions between the systemic circulatory scale, and local cerebral hemodynamics. Moreover, the proposed tools and the resulting model in this work are a potential path which may boost the study of neurovascular coupling in the future. That is, the mechanisms thorugh which where neural activity and hemodynamics are connected. The availability of such highly-detailed, patient-specific models makes it possible to perform refined *in silico* experiments, empowering the capabilities of modern individualized medicine.

The generated network for the pial domain includes over 230 000 blood vessels, reaching a network length of over 170 m, and a blood volume fraction of 1.48%. Blood vessels range from 2000 µm down to the scale of penetrating arterioles at 50 µm. The pressure drop from the Circle of Willis down to the penetrating arterioles is around 50 mmHg. In turn, the gray matter network reaches the scale of 12 µm in diameter, and contains over 23 million blood vessels. The total length of this network is over 4.5 km in extension. By analyzing the pressure field predicted by the model, it is possible to identify regions at the interface between the ACA and MCA territories where the pressure features lower values compared to other regions around the cortex, which is related to the fact that these places are located further away from the corresponding inlet points. This tells us about the heterogeneities of the blood pressure around the cortical domain, something that deserves further investigation.

One of the main specific contributions of this work is the construction of a highly refined vascular network of the human cerebral cortex, with unprecedented level of detail, that encompasses both large cerebral arteries, through the vessels of the pial surface,

and down to the scale of smaller vascular arterioles in the ramifications of the gray matter perforators. The present model, or a submodel from it, can be coupled with existing blood flow models of the entire cardiovascular system, to perform pulsatile blood flow simulations using one-dimensional modeling tools, and get a better picture of the hemodynamics across the entire cardiac cycle. This can help in giving insight about pressure and flow pulsatility and heterogeneities across the entire cerebral vasculature, including regions suffering from hypoperfusion, and regions whose low blood pressure may affect the metabolism of the neuroglial cells. The novel approach proposes a strategy for vascularization and simulation of the brain hemodynamics, aiming state-of-the-art knowledge of microcirculation under normal and pathological systemic conditions, laying the foundation to investigate cerebrovascular anomalies and clarify connections between brain function and hemodynamic phenomena, in normal and abnormal scenarios. Typical scenarios that benefit from this work can be the assessment of risk of stroke, the investigation of the mechanisms underlying vessel diseases, and other blood flow phenomena involved in the onset and progress of degenerative diseases. The technique in this work can also be more automatized with further development of algorithms or machine learning techniques, particularly in the steps regarding the initial data analysis and projection of the baseline model. Additionally, more powerful MRI scanning techniques could obtain a high-fidelity of the macrovascular characteristics of the patient, and an accurate patient-specific network could be generated, using the arterial vessels as the baseline model of the generation, and obtaining the blood flow from medical exams.

6.2 Limitations of the current approach

One limitation is the scarcity of numerical data to validate that the proposed vascular networks are in agreement with real in-vivo data in terms of the predicted hemodynamic environments. Although structural and qualitative validation can be done with the available data, numerical validation can be further improved. The proposed approach has relied on data reported in the literature about hemodynamic conditions found in the pial circulation, as well as about anatomical data extracted from images of the deepest cerebral vascular structures. The scarcity of data is well-known in the field, and the proposed approach relies on the consistency of the CCO-based approach in reproducing anatomically realistic vascular networks when compared with animal data and post-mortem studies in other vascular territories. An indirect validation could be performed by collecting perfusion maps from MRI scans in real patients, and by comparing these maps with the perfusion as predicted by the model. Although indirect, this is the validation that could be performed with current technologies. However, validation with brain perfusion maps was out of the scope of the present work. Notice, also, that this validation would be in terms of flow rate, while the pressure estimate would still remain

to be validated. Another method to numerically validate the results would consist in evaluating SPECT-CT data to compare the energy balance of an organ given the blood flow, i.e., correlate perfusion and blood vessel density with the energy data extracted from SPECT-CT.

Another limitation of the current work is the lack of collateral vessels in the vascular network built with the proposed methodology. This limitation can be circumvented by following an ad-hoc approach in which collaterals are created based on the proximity of neighboring vessels and the similarity of the diameters of these neighboring vessels. This was out of the scope of the present work, and is being a matter of current research.

As mentioned briefly at the end of chapter 4, the sub-tree structures do not have their collisions checked due to the great number of connections happening at this step. This could be fixed in the future by checking the collisions and changing sub-trees that result in overlapping vessels. The methodology of this algorithm, however, is still to be discussed due to the computational cost required. The distribution of the cortical columns can also be further studied. Stochastic patterns in the generation of this network, i.e. the variation of the random seed input, were not studied. The generation considering these variations could give insight into a distribution of possible arterial networks and their associated probabilities. Oxygen transport was not considered in this model, neither was the autoregulation in different cerebral regions. Also, the physicochemical properties of the medium are not considered in the CCO generation. Capillary blood flow can be studied via the coupling with hybrid models and porous media similar to other works, as mentioned in chapter 1 and 2.

The multiscale approach in this work was not concurrent, i.e. it was not generated for each scale, but instead via a top-down approach, where the vascular network is generated from larger structures down to the coupling with smaller sub-trees at the lower scales. Data from multiple scales were used as a guideline for this generation.

6.3 Scientific publications

Some works were published during the development of this dissertation. An abstract for the *CNMAC 2023* conference, describing the initial steps of the generation in a test domain, and an extended abstract for the *CMBE 2024* international conference, with insight into the simulation of pulsatile blood flow in the pial network, were published:

a) **E.G. Zilves**, G.D.M. Talou, and P.J. Blanco. A vascular model of cerebral arteries generated by constrained constructive optimization. *Proceeding Series of the Brazilian Society of Computational and Applied Mathematics - CNMAC 2023* v. 10 n. 1 (2023) SBMAC.

b) **E.G. Zilves**, G.D.M. Talou, L.O. Müller, and P.J. Blanco. Construction of

(and blood flow simulation in) highly detailed arterial networks in the human cerebral cortex. *Proceeding: 8th International Conference on Computational & Mathematical Biomedical Engineering - CMBE2024* vol.1, June 2024, USA.

Two full-length papers were accepted for publication, one for the *ENEBI 2024* conference, and one for the *CILAMCE 2024* conference. The first paper describes the complete generation of the pial network, while the second paper covers the steps in the generation of the cortical column structures for the gray matter.

a) **E.G. Zilves**, G.D.M. Talou, and P.J. Blanco. Generation of highly-detailed arterial networks in the human cerebral cortex by constrained constructive optimization. *Proceedings of VIII Encontro Nacional de Engenharia Biomecânica - ENEBI* October 2024.

b) **E.G. Zilves**, G.D.M. Talou, L.O. Müller, and P.J. Blanco. Into the gray matter: construction and coupling of multiscale highly-detailed arterial networks in the human cerebral cortex. *Proceedings of the XLV Ibero-Latin-American Congress on Computational Methods in Engineering, ABMEC - CILAMCE 2024* November 2024.

A scientific paper published in the *Stem Cells Translational Medicine* journal, concurrent but unrelated to this work.

a) R.S. Tesch, E.R. Takamori, K. Menezes, R.B.V. Carias, C.L.K. Rebelatto, A.C. Senegaglia, D.R. Daga, L. Fracaro, A.W. Robert, C.B.R. Pinheiro, M.F. Aguiar, P.J. Blanco, **E.G. Zilves**, P.R.S. Brofman, and R. Borojevic. Nasal septum-derived chondroprogenitor cells control mandibular condylar resorption consequent to orthognathic surgery: a clinical trial. *Stem Cells Translational Medicine* v.13, Issue 7, July 2024.

6.4   Final remarks

The study of cerebral hemodynamics enables the understanding of blood flow phenomena in the brain, becoming a tool that complements current technologies to assess the brain perfusion. This work establishes the groundwork for the development of computational models of the circulation in the cerebral cortex, making it possible, in the future, to correlate the hemodynamics phenomena and brain function, under both normal and abnormal conditions. Moreover, this approach can be automated to patient-specific settings, allowing the study of drug delivery, risk of stroke, and mechanisms observed in neurodegenerative diseases that could be linked to the local cerebral environment. This approach is a potential tool for the study of how the blood pressure varies along the cortical brain, and may also fuel research in the field of neurovascular coupling in the future. This kind of tool, enabling the multi-scale analysis of blood flow phenomena in the brain, and

also enabling for patient-specific analyses, will aid to strengthen the physiological and future pathophysiological connections between neurology and cardiovascular function.

Bibliography

AVOLIO, A. P. Multi-branched model of the human arterial system. *Medical & Biological Engineering & Computing*, v. 18, n. 6, p. 709–718, nov. 1980. ISSN 0140-0118, 1741-0444. Cited in page 33.

BAUMBACH, G. L.; HEISTAD, D. D. Cerebral circulation in chronic arterial hypertension. *Hypertension*, v. 12, n. 2, p. 89–95, ago. 1988. ISSN 0194-911X, 1524-4563. Cited 2 times in 17 and 30.

BAUMBACH, G. L.; SIEMS, J. E.; HEISTAD, D. D. Effects of local reduction in pressure on distensibility and composition of cerebral arterioles. *Circulation Research*, v. 68, n. 2, p. 338–351, fev. 1991. ISSN 0009-7330, 1524-4571. Cited in page 86.

BERNIER, M.; CUNNANE, S. C.; WHITTINGSTALL, K. The morphology of the human cerebrovascular system. *Human Brain Mapping*, v. 39, n. 12, p. 4962–4975, dez. 2018. ISSN 1065-9471, 1097-0193. Cited 3 times in 18, 31, and 36.

BLANCO, P. J.; MÜLLER, L. O.; SPENCE, J. D. Blood pressure gradients in cerebral arteries: A clue to pathogenesis of cerebral small vessel disease. *Stroke and Vascular Neurology*, v. 2, n. 3, p. 108–117, set. 2017. ISSN 2059-8688, 2059-8696. Cited 4 times in 17, 18, 29, and 86.

BLANCO, P. J. et al. On the anatomical definition of arterial networks in blood flow simulations: Comparison of detailed and simplified models. *Biomechanics and Modeling in Mechanobiology*, v. 19, n. 5, p. 1663–1678, out. 2020. ISSN 1617-7959, 1617-7940. Cited 2 times in 22 and 34.

BLANCO, P. J.; QUEIROZ, R. A. B. D.; FEIJÓO, R. A. A computational approach to generate concurrent arterial networks in vascular territories. *International Journal for Numerical Methods in Biomedical Engineering*, v. 29, n. 5, p. 601–614, maio 2013. ISSN 2040-7939, 2040-7947. Cited in page 37.

BLANCO, P. J. et al. An Anatomically Detailed Arterial Network Model for One-Dimensional Computational Hemodynamics. *IEEE Transactions on Biomedical Engineering*, v. 62, n. 2, p. 736–753, fev. 2015. ISSN 0018-9294, 1558-2531. Cited 10 times in 22, 33, 34, 53, 57, 59, 60, 63, 74, and 88.

CASSOT, F. et al. A Novel Three-Dimensional Computer-Assisted Method for a Quantitative Study of Microvascular Networks of the Human Cerebral Cortex. *Microcirculation*, v. 13, n. 1, p. 1–18, jan. 2006. ISSN 1073-9688, 1549-8719. Cited 7 times in 18, 28, 31, 68, 69, 70, and 95.

CASSOT, F. et al. Branching patterns for arterioles and venules of the human cerebral cortex. *Brain Research*, v. 1313, p. 62–78, fev. 2010. ISSN 00068993. Cited 5 times in 38, 75, 88, 92, and 94.

CURY, L. F. M. et al. Parallel generation of extensive vascular networks with application to an archetypal human kidney model. *Royal Society Open Science*, v. 8, n. 12, p. 210973, dez. 2021. ISSN 2054-5703. Cited 10 times in 21, 45, 48, 49, 54, 61, 74, 75, 76, and 79.

DAYEH, M. A.; LIVADIOTIS, G.; ELAYDI, S. A discrete mathematical model for the aggregation of β-Amyloid. *PLOS ONE*, v. 13, n. 5, p. e0196402, maio 2018. ISSN 1932-6203. Cited in page 30.

DIEM, A. K. et al. A Simulation Model of Periarterial Clearance of Amyloid-β from the Brain. *Frontiers in Aging Neuroscience*, v. 8, fev. 2016. ISSN 1663-4365. Cited 2 times in 17 and 30.

DUVERNOY, H.; DELON, S.; VANNSON, J. Cortical blood vessels of the human brain. *Brain Research Bulletin*, v. 7, n. 5, p. 519–579, nov. 1981. ISSN 03619230. Cited 7 times in 18, 25, 27, 28, 32, 84, and 91.

FÅHRÆUS, R.; LINDQVIST, T. The viscosity of the Blood in Narrow Capillary Tubes. *American Journal of Physiology-Legacy Content*, v. 96, n. 3, p. 562–568, mar. 1931. ISSN 0002-9513. Cited 4 times in 26, 39, 74, and 88.

FEIGIN, V. L. et al. Global, regional, and national burden of stroke and its risk factors, 1990–2019: A systematic analysis for the Global Burden of Disease Study 2019. *The Lancet Neurology*, v. 20, n. 10, p. 795–820, out. 2021. ISSN 14744422. Cited 2 times in 16 and 27.

FUJISHIMA, M. et al. Cerebral Blood Flow and Brain Function in Hypertension. *Hypertension Research*, v. 18, n. 2, p. 111–117, 1995. ISSN 0916-9636, 1348-4214. Cited 2 times in 17 and 30.

GENTILE, M. T. et al. β-Amyloid deposition in brain is enhanced in mouse models of arterial hypertension. *Neurobiology of Aging*, v. 30, n. 2, p. 222–228, fev. 2009. ISSN 01974580. Cited in page 30.

GOULD, I. G. et al. The capillary bed offers the largest hemodynamic resistance to the cortical blood supply. *Journal of Cerebral Blood Flow & Metabolism*, v. 37, n. 1, p. 52–68, jan. 2017. ISSN 0271-678X, 1559-7016. Cited 3 times in 20, 31, and 99.

HARTUNG, G. et al. Mathematical synthesis of the cortical circulation for the whole mouse brain—part II: Microcirculatory closure. *Microcirculation*, v. 28, n. 5, jul. 2021. ISSN 1073-9688, 1549-8719. Cited 7 times in 19, 21, 25, 65, 70, 92, and 93.

HARTUNG, G. et al. Simulations of blood as a suspension predicts a depth dependent hematocrit in the circulation throughout the cerebral cortex. *PLOS Computational Biology*, v. 14, n. 11, p. e1006549, nov. 2018. ISSN 1553-7358. Cited 2 times in 17 and 99.

HEAGERTY, A. M. et al. Small artery structure in hypertension. Dual processes of remodeling and growth. *Hypertension*, v. 21, n. 4, p. 391–397, abr. 1993. ISSN 0194-911X, 1524-4563. Cited in page 30.

HEINZER, S. et al. Hierarchical microimaging for multiscale analysis of large vascular networks. *NeuroImage*, v. 32, n. 2, p. 626–636, ago. 2006. ISSN 10538119. Cited 4 times in 18, 31, 32, and 36.

HIRSCH, S. et al. Topology and Hemodynamics of the Cortical Cerebrovascular System. *Journal of Cerebral Blood Flow & Metabolism*, v. 32, n. 6, p. 952–967, jun. 2012. ISSN 0271-678X, 1559-7016. Cited 3 times in 28, 65, and 69.

IADECOLA, C. Neurovascular regulation in the normal brain and in Alzheimer's disease. *Nature Reviews Neuroscience*, v. 5, n. 5, p. 347–360, maio 2004. ISSN 1471-003X, 1471-0048. Cited 2 times in 17 and 30.

IADECOLA, C. The Neurovascular Unit Coming of Age: A Journey through Neurovascular Coupling in Health and Disease. *Neuron*, v. 96, n. 1, p. 17–42, set. 2017. ISSN 08966273. Cited in page 25.

IADECOLA, C.; ANRATHER, J. The immunology of stroke: From mechanisms to translation. *Nature Medicine*, v. 17, n. 7, p. 796–808, jul. 2011. ISSN 1078-8956, 1546-170X. Cited 2 times in 27 and 29.

IADECOLA, C. et al. The Neurovasculome: Key Roles in Brain Health and Cognitive Impairment: A Scientific Statement From the American Heart Association/American Stroke Association. *Stroke*, v. 54, n. 6, jun. 2023. ISSN 0039-2499, 1524-4628. Cited 2 times in 25 and 27.

JAMES, M. A. et al. Effects of Aging and Hypertension on the Microcirculation. *Hypertension*, v. 47, n. 5, p. 968–974, maio 2006. ISSN 0194-911X, 1524-4563. Cited in page 17.

JÓZSA, T. I. et al. A porous circulation model of the human brain for *in silico* clinical trials in ischaemic stroke. *Interface Focus*, v. 11, n. 1, p. 20190127, fev. 2021. ISSN 2042-8898, 2042-8901. Cited 3 times in 18, 20, and 31.

KARCH, R. et al. A three-dimensional model for arterial tree representation, generated by constrained constructive optimization. *Computers in Biology and Medicine*, v. 29, n. 1, p. 19–38, jan. 1999. ISSN 00104825. Cited 7 times in 21, 37, 38, 41, 42, 43, and 44.

KARCH, R. et al. Three-Dimensional Optimization of Arterial Tree Models. *Transactions on Biomedicine and Health*, v. 4, 1997. ISSN 1743-3525. Cited 4 times in 36, 37, 40, and 41.

KELLY, D. M.; ROTHWELL, P. M. Blood pressure and the brain: The neurology of hypertension. *Practical Neurology*, v. 20, n. 2, p. 100–108, abr. 2020. ISSN 1474-7758, 1474-7766. Cited in page 86.

KÖPPL, T.; VIDOTTO, E.; WOHLMUTH, B. A 3D-1D coupled blood flow and oxygen transport model to generate microvascular networks. *International Journal for Numerical Methods in Biomedical Engineering*, v. 36, n. 10, out. 2020. ISSN 2040-7939, 2040-7947. Cited in page 20.

LAUWERS, F. et al. Morphometry of the human cerebral cortex microcirculation: General characteristics and space-related profiles. *NeuroImage*, v. 39, n. 3, p. 936–948, fev. 2008. ISSN 10538119. Cited 4 times in 26, 65, 69, and 94.

LEE, R. M. Morphology of cerebral arteries. *Pharmacology & Therapeutics*, v. 66, n. 1, p. 149–173, jan. 1995. ISSN 01637258. Cited in page 32.

LIANG, K. K. *Efficient Conversion from Rotating Matrix to Rotation Axis and Angle by Extending Rodrigues' Formula*. [S.l.]: arXiv, 2018. Cited 2 times in 61 and 72.

LIM, E. W. et al. Amyloid-β and Parkinson's disease. *Journal of Neurology*, v. 266, n. 11, p. 2605–2619, nov. 2019. ISSN 0340-5354, 1432-1459. Cited in page 30.

LINNINGER, A. et al. Mathematical synthesis of the cortical circulation for the whole mouse brain-part I. theory and image integration. *Computers in Biology and Medicine*, v. 110, p. 265–275, jul. 2019. ISSN 00104825. Cited 5 times in 19, 37, 40, 41, and 42.

LINNINGER, A. A. et al. Cerebral Microcirculation and Oxygen Tension in the Human Secondary Cortex. *Annals of Biomedical Engineering*, v. 41, n. 11, p. 2264–2284, nov. 2013. ISSN 0090-6964, 1573-9686. Cited 7 times in 41, 64, 68, 70, 81, 86, and 98.

LIPOWSKY, H. H. Microvascular Rheology and Hemodynamics. *Microcirculation*, v. 12, n. 1, p. 5–15, jan. 2005. ISSN 1073-9688, 1549-8719. Cited in page 86.

LORTHOIS, S.; CASSOT, F.; LAUWERS, F. Simulation study of brain blood flow regulation by intra-cortical arterioles in an anatomically accurate large human vascular network: Part I: Methodology and baseline flow. *NeuroImage*, v. 54, n. 2, p. 1031–1042, jan. 2011. ISSN 10538119. Cited in page 17.

MALATINO, L. S. et al. Cerebral blood flow velocity after hyperventilation-induced vasoconstriction in hypertensive patients. *Stroke*, v. 23, n. 12, p. 1728–1732, dez. 1992. ISSN 0039-2499, 1524-4628. Cited 2 times in 18 and 31.

MATANO, F. et al. Long-term patency of superficial temporal artery to middle cerebral artery bypass for cerebral atherosclerotic disease: Factors determining the bypass patent. *Neurosurgical Review*, v. 39, n. 4, p. 655–661, out. 2016. ISSN 0344-5607, 1437-2320. Cited in page 86.

MÜLLER, L. O. et al. A high-order local time stepping finite volume solver for one-dimensional blood flow simulations: Application to the ADAN model. *International Journal for Numerical Methods in Biomedical Engineering*, v. 32, n. 10, p. e02761, out. 2016. ISSN 2040-7939, 2040-7947. Cited in page 22.

MÜLLER, L. O. et al. An anatomically detailed arterial-venous network model. Cerebral and coronary circulation. *Frontiers in Physiology*, v. 14, p. 1162391, jun. 2023. ISSN 1664-042X. Cited 2 times in 34 and 35.

MURRAY, C. D. The Physiological Principle of Minimum Work: I. The Vascular System and the Cost of Blood Volume. *Proceedings of the National Academy of Sciences*, v. 12, n. 3, p. 207–214, mar. 1926. ISSN 0027-8424, 1091-6490. Cited 3 times in 38, 67, and 75.

NADER, C. A. et al. SimulAD: A dynamical model for personalized simulation and disease staging in Alzheimer's disease. *Neurobiology of Aging*, v. 113, p. 73–83, maio 2022. ISSN 01974580. Cited in page 17.

NARASIMHAN, M.; SCHWARTZ, R.; HALLIDAY, G. Parkinsonism and cerebrovascular disease. *Journal of the Neurological Sciences*, v. 433, p. 120011, fev. 2022. ISSN 0022510X. Cited in page 30.

NISHIMURA, N. et al. Penetrating arterioles are a bottleneck in the perfusion of neocortex. *Proceedings of the National Academy of Sciences*, v. 104, n. 1, p. 365–370, jan. 2007. ISSN 0027-8424, 1091-6490. Cited in page 69.

NONAKA, H. et al. The Microvasculature of the Cerebral White Matter: Arteries of the Subcortical White Matter. *Journal of Neuropathology & Experimental Neurology*, v. 62, n. 2, p. 154–161, fev. 2003. ISSN 0022-3069, 1554-6578. Cited in page 18.

NONAKA, H. et al. Microvasculature of the human cerebral white matter: Arteries of the deep white matter. *Neuropathology*, v. 23, n. 2, p. 111–118, jun. 2003. ISSN 0919-6544, 1440-1789. Cited 2 times in 18 and 32.

OTANI, T. et al. Computational modeling of multiscale collateral blood supply in a whole-brain-scale arterial network. *PLOS Computational Biology*, v. 19, n. 9, p. e1011452, set. 2023. ISSN 1553-7358. Cited in page 20.

PADMOS, R. M. et al. Coupling one-dimensional arterial blood flow to three-dimensional tissue perfusion models for *in silico* trials of acute ischaemic stroke. *Interface Focus*, v. 11, n. 1, p. 20190125, fev. 2021. ISSN 2042-8898, 2042-8901. Cited in page 20.

PRIES, A. R.; NEUHAUS, D.; GAEHTGENS, P. Blood viscosity in tube flow: Dependence on diameter and hematocrit. *American Journal of Physiology-Heart and Circulatory Physiology*, v. 263, n. 6, p. H1770–H1778, dez. 1992. ISSN 0363-6135, 1522-1539. Cited in page 40.

PRIES, A. R. et al. Resistance to blood flow in microvessels in vivo. *Circulation Research*, v. 75, n. 5, p. 904–915, nov. 1994. ISSN 0009-7330, 1524-4571. Cited in page 39.

RAY, L. A.; HEYS, J. J. Fluid Flow and Mass Transport in Brain Tissue. *Fluids*, v. 4, n. 4, p. 196, nov. 2019. ISSN 2311-5521. Cited 2 times in 26 and 30.

REICHOLD, J. et al. Vascular Graph Model to Simulate the Cerebral Blood Flow in Realistic Vascular Networks. *Journal of Cerebral Blood Flow & Metabolism*, v. 29, n. 8, p. 1429–1443, ago. 2009. ISSN 0271-678X, 1559-7016. Cited 2 times in 17 and 20.

Reina-De La Torre, F.; Rodriguez-Baeza, A.; Sahuquillo-Barris, J. Morphological characteristics and distribution pattern of the arterial vessels in human cerebral cortex: A scanning electron microscope study. *The Anatomical Record*, v. 251, n. 1, p. 87–96, maio 1998. ISSN 0003-276X, 1097-0185. Cited 7 times in 18, 26, 29, 32, 65, 69, and 95.

REYMOND, P. et al. Validation of a one-dimensional model of the systemic arterial tree. *American Journal of Physiology-Heart and Circulatory Physiology*, v. 297, n. 1, p. H208–H222, jul. 2009. ISSN 0363-6135, 1522-1539. Cited 2 times in 18 and 33.

SCHAEFFER, S.; IADECOLA, C. Revisiting the neurovascular unit. *Nature Neuroscience*, v. 24, n. 9, p. 1198–1209, set. 2021. ISSN 1097-6256, 1546-1726. Cited 3 times in 24, 25, and 26.

SCHMID, F. et al. Vascular density and distribution in neocortex. *NeuroImage*, v. 197, p. 792–805, ago. 2019. ISSN 10538119. Cited 7 times in 21, 23, 26, 31, 65, 66, and 76.

SCHREINER, W. Computer generation of complex arterial tree models. *Journal of Biomedical Engineering*, v. 15, n. 2, p. 148–150, mar. 1993. ISSN 01415425. Cited in page 36.

SCHREINER, W.; BUXBAUM, P. Computer-optimization of vascular trees. *IEEE Transactions on Biomedical Engineering*, v. 40, n. 5, p. 482–491, maio 1993. ISSN 0018-9294, 1558-2531. Cited 2 times in 36 and 38.

SCHREINER, W. et al. The influence of optimization target selection on the structure of arterial tree models generated by constrained constructive optimization. *The Journal of general physiology*, v. 106, n. 4, p. 583–599, out. 1995. ISSN 0022-1295, 1540-7748. Cited in page 38.

SCHREINER, W. et al. Structural Quantification and Bifurcation Symmetry in Arterial Tree Models Generated by Constrained Constructive Optimization. *Journal of Theoretical Biology*, v. 180, n. 2, p. 161–174, maio 1996. ISSN 00225193. Cited in page 37.

SCHÜNKE, M.; SCHULTE, E.; SCHUMACHER, U. *Head and Neuroanatomy*. Stuttgart: Thieme, 2010. ISBN 978-1-60406-296-0. Cited 5 times in 23, 24, 25, 27, and 53.

SHIMA, T. et al. Cortical Arterial Pressure and Anastomotic Blood Flow Measurements during STA-MCA Anastomosi. *Neurologia medico-chirurgica*, v. 28, n. 4, p. 340–345, 1988. ISSN 0470-8105, 1349-8029. Cited in page 86.

STERGIOPULOS, N.; YOUNG, D.; ROGGE, T. Computer simulation of arterial flow with applications to arterial and aortic stenoses. *Journal of Biomechanics*, v. 25, n. 12, p. 1477–1488, dez. 1992. ISSN 00219290. Cited 2 times in 29 and 33.

TALOU, G. D. M. et al. Adaptive constrained constructive optimisation for complex vascularisation processes. *Scientific Reports*, v. 11, n. 1, p. 6180, mar. 2021. ISSN 2045-2322. Cited 10 times in 37, 38, 44, 45, 46, 47, 49, 61, 62, and 75.

TATU, L. et al. Arterial territories of the human brain: Cerebral hemispheres. *Neurology*, v. 50, n. 6, p. 1699–1708, jun. 1998. ISSN 0028-3878, 1526-632X. Cited in page 31.

WEBER, B. et al. The Microvascular System of the Striate and Extrastriate Visual Cortex of the Macaque. *Cerebral Cortex*, v. 18, n. 10, p. 2318–2330, out. 2008. ISSN 1460-2199, 1047-3211. Cited in page 69.

ZAMIR, M. On Fractal Properties of Arterial Trees. *Journal of Theoretical Biology*, v. 197, n. 4, p. 517–526, abr. 1999. ISSN 00225193. Cited in page 36.

ZAMIR, M. Arterial Branching within the Confines of Fractal L-System Formalism. *The Journal of General Physiology*, v. 118, n. 3, p. 267–276, set. 2001. ISSN 0022-1295, 1540-7748. Cited in page 36.

Appendix

APPENDIX A – Technical definitions for replicability

A.1 Versions of packages and execution

This appendix cites the software versions for replicating this study. The software versions used in this work were:

a) Blender 3.4 `https://www.blender.org/`

b) Paraview 5.11 `https://www.paraview.org/`

c) VTK version 8.1.2 `https://vtk.org/`

d) VItA, for reference, originally from
`https://github.com/GonzaloMaso/VItA`

e) VItA, PDCCO branch obtained from the git tag
`https://github.com/lfmc/VItA/tree/Cury2021_et_al_PDCCO`

f) VItA with the algorithms to penetrate the gray matter and to append sub-trees
`https://github.com/egzilves/VItA/tree/v0.1-202407`

The generation is conducted in a Podman or Singularity containers running Ubuntu 22.04 with VTK and VItA compiled and installed in it. The execution occurs in two scenarios:

a) a desktop PC with Ryzen 5700G CPU with 16GB of Ram, running Debian Linux 12, using a Podman container with Ubuntu 22.04, for the first two stages of the pial network, and the stages involving the generation of the gray matter network;

b) the HPC environment of the LNCC/MCTI SDumont supercomputer, using a Singularity container with Ubuntu 22.04, for the generation of the parallelized pial network.

The containers are first built in the desktop PC and later deployed to the supercomputer. More information about the SDumont supercomputer can be found in:

a) LNCC/MCTI SDumont supercomputer home page
`https://sdumont.lncc.br/index.php`